

**Earth Radiation Budget Variability and Its Relationship to
Changes in the General Circulation**

by
David L. Randel

Department of Atmospheric Science
Colorado State University
Fort Collins, Colorado

**Colorado
State
University**

**Department of
Atmospheric Science**

Paper No. 478

**EARTH RADIATION BUDGET VARIABILITY AND ITS RELATIONSHIP
TO CHANGES IN THE GENERAL CIRCULATION**

by

David L. Randel

Department of Atmospheric Science
Colorado State University
Fort Collins, CO 80523

This research was supported by the National Aeronautics and
Space Administration (NASA) Grant No. NAG 1-661

Principal Investigator: Thomas H. Vonder Haar

Atmospheric Science Paper No. 478

February, 1991

ABSTRACT

The geographical variability of the radiation balance forces the different atmospheric circulations. To fully comprehend the variability in these atmospheric flow patterns we must address the fundamental problems of how changes in the earth radiation budget (ERB) affects these circulations, and also the role of clouds in modification of the ERB.

The *Nimbus-7* satellite ERB climatology from 1978–1987 is presented as well as the interannual variability. The areas with highest variations are reported for each of the ERB parameters and show the pronounced effect of the 1982–1983 El Niño. Concurrent with the ERB observations is an independent five year cloud climatology allowing for comparisons of ERB with estimates of total and multi-level cloud amounts. The area of greatest variability in the net balance occurs off the west African coast where there are primarily middle and low level clouds, not in the Pacific where the changes are mainly in convective cloudiness. Convective clouds have less net balance variation due to the reciprocity in their shortwave and longwave fluxes.

The circulation data includes eight years of ECMWF global winds and temperatures from which the eddy and zonal components of the available potential and kinetic energies are computed. The circulation differences between the continental Northern Hemisphere and oceanic Southern Hemisphere are interpreted in terms of the magnitudes of these energetic terms. For the direct study of ERB and energetic comparisons, a simultaneous time series of mid-latitude ERB gradients and hemispheric averaged energetics are examined. By doing a time correlation study we found the annual cycles of the radiation gradients to lead the energetics by 2-3 weeks.

The spatial relationship of the variability in the ERB related to tropical circulations is investigated through spatial correlations. Reference areas are defined from the areas of highest variability and correlated with all other global areas. Tropical ERB anomalies are also correlated with mid-latitude 500 mb geopotential anomalies derived from the ECMWF global weather data. While correlations are smaller than the ERB–ERB comparisons, the mid-latitude geopotential heights in the Gulf of Alaska are shown to have a strong connection with equatorial OLR anomalies.

ACKNOWLEDGEMENTS

This research was accomplished with the guidance and support of Professor Thomas H. Vonder Haar, my committee head and advisor. Without his continued encouragement and patience this research would have remained fragmented and without direction. His support in allowing me to attend numerous scientific meetings and conferences helped to broaden my knowledge of the current and future problems in our field. Professors Wayne H. Schubert, Steven K. Cox, and M. Moinuddin Siddiqui were valuable members of my advisory committee and I thank them for their critical suggestions. Dr. Thomas A. Brubaker graciously volunteered to replace Dr. Siddiqui during the final stages of this work. Thanks also to G. Garrett Campbell for assistance with the *Nimbus-7* ERB calibration and with the CMATRIX cloud data set. Kelly Dean provided the software and data processing of the CMATRIX data. Many of the preliminary discussions for this work were made with the assistance of Dr. Laura D. Smith. Without the 20 year supreme effort of the members of the *Nimbus-7* ERB Science Team, the ERB experiment, data processing and final set of products would never have occurred. This effort was far beyond that which could be expected of each of these fine scientists. Mrs. Judy Sorbie-Dunn expertly drafted many of the figures.

Finally thanks go to my many family, including my brothers, sister, parents Willie and Verna, and especially my wife Anny who was there for every minute. Also to my friends whose constant support, interested questions, and encouragement was simply beyond belief.

This research was made possible primarily by the financial assistance of NASA contract NAG-1-661.

TABLE OF CONTENTS

1 INTRODUCTION	1
1.1 Scientific Contributions of ERB Studies	3
1.2 Dissertation Objectives and Plan	5
2 DESCRIPTION OF THE NIMBUS-7 INSTRUMENTS, DATA, AND DATA PROCESSING	7
2.1 Nimbus-7 Earth Radiation Budget Instrumentation	7
2.2 Earth Radiation Budget Data Selection	9
2.3 Defining the Minimum Temporal and Spatial Scale	11
2.4 ERB Data Calibration	15
2.5 ERB Data Processing	18
2.6 Nimbus-7 Derived Cloud Climatology	20
3 EXAMINATION OF THE EIGHT YEAR NIMBUS-7 EARTH RADIATION BUDGET DATA SET	22
3.1 Eight Year Nimbus-7 Averages	22
3.1.1 Global average values	22
3.1.2 Outgoing Longwave Radiation - OLR	24
3.1.3 Albedo	28
3.1.4 Net radiation balance	31
3.1.5 Southern Hemisphere 'three wave pattern'	35
3.1.6 Required total energy transport	37
3.2 Monthly Averages and Annual Cycles	41
3.2.1 Outgoing longwave radiation and net balance	41
3.2.2 Albedo	43
4 VARIABILITY IN THE EARTH RADIATION BUDGET	47
4.1 Interannual Variability	47
4.1.1 ERB Variability of One Year Averages	47
4.1.2 ERB Variability of Monthly Averages	49
4.1.3 ERB Variability with Annual Cycle	55
4.2 Examination of the Interannual NET Variability	57
4.2.1 NET Time Series	60
4.2.2 Cloud Variability in Three Areas of Highest NET Variability	64
4.2.3 Discussion and Conclusions on Highest NET Variability Areas	64

5	ATMOSPHERIC ENERGETICS AND NIMBUS-7 ERB COMPARISONS	69
5.1	Atmospheric Circulation Data	69
5.2	Energetics	70
5.2.1	Kinetic Energy	70
5.2.2	Available Potential Energy	71
5.3	ERB and Energetics Comparisons	78
5.3.1	Annual cycle	78
5.3.2	Weekly Anomalies	79
5.4	Winter Only Correlations	85
5.5	Discussion and Summary	87
6	OBSERVED NIMBUS-7 ERB TELECONNECTIONS	89
6.1	ERB to ERB Comparisons	90
6.1.1	Background	90
6.1.2	OLR Teleconnections	92
6.1.3	NET Teleconnections	94
6.2	ERB to Geopotential Height Comparison	97
7	SUMMARY AND CONCLUSIONS	105
	REFERENCES	109

LIST OF FIGURES

2.1	Wide field-of-view instrument.	8
2.2	Zonal averaged RMS WFOV vs NFOV.	12
2.3	Zonal averaged RMS error for the six day composite WFOV OLR with and without deconvolution.	14
2.4	Global average RMS for a 6 day sample period with and without deconvolution.	15
2.5	Zonal bias of NFOV and WFOV data.	16
2.6	Final RMS error.	17
3.1	Ascending node outgoing longwave radiation.	25
3.2	Descending node outgoing longwave radiation.	25
3.3	Daily averaged Outgoing longwave radiation.	26
3.4	Zonal averaged OLR.	27
3.5	OLR diurnal variability.	29
3.6	Zonal averaged OLR diurnal variability.	30
3.7	Daily averaged Albedo.	31
3.8	Zonal averaged albedo (%) from 11/78 – 10/86.	32
3.9	Net balance.	33
3.10	Zonal averaged of the net balance (NET) (Wm^{-2}) from 11/78 – 10/86.	34
3.11	Net radiation gradient.	36
3.12	Total required atmospheric transport.	38
3.13	Net, OLR and Albedo annual cycles.	44
3.14	Annual cycle of sub-hemispheric averaged albedo (%).	46
4.1	OLR standard deviation of annual averages.	50
4.2	Albedo standard deviation of annual averages.	51
4.3	NET standard deviation of the annual averages.	52
4.4	OLR standard deviation with monthly variability.	54
4.5	Albedo standard deviation with monthly variability.	55
4.6	NET standard deviation with monthly variability.	56
4.7	NET standard deviation with annual cycle.	57
4.8	Albedo standard deviation with annual cycle.	58
4.9	OLR standard deviation with annual cycle.	58
4.10	NET weekly anomalies for three areas.	61
4.11	OLR weekly anomalies for three areas.	63
4.12	Total and high cloud anomalies for three areas.	65
4.13	Middle and low cloud anomalies for three areas.	66
5.1	Zonal and eddy kinetic energy time series.	72
5.2	Zonal and eddy available potential energy.	75
5.3	Atmospheric energy diagram.	76

5.4	NH cycles of zonal APE, NET and OLR gradients.	79
5.5	SH cycles of zonal APE, NET and OLR gradients.	80
5.6	NET gradient anomaly time series.	82
5.7	OLR gradient anomaly time series.	83
6.1	OLR Correlation coefficient for South America.	92
6.2	OLR Correlation coefficient for the central Pacific.	93
6.3	OLR Correlation coefficient for the western Pacific.	94
6.4	NET Correlation coefficient for the Gulf of Guinea.	95
6.5	NET Correlation coefficient for the western Pacific.	96
6.6	NET Correlation coefficient for the eastern Pacific.	97
6.7	NET - 500mb height correlation coefficient for the Gulf of Guinea.	99
6.8	NET - 500mb height correlation coefficient for the western Pacific.	100
6.9	OLR - 500mb height correlation coefficient for Brazil.	101
6.10	OLR - 500mb height correlation coefficient for the western Pacific.	101
6.11	OLR - 500mb height correlation coefficient for the central Pacific.	103
6.12	Hypothesized pattern of mid-latitude GH heights during a tropical SST warming event.	104

LIST OF TABLES

2.1	Spectral characteristics of the <i>Nimbus-7</i> Earth Radiation Budget experiment channels.	9
3.1	ERB global averages.	23
3.2	ERB OLR, Albedo and NET zonal averages.	39
3.3	ERB diurnal difference and total transport zonal averages.	40
3.4	ERB global monthly averages.	41
3.5	ERB NH monthly averages.	42
3.6	ERB SH monthly averages.	42
4.1	ERB global average standard deviation - annual average.	48
4.2	ERB standard deviation - monthly averages.	53
5.1	Energetic correlation coefficients.	77
5.2	Energetic correlation coefficients of weekly averages.	78
5.3	Correlation of APE and NET, OLR gradients.	80
5.4	Correlation of weekly ERB vs. energetics.	84
5.5	Correlation of weekly ERB and Energetic eddy terms.	85
5.6	Correlation coefficients for winter only.	86

Chapter 1

INTRODUCTION

The geographical distribution of the difference in the absorbed and emitted radiation drives our earth's circulation. This has been known for hundreds of years since Hadley, Ferrel and others first described the workings of the major features of the atmosphere. These include circulation features such as the strong tropical low level convergence with heavy rainfall, the subtropics with their consistent trade winds, the westerlies of the mid-latitudes, and the polar easterlies. Each of these features is related to the uneven distribution of incoming solar radiation that impinges on the earth's atmosphere modified by the earth's rotation. With the launch of the USA's Explorer VII in 1959, scientists began to realize the potential for observing the earth-atmosphere system and its radiation balance with satellites measurements. These unique observing platforms enabled true global coverage for the first time – the dream of global climatologists only a few years before. Enter the era of satellite observations. Even though there now has been over 30 years of earth observing satellite measurements, the interest in the distribution and variability of the net radiation balance has never waned, possibly due to the basic, primary nature of the measurement. If we could measure with perfect accuracy the amount and geographical distribution of the components of the radiation balance, a quantum leap in our understanding of the functioning of the atmosphere would result. However no perfect instrument can ever be designed, and there will always be error in the accuracy of the sensors and in the limitations of the data sampling and retrieval. For this reason we must fully understand the shortcomings of each new instrument system which puts limits on the validity and confidence of our scientific conclusions. This understanding leads to improved design of the next generation of radiation budget instruments.

In the long term average, the net radiation balance (NET) is positive equatorward of approximately 40° . Due to the large amount of incoming radiation, this area absorbs more radiation than it emits. Poleward of 40° the reverse is true and emission is greater than absorption. The tilt of the earth's axis creates a seasonal cycle to the NET so that during the summer months the latitude of radiative balance is much further poleward. This seasonal cycle causes the greatest temporal variability in the radiation balance. The global circulation features that are driven by the radiation distribution cause areas of convergence and divergence and associated vertical motion fields. These force the formation and dissipation of clouds. Over 50 % of the earth's surface is covered by clouds and these have a large impact on the absorbed and emitted radiances. A simplified explanation of the effect of clouds is that they cause decreased absorption because they reflect shortwave solar radiation. However, simultaneously the clouds emit less terrestrial longwave radiation than clear sky due to their high altitude and cooler emitting temperatures. Since these effects are in opposition the resulting NET effect of the clouds is anything but simple. Cloud amount and cloud type play major roles in determining if shortwave or longwave influences will dominate. At the smaller scale, the earth's surface properties affect the radiation components by the shortwave reflectivity and the longwave emitting temperature of the surface. The land-ocean contrast in surface properties produce small scale circulations that rival the large global scale circulations in intensity. The differences in the land and ocean percentages between the northern and southern hemispheres cause each half of the earth to experience much different weather and circulation patterns.

These interactions between the radiation variability and the atmospheric circulations that result is the subject of this dissertation. This study required long term continuous data sets of both earth radiation budget (ERB) data and atmospheric circulation data. Both of these requirements have only recently been met. Over eight years of global circulation data, accurate in the Northern as well as Southern Hemisphere are available from the European Centre for Medium Range Weather Forecasts (ECMWF). At present over nine years of *Nimbus-7* ERB observations with global coverage, concurrent with the ECMWF circulation data are available. Therefore this study follows a two pronged approach culminating in our goal of direct comparison of the ERB variability with variability in the

atmospheric circulation. First however, we examine and present the ERB climatology with emphasis on the areas on highest variability. An closer examination of the net balance variability related to cloud variability helps us understand the type of clouds and cloud changes that affect the balance the most. Second, the atmospheric circulation data is used to calculate atmospheric available potential and kinetic energetics. These energetics are used as a descriptor of the current state and variability of the atmosphere. The annual cycle of the energetics explains much of the functionality of the large scale general circulation and points out the circulation differences between the hemispheres. Lastly, spatial connections are examined by comparing the tropical ERB areas of highest variability with mid-latitudes geopotential heights.

In the following sections a short historical background of the ERB measurement systems will be given and then finally a more detailed outline of the dissertation is presented.

1.1 Scientific Contributions of ERB Studies

The first attempt to measure the components of the ERB was from the Suomi black/white painted ping-pong ball radiometers on Explorer VII. Though crude, this instrument and later flat plate radiometers showed the global distribution of longwave and shortwave terrestrial emission and reflectivity at low resolution. Vonder Haar and Suomi (1971) presented 39 months of ERB measurements from the earliest satellite over the years 1962–1966. These included the Tiros and ESSA satellite series as well as *Nimbus-2*. Included were complete discussions of the annual cycle as well as seasonal values of the total atmospheric transport. Vonder Haar's (1968) results from these Wide Field-Of-View (WFOV) instruments showed the earth to have a lower albedo and higher radiative temperature than from contemporary theoretical calculations. *Nimbus-2* and *Nimbus-3* flew instruments quite different than the flat plate radiometers. These were the first ERB scanning radiometers with spatial resolutions of 200 X 200 km. Raschke and Bandeen (1970) provided from *Nimbus-3* global maps of longwave flux, reflected shortwave and net radiation from 1966 data. The complexity of data processing into total earth flux took a leap in magnitude due to the need to apply complicated bi-directional reflectance models

to the calculated top of the atmosphere reflectivity. Also limb darkening models were necessary to estimate the total emitted irradiance. Seasonal cycles of ERB were available from 10 periods between April 1969 and February 1970 producing the first time-latitude cross section of the ERB (Raschke et al. 1973). Zonal averaged radiation budget data for 29 months from 1964–1971 were presented by Ellis and Vonder Haar (1976) and showed the monthly variability in the ERB. The *Nimbus-6* satellite was launched in 1975 with an instrument package nearly identical to the *Nimbus-7* ERB experiment. Jacobowitz et al. (1979) reported global averaged values of 31 % for the albedo and 234 Wm^{-2} infrared flux, nearly the 'accepted' values of today. Stephens, et al. (1981) reported on a composite of 48 months of ERB data which included *Nimbus-6*. The last *Nimbus* experimental satellite, *Nimbus-7* was launched in October 1978. On board this multi-experiment satellite was the Earth Radiation Budget experiment which included fixed and scanning radiometers as well as the first total solar cavity radiometer. Jacobowitz (1984b) presented the first look at the *Nimbus-7* scanning radiometer data. The albedo was measured as 33 %, roughly 3 % higher than the accepted value. Error analysis showed scanning at high angles caused the bias. The scanner defined the ERB on regional scales and clearly the effects of smaller scales clouds on the daily ERB could be examined (Randel, 1983). Ardanuy et al. (1986) used the first five year climatology to examine changes in the tropical outgoing longwave radiation (OLR) in the Pacific during the 1982-1983 El Niño year. This showed that large scale climate anomalies could accurately be observed from the rough WFOV measurements.

The best earth radiation budget set is available today is from the *Nimbus-7* ERB experiment. Over 9 years of continuous WFOV data has been processed to date and available for use. As of this time, an additional 2-3 years are currently being processed. The scanner data with its much improved resolution lasted the first 18 months of the experiment until a mechanical failure occurred. Smith (1989) recently used the first year of scanner data to define the deviation of clouds with a single month, and compare these with GCM simulated cloud variability. The Earth Radiation Budget Experiment (ERBE) launched in the mid-1980s was a three satellite system designed to increase the accuracy

and temporal resolution of the radiation data. The satellites included the Earth Radiation Budget Satellite launched in 1984 which was the first scientific satellite launched from the USA shuttle system. Identical instruments were launched in the following years on the NOAA-9 and NOAA-10 platforms. ERBE included WFOV and medium FOV sensors as well high resolution scanners. Scanner measurements are now available for a $2.5^{\circ} \times 2.5^{\circ}$ global coverage grid and are a combination of data from the different satellites. Hartmann et al. (1986) and Ramanathan (1987) give excellent descriptions of the future goals and expectations of the ERBE results. Included are an improved understanding of the cloud-radiation-climate feedbacks and improved validation of climate models. Ramanathan et al. (1989) presenting early results from ERBE showed that clouds, in general, tend to cool the planet.

1.2 Dissertation Objectives and Plan

The long successful history of earth radiation budget measurements continues with the *Nimbus-7* ERB observations. These provide the most accurate long term ERB measurements from a consistent set of instruments. The following chapter provides a description of the *Nimbus-7* instruments, the data, and the data processing steps necessary to compile the nine year data set. The results of the dissertation start in the third chapter where the earth radiation budget climatology from the eight year *Nimbus-7* ERB data set is presented. The data are from the hemispheric viewing WFOV sensors with roughly 10° resolution. Global distributions of albedo, outgoing longwave radiation and net radiation are presented as well as total atmospheric transport. Before we can compare the ERB observations to other circulations indices, an understanding of the ERB observational climatology and their limitations is critical.

In Chapter 4 we first examine the interannual variability of the ERB data. The long time series of continuous observations make these studies possible for the first time. The need to understand the relationship of changes in clouds to the ERB variability is primary to this work. Later sections of this chapter will closely examine the cloud changes in the areas of highest interannual NET variability. This provides valuable insight into the effect

of certain cloud types and cloud amount on the variability of NET radiation. The high variability areas need to be defined for use as reference areas in our ERB anomaly to circulation anomaly comparisons.

The fifth chapter presents atmospheric energetic products derived from the ECMWF initialization fields, including the zonal and eddy components of the kinetic and available potential energy fields. Distinct differences between hemispheres can be explained by the circulation patterns unique to each hemisphere. Our intercomparison between ERB and the circulation starts here with hemispheric scale comparisons of the annual cycles, weekly averages, and weekly anomalies. As the variability of the earth's radiation drives the different circulations, this section shows that observations of radiation budget variations are related to the variability of the atmospheric energetics. This relationship is strongest for the annual cycles of both quantities as both are driven by the annual cycle of the incident solar radiation. However, there are also short term variability correlations which have proved significant enough for future study.

Finally Chapter 6 will conclude the ERB and circulation comparisons by presenting first the simultaneous ERB to ERB teleconnection patterns and finally the ERB to mid-latitude 500 mb geopotential height correlations. The ERB to ERB correlations are important to point out the connections in tropical cloudiness, heating, and circulation patterns. The tropical OLR interactions are often separated by more than 25 % of the circumference of the earth. Weaker correlations with smaller spatial separation are present in the tropical to mid-latitude height teleconnections, though in one case an encouraging 10-15% of the mid-latitude height variability is explained. This case has the tropical ERB reference point in the central Pacific and strong correlations patterns are found off the west coast of the USA. This observation agrees well with published hypothetical results of mid-Pacific warming relating to lower mid-latitude heights. The study of significant tropical ERB anomalies and their effects on the mid-latitudes is enhanced by the 1982-1983 El Niño event occurring during the ERB time series.

Chapter 2

DESCRIPTION OF THE NIMBUS-7 INSTRUMENTS, DATA, AND DATA PROCESSING

2.1 Nimbus-7 Earth Radiation Budget Instrumentation

The *Nimbus-7* satellite was launched in October 1978, and approximately one month later the Earth Radiation Budget (ERB) sensors became operational. *Nimbus-7* was a multi-experiment satellite with ten different instrument packages and was the culmination of a successful *Nimbus* line of experimental satellites. A complete description of the *Nimbus-7* ERB instrument package and mission are provided by Jacobowitz et al., (1978) in *The Nimbus-7 Users Guide*. A more detailed description of the sensor details and components is found in Soule (1983). A brief description of the instruments and their spectral channels and design will follow.

The *Nimbus* ERB instrument consists of 22 radiation detectors. Solar observations from narrow spectral bands were produced by channels 1-9. Channel 10C is a total solar irradiance absorber and was the first accurate cavity radiometer in space to measure the solar constant. Values from 10C range from 1370–1375 Wm^{-2} , lower than previously estimated, but slightly higher than the later Solar Maximum Mission experiment values of 1360–1365 Wm^{-2} . For the net radiation balance calculation from *Nimbus* the solar constant was specified as 1372 Wm^{-2} . Channels 11-14 are fixed earth flux wide field-of-view (WFOV) radiometers. Like the solar channels there were no moving parts and the instruments continue to function. Data from these channels are still being archived and processing to the full 11-12 year data set is expected. Channels 11 and 12 are total earth flux hemispheric dome instruments and make redundant measurements, but channel 12 is used only occasionally to check the constancy of channel 11. The only difference in

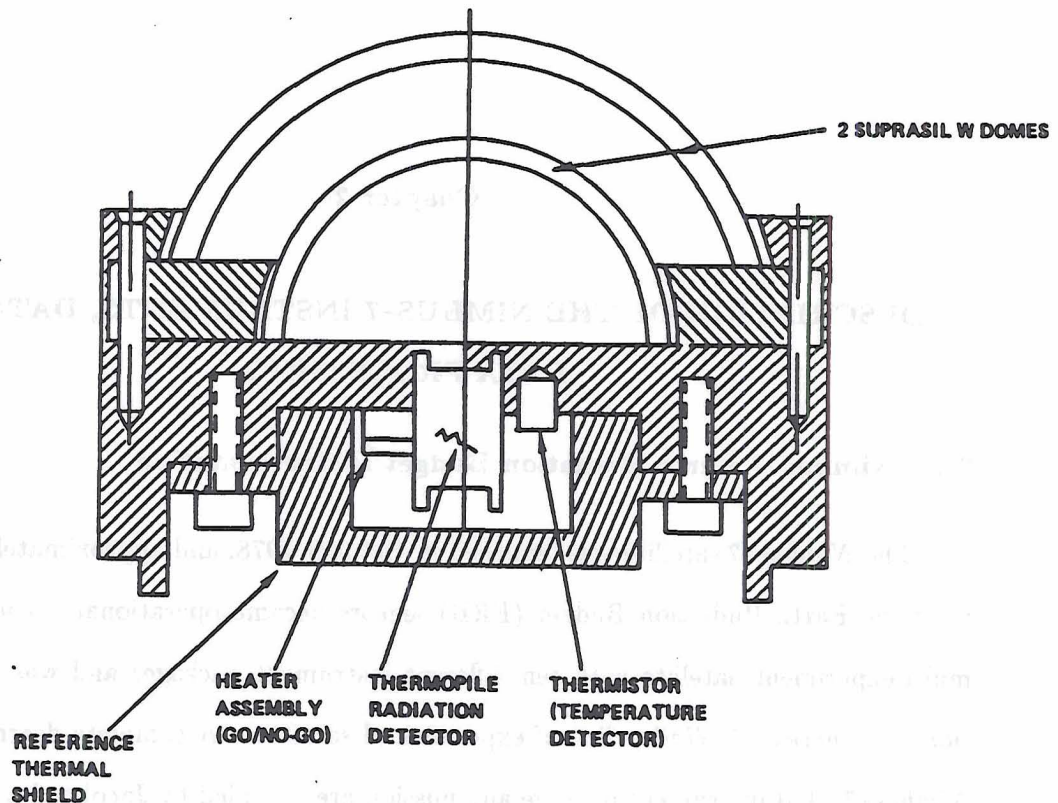


Figure 2.1: Schematic of the fixed hemispheric wide field-of-view radiometers used in the *Nimbus-7* Earth Radiation Budget experiment.

the channel 11 and 12 sensors are the black painted baffles on channel 12. Channels 13 measures the terrestrial flux from the shortwave to the lower end of the infrared, and channel 14 measures the near-infrared flux. A schematic with the basic layout and design of a fixed earth channel radiometer is shown in Figure 2.1. The spectral characteristics of the fixed earth flux channels 11-14 are shown in Table 2.1. The shortwave flux is calculated by differencing channel 13 and 14, the longwave 12 and 13, while channel 14 is used for the near infrared.

The scanning instrument includes channels 15-22. Due to the complex mechanical scanning motor the expected life time of this instrument was only one year. Nevertheless, the instrument lasted 18 months, until June 1980. This narrow Field-Of-View (NFOV) instrument is a telescopic device that an internal mirror chopper wheel to split the signal into the shortwave and longwave sensors. There were four earth pointing scanning telescopes, and therefore four sensors were needed for each spectral interval. The field-of-views of the

Table 2.1: Spectral characteristics of the *Nimbus-7* Earth Radiation Budget experiment channels.

ERB Channel	Instrument type	Spectral interval
10C	Conic blackbody	TOTAL
11	Fixed Hemispheric	$<0.2 - > 50 \mu m$
12	Fixed Hemispheric	$<0.2 - > 50 \mu m$
13	Fixed Hemispheric	$0.2 - 3.8 \mu m$
14	Fixed Hemispheric	$<0.695 - 2.8 \mu m$
15-18:	Chopped Scanner	$0.2 - 4.8 \mu m$
19-22:	Chopped Scanner	$4.5 - > 50 \mu m$

four telescopes were rectangular ($0.25^\circ \times 5.12^\circ$), and the usual scan pattern was oriented perpendicular to the direction of the sub-satellite track. The spectral characteristics of the NFOV scanning channels 15-22 are also shown in Tab. 2.1.

2.2 Earth Radiation Budget Data Selection

There were many reasons for selecting the *Nimbus-7* Earth Radiation Budget (ERB) data for this study. Temporal extent of the data was critical for study of interannual variations and long time series. Nine years of the ERB WFOV data set from November 1978 - October 1987 were used. At this time the data collection continues and the ERB is the last *Nimbus-7* instrument package still operating. The unqualified success of the WFOV instruments lasting more than 11 years far surpassed their design lifetime of 2 years. Concurrent scanning channel data is available for the first 18 months of the experiment until June 1980 when the scanner failed. Due to the limited time of the NFOV data collection, it was not used except in calibration and composite studies. As of July 1989 only a few months of test results from the Earth Radiation Budget Experiment (ERBE) have been released, therefore data from this new experiment could not be included. The *Nimbus-7* WFOV ERB data is the longest ERB data set available from well calibrated broad spectral band instruments (Kyle et al., 1985). Careful post-launch studies of the radiometric qualities of the sensors has allowed for additional calibration applied directly to the primary data (Jacobowitz, 1980). Critical to the calibration success was the exact

understanding of the filter dome degradation and heating while in orbit (Maschhoff, 1984a, 1984b).

To calculate the net radiative balance (NET), it is critical that both the visible and infrared irradiances be as accurate as possible. Another advantage of the *Nimbus-7* data is that all components of the radiative balance, the solar incident, terrestrial reflected, and terrestrial infrared radiation were measured from the same instrument package. These WFOV instruments were designed specifically for collection of ERB data, and therefore no complicated bi-directional estimates of the total flux needed to be added to the data processing. Longwave irradiance can be fairly well estimated from narrow spectral band instruments such as those on the NOAA and TIROS series satellites (Ohring et al., 1984). Much of the success in estimating the total longwave flux from narrow spectral bands is due to the isotropic nature of infrared radiation. This allows the formation of good regression schemes to estimate the total infrared irradiance (Gruber and Jacobowitz, 1985). The NOAA instruments measure the longwave radiance from 10.5 - 12.5 μm , while the TIROS instrument measures from 10.5 - 11.5 μm . The estimated longwave flux is thought to be accurate to within 1 - 3 % (Saunders, et al., 1983).

For two reasons accurate calculation of the visible irradiance from the NOAA satellites is much more difficult. First, the shortwave cannot be considered isotropic, and second, almost half of the radiance is outside the measurement range. The NOAA instruments measure the shortwave radiance from 0.5-0.7 μm , while the TIROS-N instrument measures from 0.55 - 0.90 μm (Gruber, 1977). The NOAA processing does make solar zenith angle corrections to calculate the daily average albedo but TIROS-N assumes the daily average albedo is equivalent to the instantaneous measurements. Due to this and also the the shortwave channel degradation the error in estimating the albedo is much higher near 12 - 15 % (Staylor, 1990). To calculate the NET balance we must have accurate visible and infrared irradiances. These are currently available only from the broadband ERB instruments.

2.3 Defining the Minimum Temporal and Spatial Scale

The WFOV instruments produce sparse data coverage. This causes the greatest uncertainty in using WFOV measurements on time scales of less than a month. Only approximately 15 % of the earth's surface has data coverage for any one day, and averaging the WFOV daily data fields produces more a composite than an average. There is error in assuming that any composite is truly representative of a true average. Defining the minimum number of days to include in the composite, and the limitations of using the composite is the purpose of this section. Creating the composite within acceptable error limits, on as short a time sampling as possible is critically important, since it is the purpose of this thesis to study a long term ERB data set on shorter, weekly time scales. To date other studies which used the *Nimbus-7* WFOV ERB, have concentrated on monthly and annual time scales (Kyle et al., 1986; Ardanuy, Kyle, 1984; Randel et al., 1984; Jacobowitz et al., 1984; Ardanuy, 1983).

An experiment was performed to define the minimum number of days to composite the WFOV daily fields. During the first 19 months of the ERB experiment, both the NFOV and WFOV instruments were operating, which allowed comparisons of the NFOV data rich set to the WFOV data sparse set. Due to its cross track scanning modes, the NFOV data had excellent daily data coverage, sampling almost the entire earth each day. Therefore combining these days together creates a true average with the sample size equal to the number of days. This allows for the use of the NFOV data as the 'truth' fields when compared with the WFOV data. WFOV composites and NFOV averages were calculated for 2,3,4,6,8,12,and 23 day samples for June 1979. Calculation of the Root Mean Square (RMS) difference between WFOV and NFOV with identical sample sizes lets one examine how close the WFOV composite is to the actual average. Figure 2.2 examines the relationship between the number of sample days and the RMS difference for the ascending infrared flux measurement. The errors show a latitudinal dependence for all sample sizes. The largest error occurs near 10° latitude, very near the latitude of the ITCZ. Increasing the number of days in the composite always decreases the RMS difference. The global average RMS for a six day composite is approximately 16-18 Wm^{-2} .

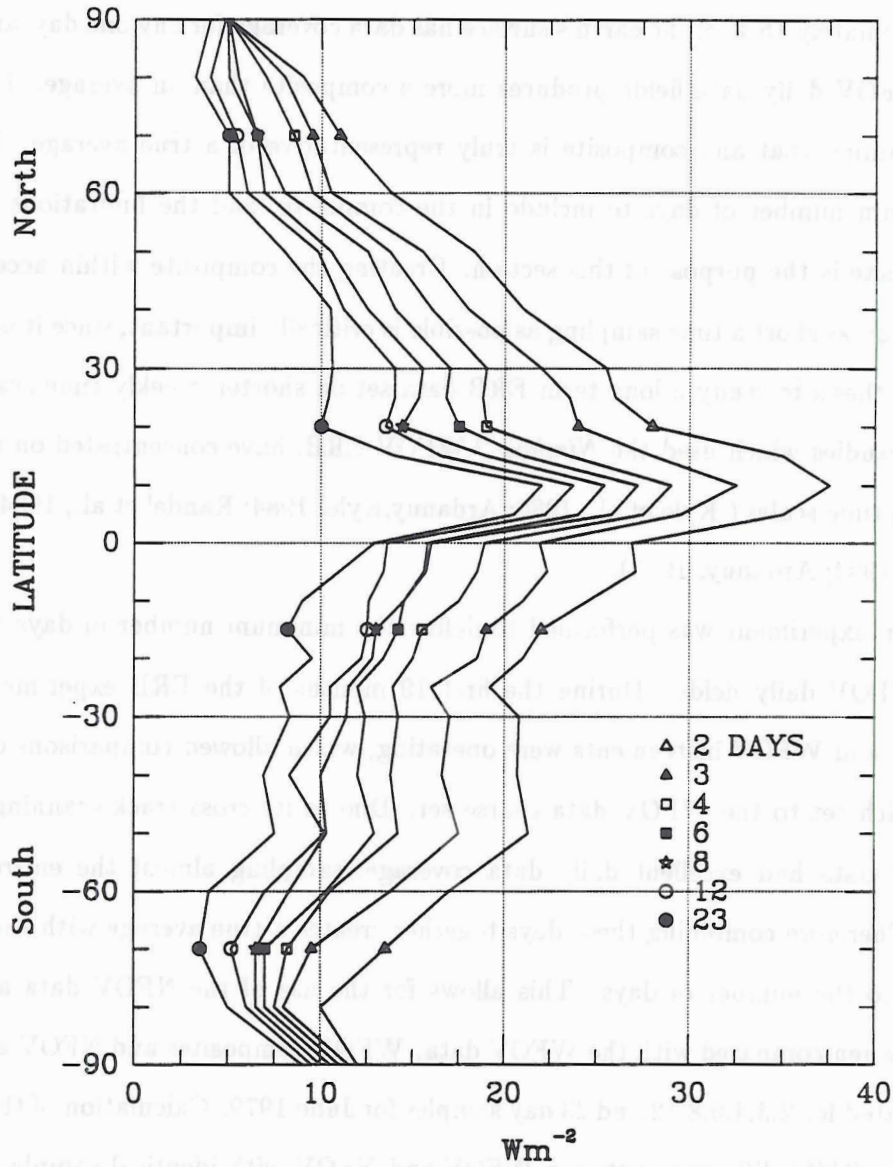


Figure 2.2: Zonal averaged Root Mean Square Difference for the WFOV Composite vs. NFOV. The error over various number of sample days are shown.

Much of this error can be explained by differences in the field-of-view of the instruments. The NFOV scanner can 'see' convection and decreased infrared emission much better than the WFOV. A technique has been developed to get more information out of the WFOV channels by deconvoluting the ERB fields into their spectral components. This technique will be discussed later in the calibration section. RMS difference with and without deconvolution for the six day composite is shown in Figure 2.3. In the tropics and subtropics, where the largest RMS error occurred in Figure 2.2, deconvolution of the WFOV decreases the RMS error. Generally wherever the ERB fields change rapidly either in longitude or latitude, deconvolution will improve the RMS error. Deconvolution also decreases the global averaged RMS for each of the composite samples (Figure 2.4). The global averaged RMS for a 6 day composite after deconvolution is reduced to 12 Wm^{-2} .

There is still some residual zonal bias even after applying the deconvolution process (Figure 2.5) due to the resolution differences of the WFOV and NFOV sensors. If we subtract this, we have a true measure of the RMS error associated with making the composite (Figure 2.6). The six day WFOV composite has fairly consistent $10\text{-}12 \text{ Wm}^{-2}$ error between 45°S - 45°N . Lower errors occur near the poles. Also plotted in Figure 2.6 is the standard deviation of the daily NFOV infrared (IR) flux for the same month. The zones with higher values change more rapidly from one day to the next. These are the same zones which have higher composite vs. average RMS error. Therefore areas which change rapidly must be used with caution when using the WFOV composite data. It was decided that a six day composite was the optimum balance between the RMS error and minimum time period. Very little improvement in RMS error occurred by the eight day composite, which due to the instrument duty cycle, would only produce 3 periods per month. A six day composite does not make a true week because the ERB instrument was not turned on each day. Due to power constraints on the *Nimbus-7* satellite, the ERB instrument followed the required duty cycle of 3 days on, 1 day off. Therefore to create a 6 day composite takes between seven or eight calendar days. Using a six day composite, 45 time periods are produced each year.

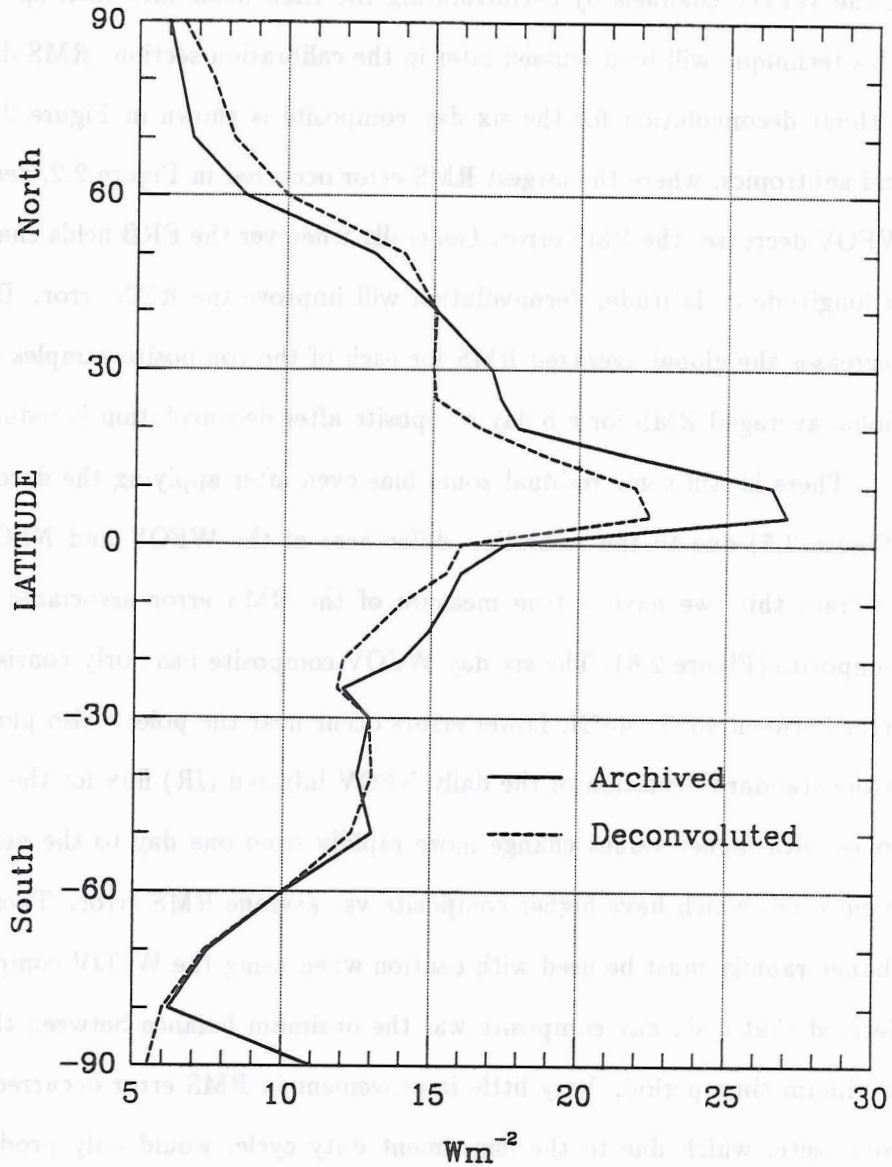


Figure 2.3: Zonal averaged RMS error for the six day composite WFOV OLR with and without deconvolution.

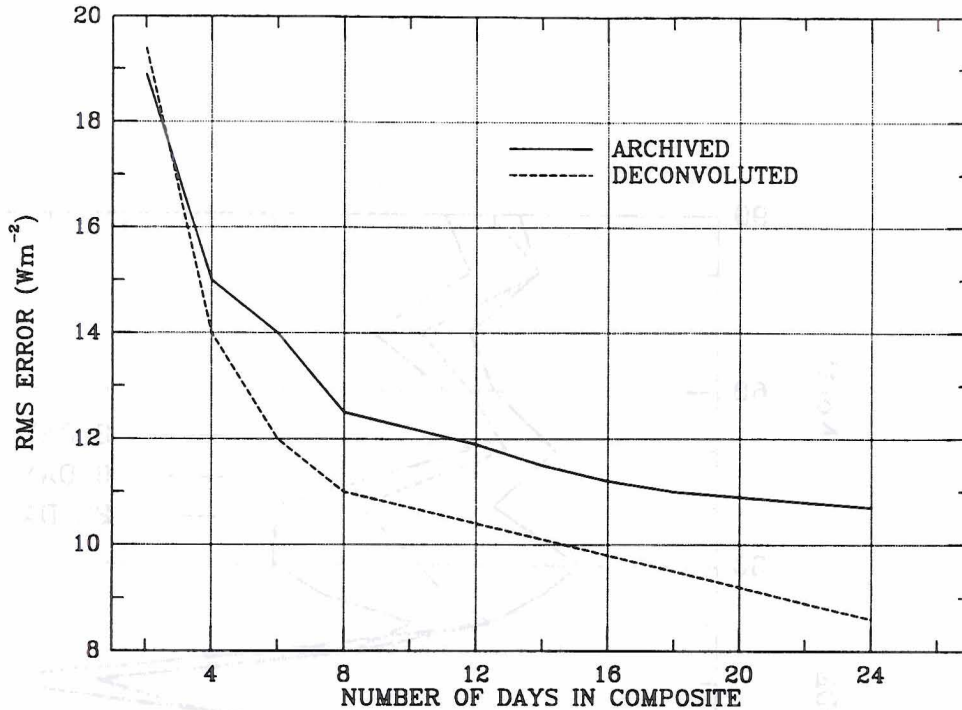


Figure 2.4: Global average RMS for a 6 day sample period with and without deconvolution.

2.4 ERB Data Calibration

The 9 years of *Nimbus-7* ERB data used in this study had at least 3 different official calibration schemes. The first of these was applied during the period when the NFOV scanning instruments were operating. The scanner had internal reference black bodies and comparison checks were made between the WFOV and NFOV radiances. After the scanner failed, a new calibration scheme, the PCAT or Pacific Calibration Adjustment Technique was applied. This calibration was used through year 5 of the data set. Further study of the performance characteristics on the data and instrument degradation while in orbit resulted in corrections to this calibration. These corrections were applied to each month and were termed the RDS calibration and could be applied directly to the reflected and longwave irradiances on the archived tapes (Kyle et al., 1984). Included in this new scheme were corrections for NFOV angular bias, the three days on, one day off cycle (the instrument takes time to reach stability after power up), and the influence of shortwave and longwave radiation on the filter domes and detectors (Maschhoff, et al., 1984b). The

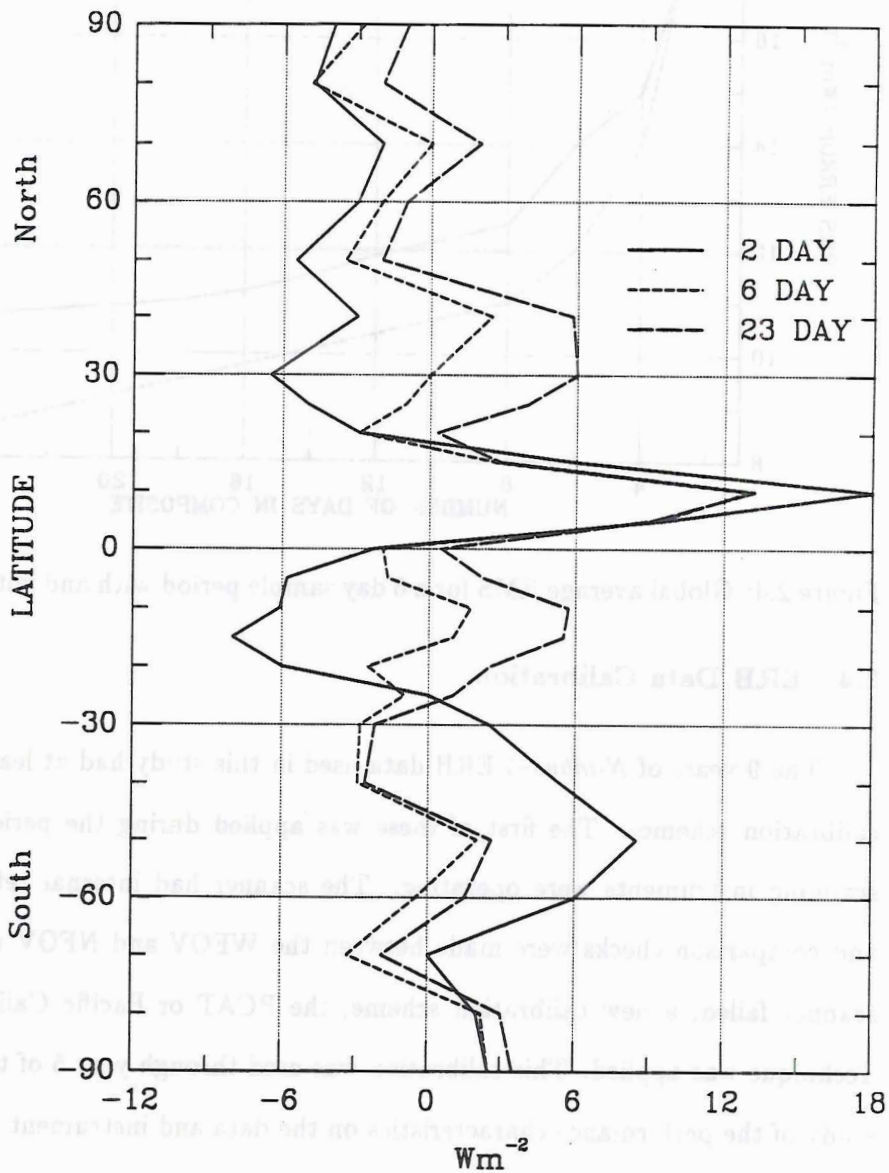


Figure 2.5: Zonal bias of NFOV and WFOV data.

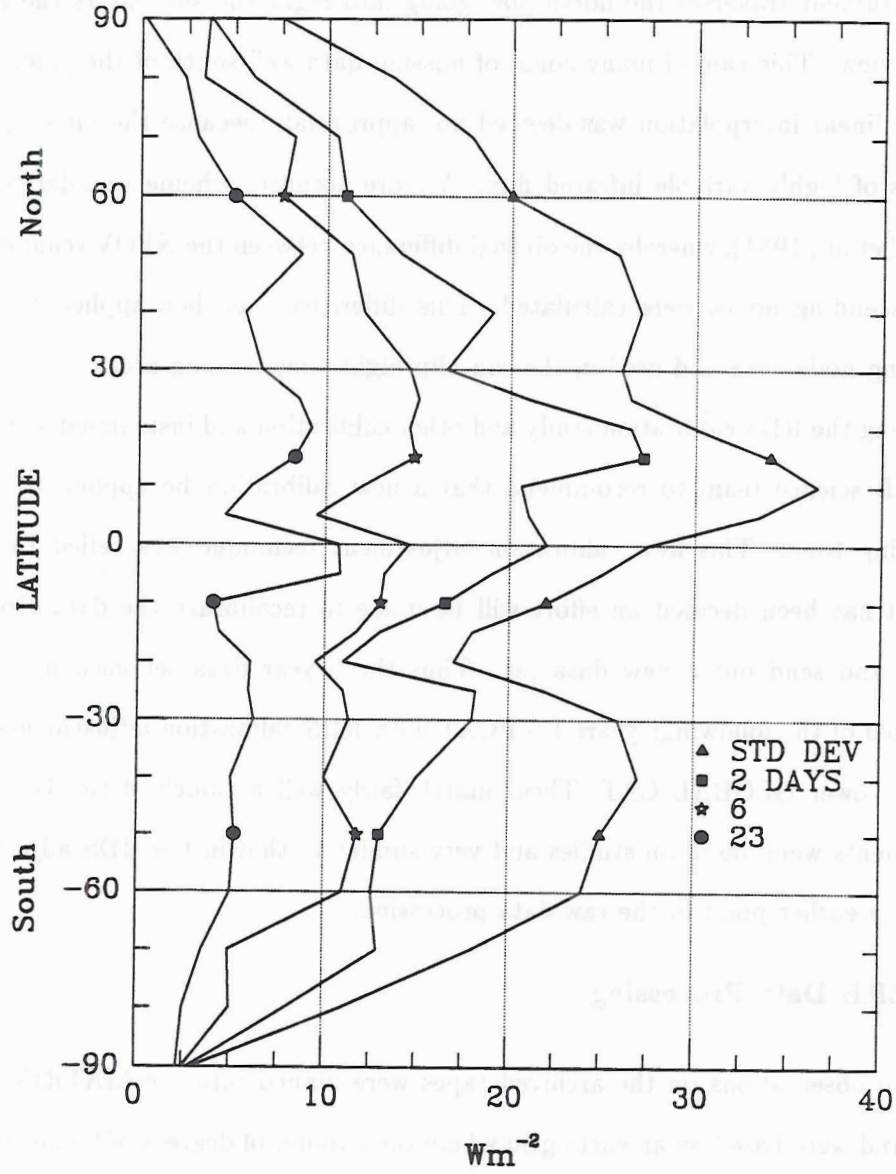


Figure 2.6: Final RMS error after subtraction of WFOV-NFOV zonal bias and with WFOV deconvolution for composite samples.

first five years of archived data were recalibrated at CIRA using the RDS recommended values.

There was also a problem with missing data in the night time infrared flux data. When the instrument traverses the north pole going into night the sun enters the instruments field of view. This caused many zones of missing data well south of the pole. Applying a straight linear interpolation was deemed not appropriate because the missing zones were in areas of highly variable infrared flux. A more accurate scheme was derived at CIRA (Randel et al., 1984), whereby the diurnal difference between the NFOV scanner ascending and descending nodes were calculated. This difference was then applied to the WFOV ascending node data and used in the sun blip night time missing areas.

Using the RDS calibration study and other calibration and instrument studies allowed the ERB science team to recommend that a new calibration be applied to the data at processing time. This new calibration adjustment technique was called the GLOBAL CAT. It has been decided an effort will be made to recalibrate the data already in the archive and send out a new data set. Thus the 9 year data set used in this study is composed of the following: years 1-5 PCAT with RDS calibration adjustments, and years 6-9 the newer GLOBAL CAT. These match fairly well as much of the GLOBAL CAT adjustments were based on studies and very similar to that in the RDS adjustment, only done at a earlier point in the raw data processing.

2.5 ERB Data Processing

The observations on the archived tapes were binned into the MATRIX tape target areas, and were based on an earth grid where the number of degrees of longitude depended on latitude. The purpose was to approximate an equivalent surface area in each target box. All data fields originally were grouped into 2070 target areas of approximately equal 500 km^2 area. During processing at CIRA the fields are stretched into $4.5^\circ \times 4.5^\circ$ grids by simple, but logical interpolation schemes. Thus in the equatorial regions from 18°N - 18°S no interpolation was necessary, but poleward required binning as few as three zonal data points into 80 areas. The interpolation was performed in order to begin the matching

process with the gridded atmospheric circulation data fields as well as other data sets. There were more than thirty different parameters on the archive tapes including NFOV and WFOV data. To create the six day averages, only four of these parameters are used: the infrared flux ascending node (day), infrared flux descending node (night), the daily averaged incident radiation, and the daily averaged reflected shortwave. After applying the necessary calibrations as discussed in the previous section and averaging the six data days, three additional parameters are derived: the daily average infrared flux, the albedo, and the NET balance. The albedo is calculated by simply normalizing the reflected energy by the incident solar radiation. The albedo field is left as the instantaneous local noon time values and no effort is made to form it into a daily average by applying a solar zenith angle correction. The ascending and descending node IR flux data can come into conflict near the date line due to the day-night decision algorithm. The NET balance is calculated as follows:

$$NET = S_0(1 - \alpha) - IR,$$

where S_0 is the solar constant, α the planetary albedo, and IR the outgoing infrared radiation at the top of the atmosphere. After the stretching to a $4.5^\circ \times 4.5^\circ$ field, applying calibration, and compositing, any remaining missing data are filled by various interpolation routines. The largest inconsistency came from filling large blocks of zones that were missing. Generally in these areas there was little or no radiation such as during the polar night. The top two zones from 81.5° to 90° were generally filled by straight interpolation of zonal averages from lower zones. Therefore studies which use high polar zones are limited and when they are included in the analyses are used with caution.

Deconvolution of the WFOV into its first 12 spectral components and then reassembling the components is a common post-processing step. The purpose is to unlock information in the data that has been masked by assigning data into specific bins and to allow the data to better resemble the NFOV observations. This technique has been developed and applied to *Nimbus-6* and *Nimbus-7* data with good results (Smith and Green, 1981; Bess et al., 1981; Campbell and Vonder Haar, 1980a; Ardanuy and Kyle, 1986). The

WFOV instruments measure the integrated radiance at satellite altitude. The inverse square relationship,

$$\left(\frac{r_{sat}}{r_{earth}}\right)^2$$

is applied to calculate the total irradiance at the top of the atmosphere, from the observations at satellite height and the value is binned into an earth located area directly below the satellite. With the half power radius of the WFOV instrument approximately 7° , and since the data is binned into smaller boxes, this in effect applies a spatial filter. Applying the deconvolution process doubles the effective spatial resolution, removes some of the higher frequency noise, and serves to "enhance" the values by increasing the highs and lowering the lows while keeping most lower order statistics relatively consistent. The greatest improvements are seen in the tropics and in the subtropical deserts (Ardanuy and Kyle, 1986) where the radiation is highly variable with longitude. This process was applied to each of the 6 day composites over the 9 year data set. It was decided that applying the deconvolution to individual days and then averaging would not be appropriate due to the large amount of missing data in each day. Instead the deconvolution scheme was used after the composites were created and the missing data fully interpolated.

2.6 Nimbus-7 Derived Cloud Climatology

A global multi-level cloud climatology has been derived, independent from the ERB observations, from two other *Nimbus-7* instruments – the Temperature Humidity Infrared Radiometer (THIR) and the Total Ozone Mapping Spectrometer (TOMS) (Hwang, 1982). The cloud data set started in April 1980, continues for six years, and is referred to as the Cloud-Matrix (CMATRIX) data. The cloud algorithm is a combination of two spectral techniques: The THIR is a scanning radiometer which measures thermal radiation in two spectral bands. The first is from $10.5 - 12.5 \mu m$ in the atmospheric window region, used for retrieval of cloud-top, land and ocean surface temperature. The second channel from $6.5 - 7.0 \mu m$ is used in the measurement of middle and upper tropospheric moisture. The TOMS instrument measures the backscattered ultra-violet radiation in six wavelengths. Two of the TOMS channels, at 0.313 and $0.38 \mu m$, are used to compute a directional

albedo at different levels in the atmosphere (Heath et al. 1978). During the daytime (ascending node) passes both the shortwave algorithm from TOMS and the longwave algorithm from THIR are used in the cloud retrievals. During the night time passes, (descending node) only the THIR longwave algorithm is used. The cloud algorithms, methods and limitations are completely described by Stowe et al. (1988). Also included in the cloud algorithm are terrain, snow, ice, and surface temperature analysis from the Air Force 3-D Cloud Nephanalysis which are used to compute a cloud/no cloud threshold. Global cloud amounts for three different levels (high, middle and low), and estimates of cirrus, warm and deep convective clouds are produced for daily as well as monthly means. The data are conveniently binned into matching geographical areas as ERB with identical temporal averages of daily and monthly means which allows easy comparisons between these data sets. The data bins are approximately equal 500 km^2 areas, with $4.5^\circ \times 4.5^\circ$ resolution from 18°N to 18°S and wider longitudinal degree grid spacing toward the poles. The cloud threshold level that separates the low and middle clouds is 2 km above mean sea level. The threshold between middle and high levels is set at 7 km and is constant equatorward of 30° . This boundary level decreases poleward with increasing latitude following the decrease in the tropopause thickness. In following chapters the long time series and global coverage of this cloud climatology will provide an ideal tool for examination of cloud changes with concurrent ERB anomalies.

Chapter 3

EXAMINATION OF THE EIGHT YEAR NIMBUS-7 EARTH RADIATION BUDGET DATA SET

This chapter examines the *Nimbus-7* ERB data set. Understanding the processes of collection, calibration, and averaging discussed in the previous chapter are only the first step in retrieving useful information. We must also carefully examine the final data products for full understanding of their limitations and errors. Much of this examination has already occurred leading to the new calibration schemes. Our starting point in this task will be a long term eight year average then a progression will occur to shorter time scales.

3.1 Eight Year Nimbus-7 Averages

The *Nimbus-7* data set used in this study was from the wide Field-Of-View (WFOV) instruments. These are hemispheric dome instruments which have a large observing 'foot-print'. Thus even at daily time scales the data tend to appear smoothed or averaged and void of small scale cloud features. For these studies the first eight years of the *Nimbus-7* data set are used. When the radiation fields are averaged for each day over eight years, we are left with only the largest scale radiation features.

3.1.1 Global average values

The global averages for the first eight years of the data set are presented in Table 3.1. The global averaged local noon, local midnight and daily average outgoing longwave radiation (OLR) observations were 237.3, 232.3, and 235.2 Wm^{-2} respectively. The OLR was 5 Wm^{-2} greater during the day than at night, with a slightly larger diurnal difference

Table 3.1: *Nimbus-7* Earth Radiation Budget global averages for the eight year data set from 11/78 – 10/86. All values are in Wm^{-2} except albedo which is in %.

ERB Parameter	Global Average	N. Hemisphere	S. Hemisphere
IRF DAY	237.3	237.9	236.8
IRF NIGHT	232.3	232.0	232.6
IRF DAY+NIGHT	235.2	235.3	235.0
ALBEDO	31.3	31.9	30.7
NET BALANCE	4.5	2.2	6.7
IRF DAY-NIGHT	5.0	5.9	4.2

(by 2 Wm^{-2}) in the Northern Hemisphere (NH). This was most likely due to strong continental heating during the day, evident by the greater daytime flux in the NH. Likewise the midnight OLR was higher in the Southern Hemisphere (SH), again pointing to cooler emitting NH continents at night and predominately warmer SH oceanic emission. The global averaged albedo was 31.3 %, in good agreement with previously experiments, and was 1.2 % lower in the SH due to the large percentage of low reflectivity ocean surface. These differences are additive when the NET balance is calculated, thus causing the SH radiative balance to be 4.5 Wm^{-2} greater than the NH. This would imply a cross-equatorial energy flow from south to north when annual averages are compiled.

The global averaged NET does not equal zero, but rather 5 Wm^{-2} , and there are many possible places to look for the cause. The most probable place to start, would be with the incident radiation measurement. As was mentioned in the last chapter the measurement of incident radiation was made by channel 10C, a conic cavity radiometer. At the time of launch this was the most accurate instrument ever flown in space to measure this quantity. A later launch of the Solar Maximum Mission (SMM) satellite allowed for measurements from other total solar instruments. The SMM results suggested that the *Nimbus-7* channel 10C instrument and the value of the solar constant used in the *Nimbus-7* processing was too high by approximately $6-7 \text{ Wm}^{-2}$ too high. However relative changes agreed with great accuracy. With a annual albedo of near 31 %, this would make up 3.0 out of the 4.5 excess watts. Additional error may be present in the shortwave and/or

longwave measurements due to a systematic bias that was not removed in the processing. Also we know that when the satellite moves from night into day the sensors were exposed to sunlight for a short period of time and this SH measurements. Finally some short term climate variability may have occurred. It would not be unreasonable to assume that $1\text{--}2\text{ Wm}^{-2}$ may have been absorbed into the oceans on such a short climatic time scale of only 8 years.

3.1.2 Outgoing Longwave Radiation – OLR

Shown in Figures 3.1 and 3.2 are the global distribution of longwave radiation for the local noon and midnight observations. A short description of the major features follows. The polar regions emit much less than the tropics and mid-latitudes, with the south pole less than the north. The subtropical desert regions emit the most radiation, and the earth maximum occurs over the Saudi Arabian peninsula. Strong local maximums also occur over the desert regions of western Australia and below the equator in the clear subtropical subsidence regions off the west coasts of South America and Africa. The equatorial continents, including the marine continent of Indonesia, tropical South America and central Africa have decreased emission due to their persistent convective cloudiness. OLR as low as 220 Wm^{-2} occurs during the night over these areas. Areas where there are large gradients of longwave or other input energies are of great importance because of the atmospheric circulations driven by this variability.

In some areas the magnitude of the equator to pole gradients are equivalent to that measured over much smaller distances meridionally. As an example, between the South America tropical convective regions and the north pole the OLR gradient measured approximately 50 Wm^{-2} , the same magnitude as measured to the clear or stratiform region only 1500 kilometers off the west coast. It is no wonder there are strong meridional circulations across the Pacific ocean at these latitudes. Poleward of 30° the patterns are much more zonal, but in the NH continental effects are still present. The east Asian continent clearly shows decreased emission both during day and night compared to the relatively warm emitting western Pacific ocean. The effect is pronounced at night when the land values are even less. However the oceans in the NH eastern Pacific are much cooler and

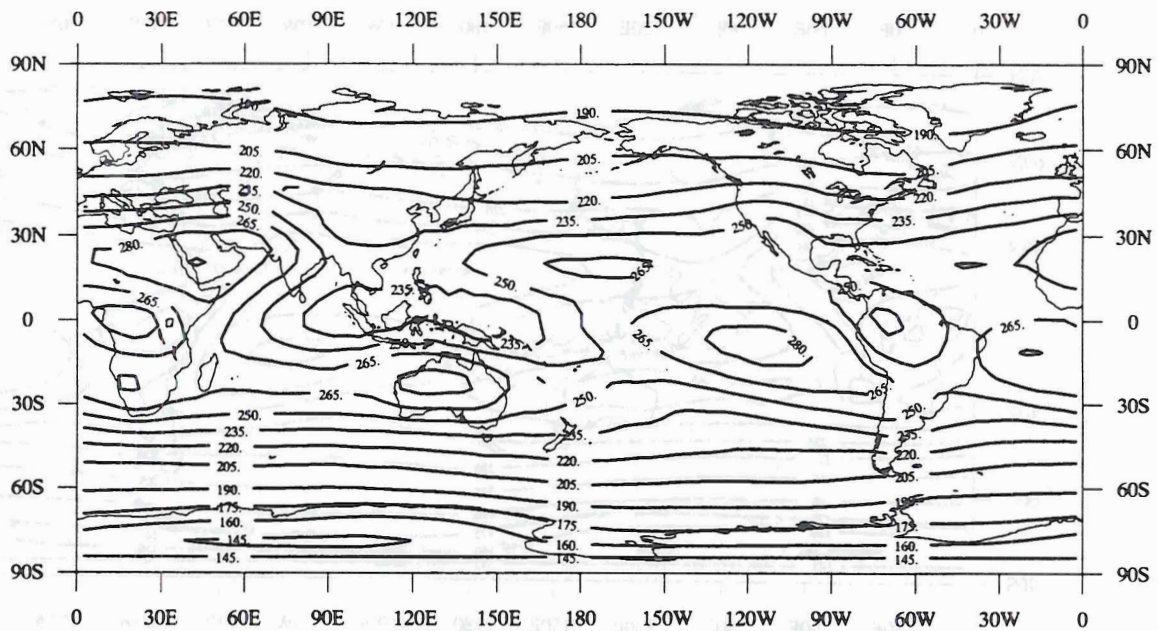


Figure 3.1: Global distribution of DAY time ascending node orbits outgoing longwave radiation (Wm^{-2}) from 11/78 - 10/86.

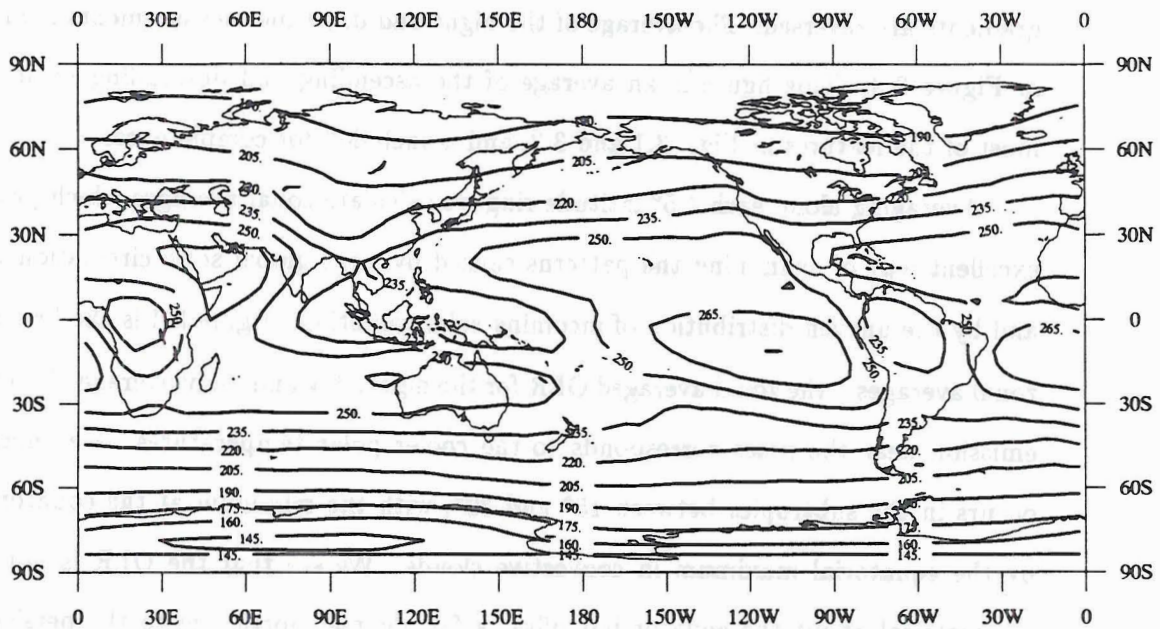


Figure 3.2: Global distribution of NIGHT time descending node orbits outgoing longwave radiation (Wm^{-2}) from 11/78 - 10/86.

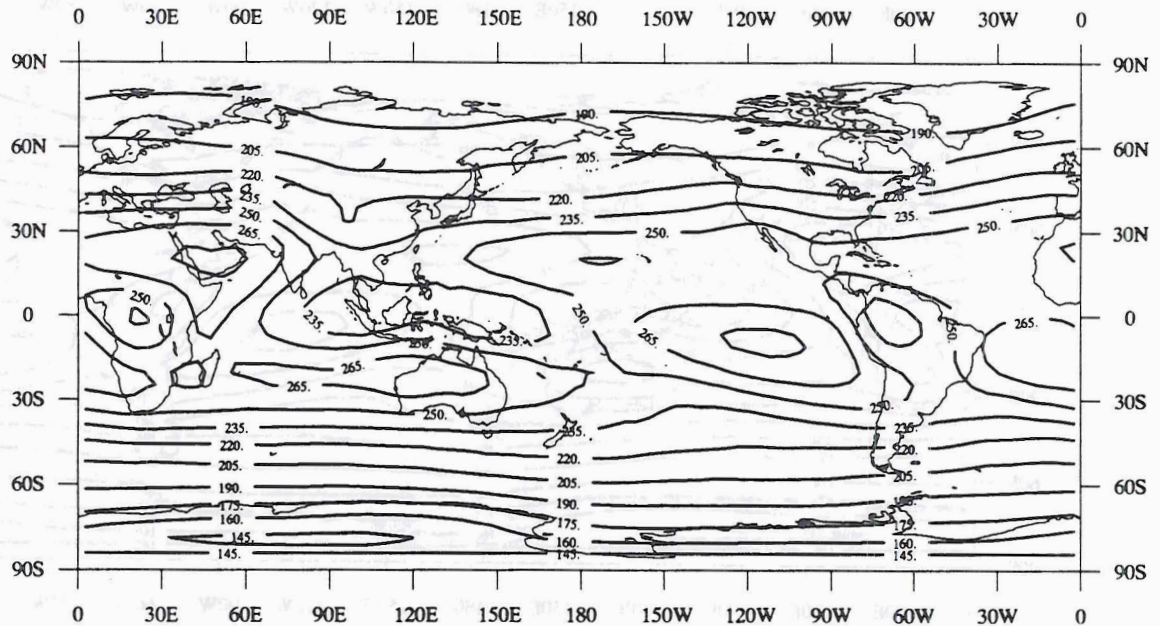


Figure 3.3: Global distribution of daily averaged outgoing longwave radiation (Wm^{-2}) from 11/78 – 10/86.

when the land in the southwest deserts of the U.S. and Mexico heats up during the day, the gradients are reversed. The average of the night and day time measurements is presented in Figure 3.3. This figure is an average of the ascending and descending orbits, shows most of the features in Figs. 3.1 and 3.2, and is included for completeness.

Averaging along each 4.5° latitude ring we calculate zonal averages which provide an excellent way of examining the patterns caused by large global scale circulation features and by the uneven distribution of incoming solar radiation. Figure 3.4 is the first of these zonal averages – the zonal averaged OLR for the night, day and daily average. Much cooler emission near the poles corresponds to the cooler polar temperatures. Maximum OLR occurs in the subtropics between 15° and 30° , with the minimum at the equator caused by the equatorial maximum in convective clouds. We see that the OLR is not exactly symmetrical about the equator but offset a few degrees north due to the persistence of the Pacific ITCZ in the NH. Much cooler emitting temperatures in the south polar region cause the OLR to be 40 Wm^{-2} less when compared to the arctic region.

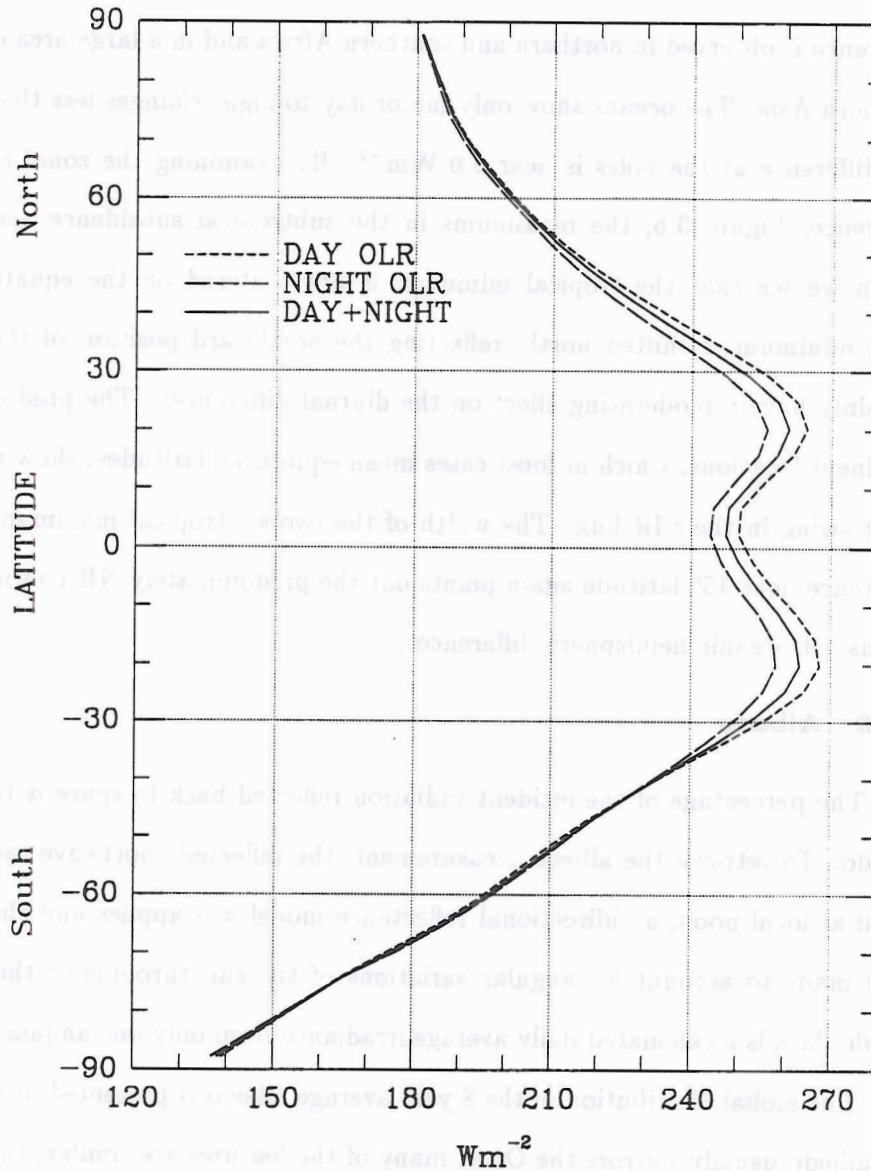


Figure 3.4: Zonal averaged outgoing longwave radiation (Wm^{-2}) from 11/78 - 10/86.

By subtraction of the day and night OLR fields we produce a map of diurnal difference, Figure 3.5. In this figure, the effects of daytime heating and nighttime cooling are readily seen. All diurnal variation over 8 Wm^{-2} occurs on the continents, with the largest reaching a maximum of 30 Wm^{-2} in the dry subtropical regions of Australia. Over 20 Wm^{-2} difference is observed in northern and southern Africa and in a large area covering most of southern Asia. The oceans show only minor day to night changes less than 3 Wm^{-2} , and the difference at the poles is near 0.0 Wm^{-2} . By examining the zonal averaged diurnal difference, Figure 3.6, the maximums in the subtropical subsidence zones are evident. Again we see that the tropical minimum is not centered on the equator, but like the OLR minimum is shifted north, reflecting the northward position of the ITCZ. Clouds certainly have a moderating effect on the diurnal differences. The predominately cloudy continent locations, which in most cases mean equatorial latitudes, show much less day to night swing in their IR flux. The width of the two subtropical maximums as well as the difference near 45° latitude again points out the predominately NH continent hemisphere versus SH oceanic hemisphere differences.

3.1.3 Albedo

The percentage of the incident radiation reflected back to space is referred to as the albedo. To retrieve the albedo measurement, the reflected shortwave radiance was measured at local noon, a bidirectional reflectance model was applied and then modifications were made to account for angular variations of the sun throughout the day. Thus the albedo data is a calculated daily average irradiance from only one angular observation per day. The global distribution of the 8 year average albedo is presented in Figure 3.7. Since the albedo usually mirrors the OLR, many of the features are similar, though reversed in relative magnitude. A description of the the major features follows. In general the albedo is highest in the poles where high reflectivity snow and ice reside year round. Albedo values above 70% are calculated poleward of 70° latitude. The albedo poleward of 80° is suspect due to a combination of high viewing angle and data processing which often creates missing data in these zones. The annual averaged polar values also may be slightly low as the albedo measurement can only be made in these high latitude areas when there

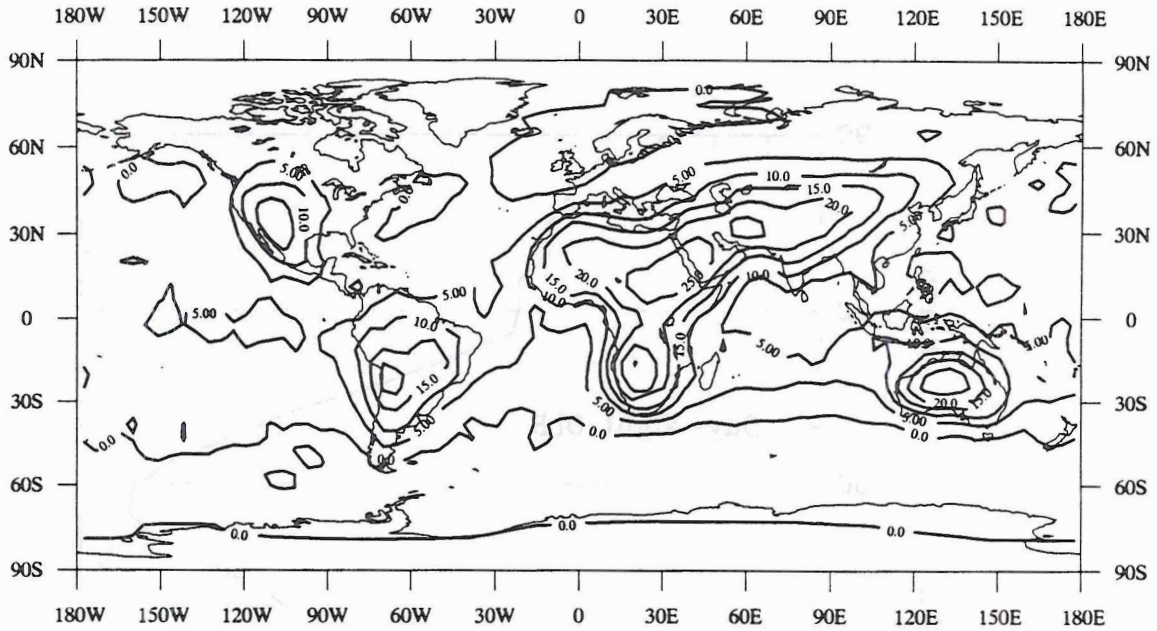


Figure 3.5: Global distribution of outgoing longwave radiation (Wm^{-2}) diurnal variability from 11/78 - 10/86.

is incident radiation. Therefore the annual averaged albedo is not an actual average of the reflectivity of the surface, but also a measure of the average amount of radiation reflected during the year. The albedo in the mid-latitudes is 30 - 60%, with continental areas higher than equivalent latitude ocean areas. Very little meridional variation is apparent from 40° N to the north pole and from 35° S to the south pole. Minimum albedo values occur in the tropical ocean subsidence areas where a lack of clouds combines with the dark ocean surface for albedo values less than 25%. The Sahara desert and Tibetan plateau have albedo of 40-45% but for much different reasons as the predominately clear sky, light sand of the Sahara and the winter snow coverage of Tibet lead to similar annual averages. The equatorial convective regions albedos are slightly lower, measuring 35 to 40%.

The zonal averaged albedo is shown in Figure 3.8. Here the increase toward the poles, the minimum in the subtropical clear areas, and slight increase in the equatorial region are seen. We might expect the increase, due to equatorial cloudiness, to be greater but the ITCZ moves throughout the year and therefore when averaged, smooths out this feature. Higher resolution scanner instruments discern the location of the ITCZ with much better

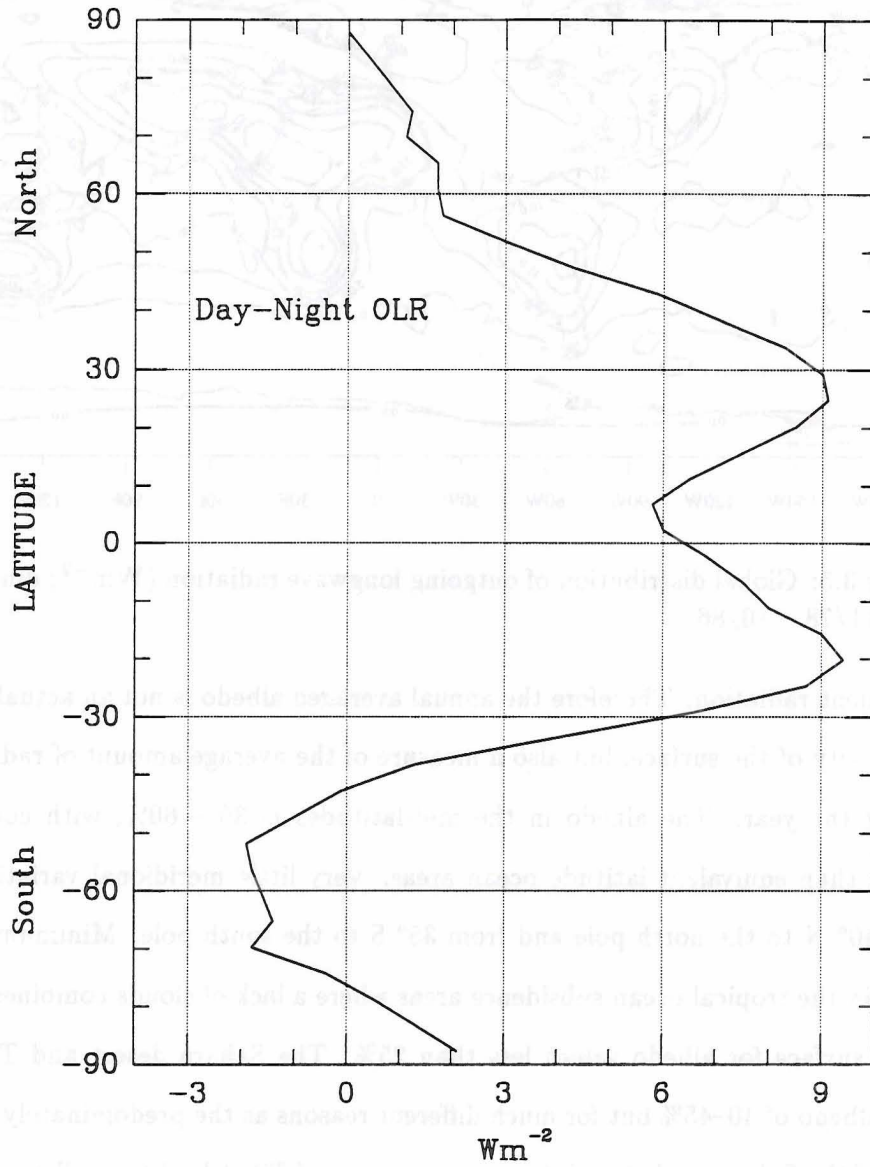


Figure 3.6: Zonal average of the diurnal variability outgoing longwave radiation (Wm^{-2}) from 11/78 - 10/86.

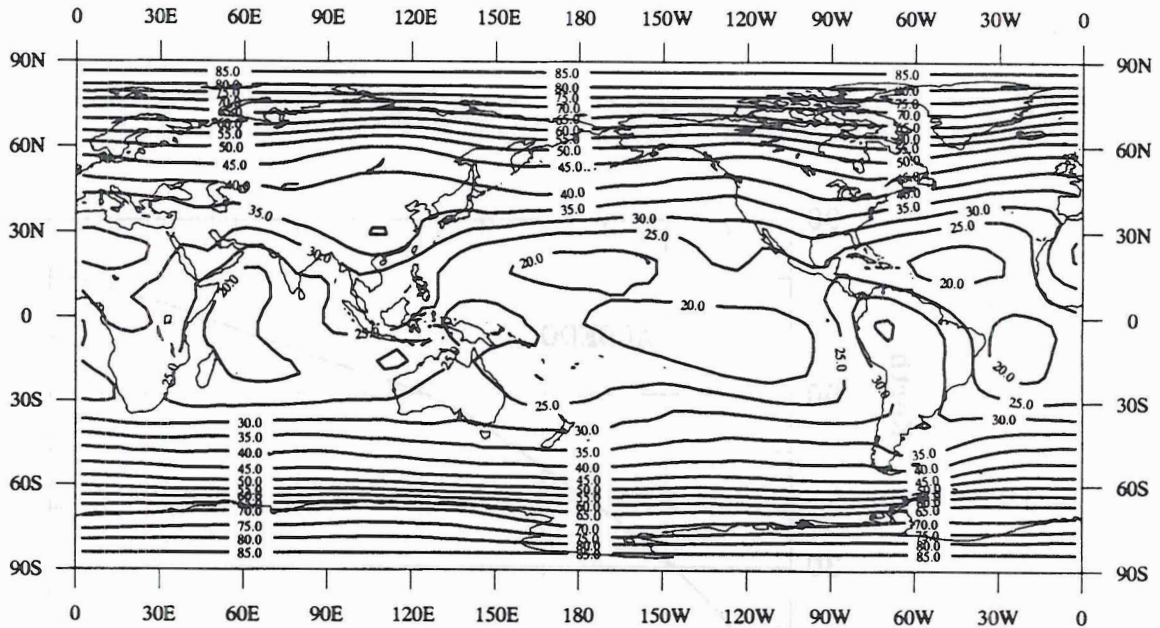


Figure 3.7: Global distribution of daily averaged albedo (%) from 11/78 - 10/86.

accuracy and therefore their increase near the equator is much more pronounced. This is another example where caution must be taken in examining the results from the WFOV instruments as they cannot sense smaller than regional scale cloud variations.

3.1.4 Net radiation balance

The radiative balance (NET) is calculated as the difference of the absorbed and emitted radiative fluxes. Where this value was positive we have a surplus of radiation and where negative there is a deficit. Figure 3.9 presents global map of the NET parameter. We know the surplus of energy in the tropics and the deficit at the poles drives our atmospheric circulation, so it comes as no surprise to see that positive NET occurs in most areas equatorward of 35° north and 40° south latitude. In general, only negative NET values occur poleward of these latitude. The greatest exception occurs in the Middle East and Saharan deserts. Charney, 1975; Campbell, 1980b and others have shown, by calculating atmospheric transports, these subtropical desert regions operate at a radiative deficit, and are heat sink regions rather than heat producers. This deficit is caused by the high albedo characteristics of the surface and generally clear skies. Thus minimum

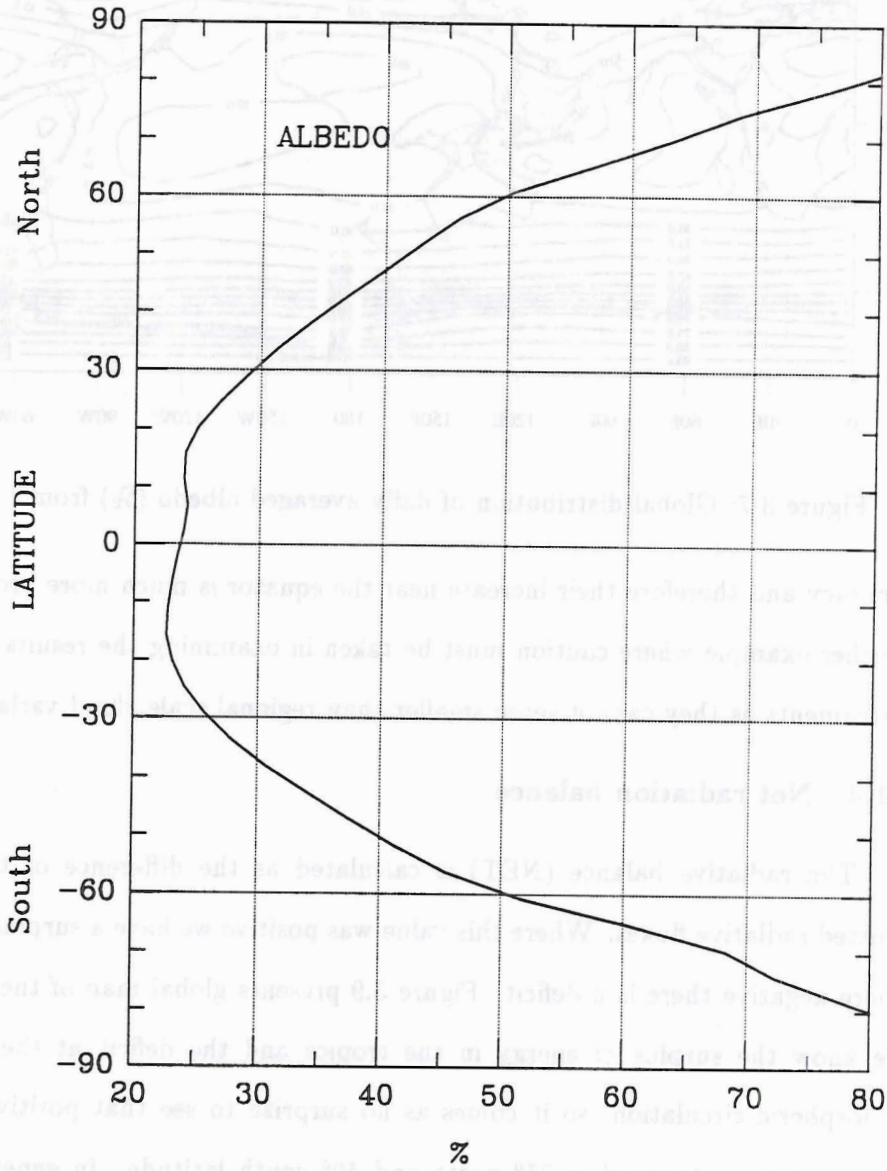


Figure 3.8: Zonal averaged albedo (%) from 11/78 - 10/86.

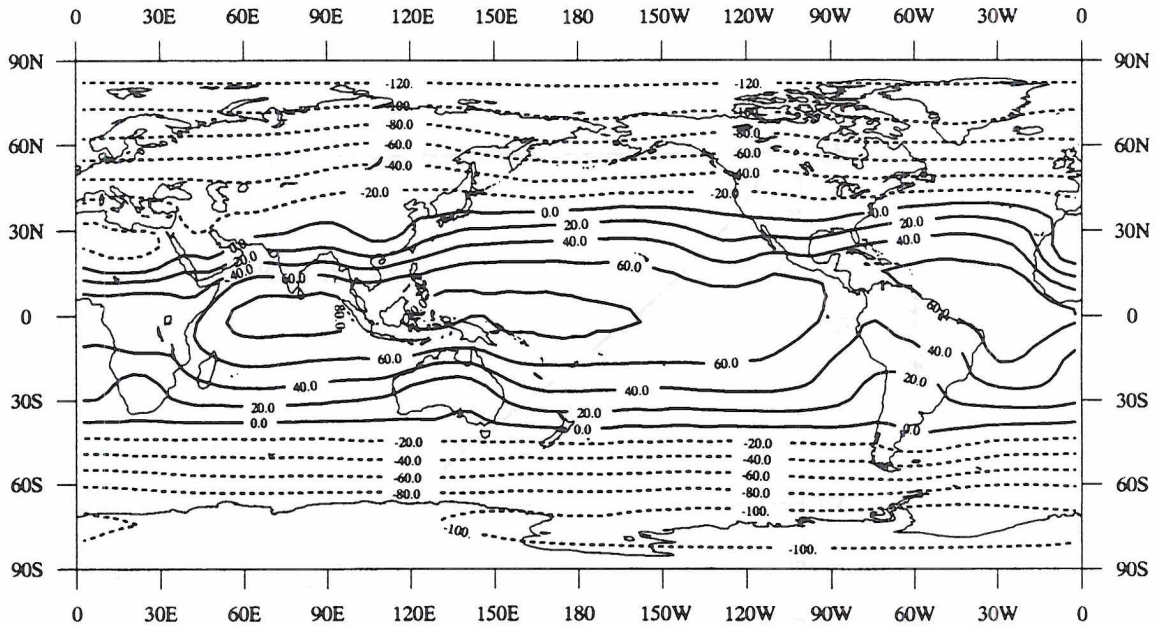


Figure 3.9: Global distribution net balance (NET) (Wm^{-2}) from 11/78 – 10/86.

energy is absorbed during the day but maximum emission occurs during all 24 hours. The NET has a very severe annual cycle due to its dependence on the incident radiation, but the 8 year average shown in Fig. 3.9 is severely smoothed by the large amount of data in the average. The largest NET excesses occur along the equator in the Indian Ocean and in the western Pacific between 120°E and 160°W longitude. Minimums are found in the polar regions with the NET at the south pole 20 – 30 Wm^{-2} less than in the north. This is caused by a cooler Antarctica surface emitting less OLR, and a higher incident radiation during SH summers. We again see that energy gradients, as in the OLR, are not limited to a simple north-south orientation. The variations in cloud cover in the tropics and subtropics can cause large meridional gradients as well. The next section will discuss more on the NET balance gradients and how they were affected by the continents. The zonal averaged NET balance, Figure 3.10, displays many of these large scale features: the excess at the equator, the loss at the poles, the hemispheric difference of the zero line, and the south pole versus north pole variations.

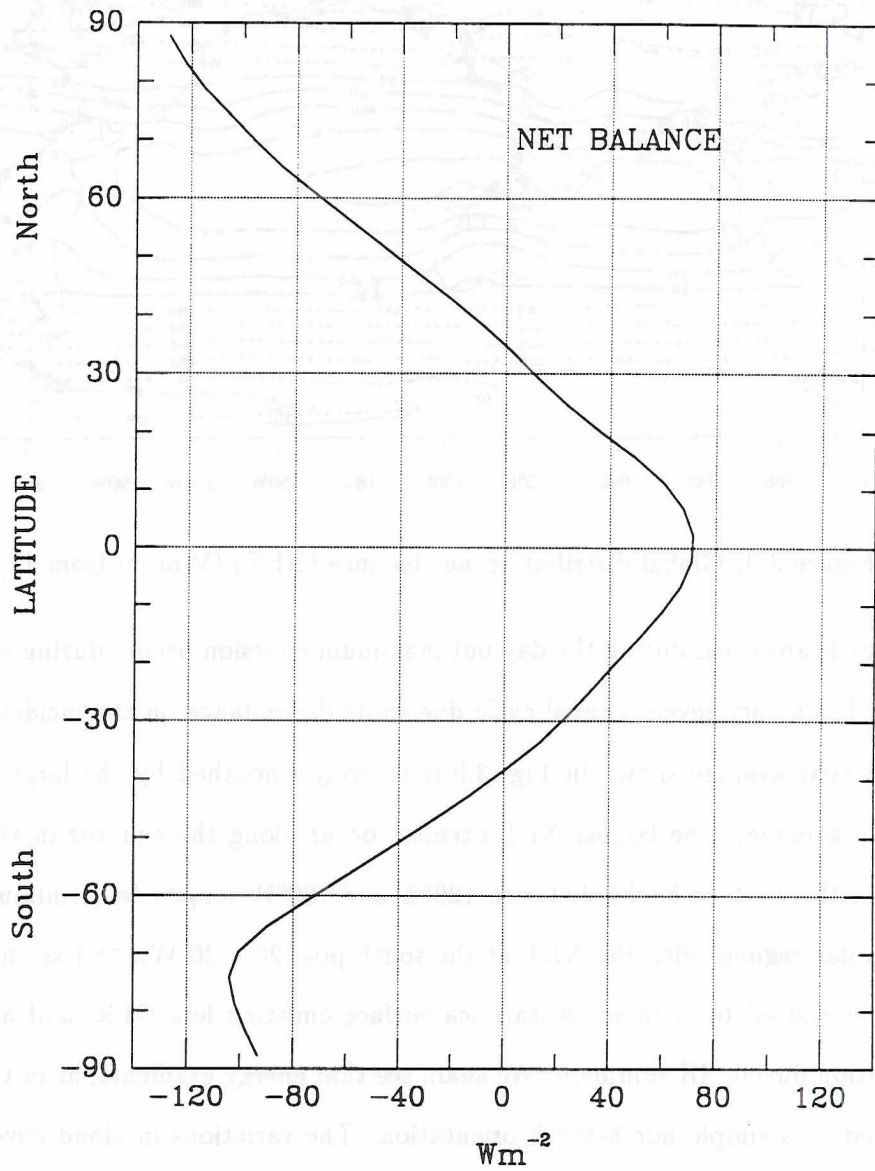


Figure 3.10: Zonal averaged of the net balance (NET) (Wm^{-2}) from 11/78 - 10/86.

3.1.5 Southern Hemisphere 'three wave pattern'

In the SH an interesting 'three wave pattern' was observed when a decrease in NET occurs over and to the west of all three continents (See Fig. 3.9. Examination of this pattern was examined in Randel et al. (1984). It was shown to be caused by both the influence of stratiform cloudiness and continental heating. Variation in the NET occurs identically in the NH over the continents but it does not create such a striking feature due to the complexity, at $35^{\circ} - 45^{\circ}N$, of the ocean/land interaction. From the NET balance equation we know the NET can be decreased relative to surrounding areas in two ways: first the reflected energy can be increased, and second the OLR can be increased. Therefore quite different mechanisms can appear to cause the same effect, and both of these mechanisms do occur in different locations resulting in the SH 'three wave pattern'. Figure 3.11, presents an estimate of the longitudinal decrease of the NET for each month, and for each of the "wave" areas. Each value represents the difference of the NET between two areas: one outside of the wave far from the continent, the other located within the wave close to the continent.

We can see that along South America, the contribution to the decrease in the NET was quite regular each month. This consistency is caused by the persistence of the western stratocumulus region and its' associated increase in albedo. There was only a hint of an annual cycle with the minimum in February and maximum in October. Upon examination of the south African pattern we see there much more of an annual cycle, but again the spring increase in stratiform cloudiness is clearly seen. In each case the effect on the wave pattern was caused by an increase in the albedo. There was little change in the albedo over the third wave over the Australian continent. The Australian pattern was unique because only for a few months of the year, in the SH summer, was there any contribution to the annual wave pattern. Therefore this wave was caused by the increase in OLR during these months. The NET radiative balance can be a informative parameter but care must be taken to understand the individual radiative processes that make up the balance. These components need to be examined individually.

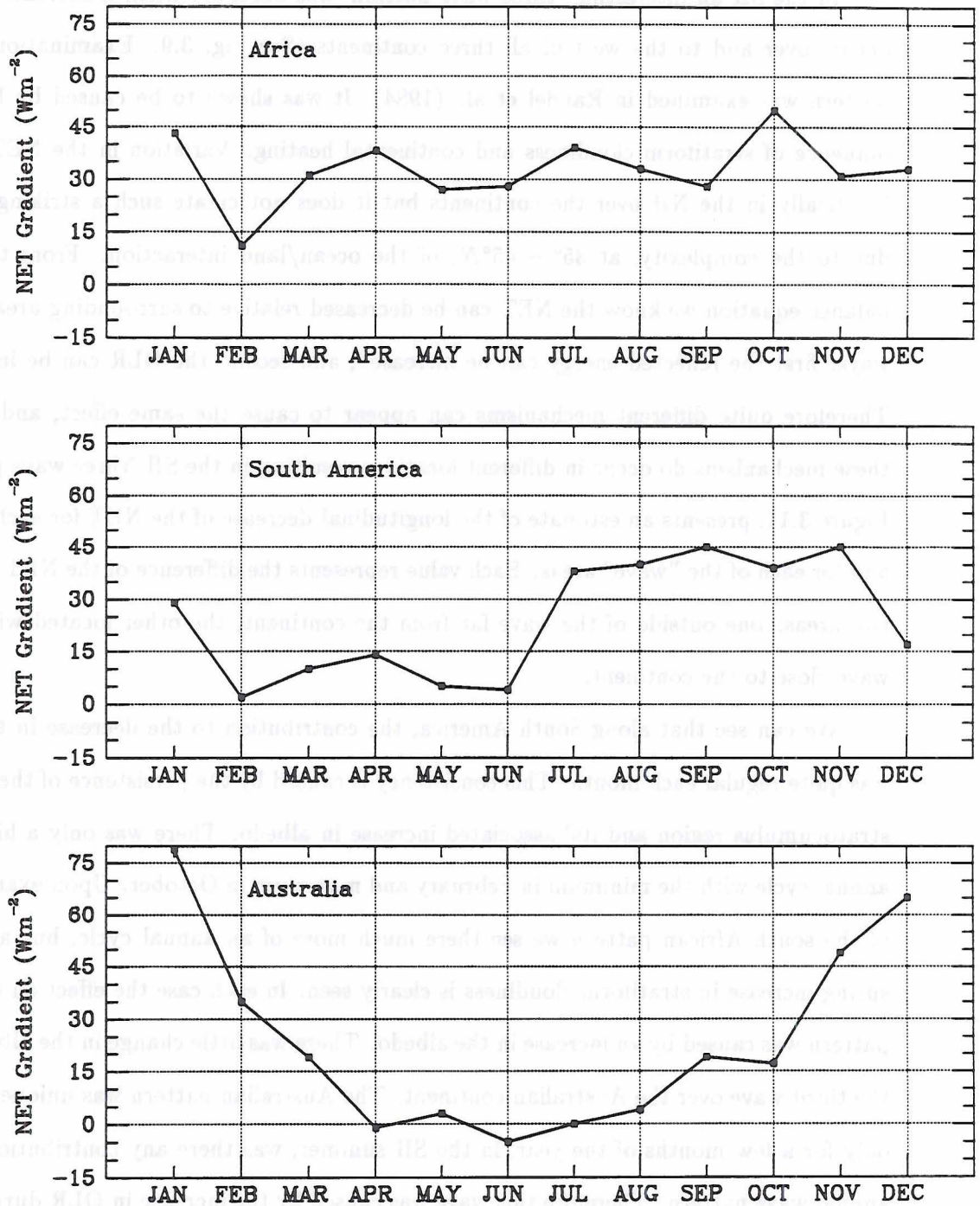


Figure 3.11: Gradient (Wm^{-2}) in the NET between an area inside the "wave" and a point outside for the three areas.

3.1.6 Required total energy transport

Using the NET balance results we can calculate the estimated total poleward energy transport. This was previously calculated using observations from a variety of satellites (Vonder Haar and Oort, 1973; Oort and Vonder Haar 1976; Carissimo et al. 1985). The energy budget including both oceans and atmosphere for a unit width latitude band is described by:

$$NET = \frac{\partial(T_A + T_O)}{a\partial\theta} - \frac{\partial E_A}{\partial t} - \frac{\partial E_O}{\partial t},$$

where $\frac{\partial E_A}{\partial t}$ is the rate of storage in the atmosphere and $\frac{\partial E_O}{\partial t}$ is the rate of storage in the oceans. It was recognized in earlier studies that integrating over the polar cap to obtain the poleward transport of total energy may lead to uncertainties at the opposing pole. To make certain that the flux is zero at both poles, corrections were made as in Carissimo et al. (1985), to account for the excess energy calculated after integration. Annual averages of NET were used so that as a first approximation the storage terms in the atmosphere and oceans could be set to zero. The final correction varies with latitude, takes into account the uncertainties in the diurnal cycle of reflected radiation, and has the form:

$$T(\theta) = T_{np}^*(\theta) - \int_{\theta}^{\frac{\pi}{2}} \frac{T_1}{\pi^2 a^2} 2\pi a^2 \cos^2 \theta d\theta,$$

where T_{np}^* is the uncorrected flux values starting with integration at the north pole. The zonal average total transport for the 8 years is presented in Figure 3.12 and shows the symmetry about the equator similar to the pattern of NET radiation. For both the northern and southern hemispheres the maximum value of poleward transport occurs from 33 – 38°. The NH maximum is higher than the SH, $6.0 \times 10^{15} \text{W}$ compared to $5.6 \times 10^{15} \text{W}$. The maximum transport values are slightly higher than previously reported Vonder Haar and Oort, (1973), and in Ellis and Vonder Haar, (1976), but are slightly lower than those calculated using the *Nimbus-7* scanning instruments by Jacobowitz et al. (1979).

The zonal averaged values for each of the parameters discussed above are presented in Table 3.2. Also the diurnal difference and the calculated required total energy transport are listed in Table 3.3. The *Nimbus-7* data processing binned the observations into 4.5° latitude zones. Therefore this is the spacing of the zonal averaged values. Each latitude value specified is at the center of the zone.

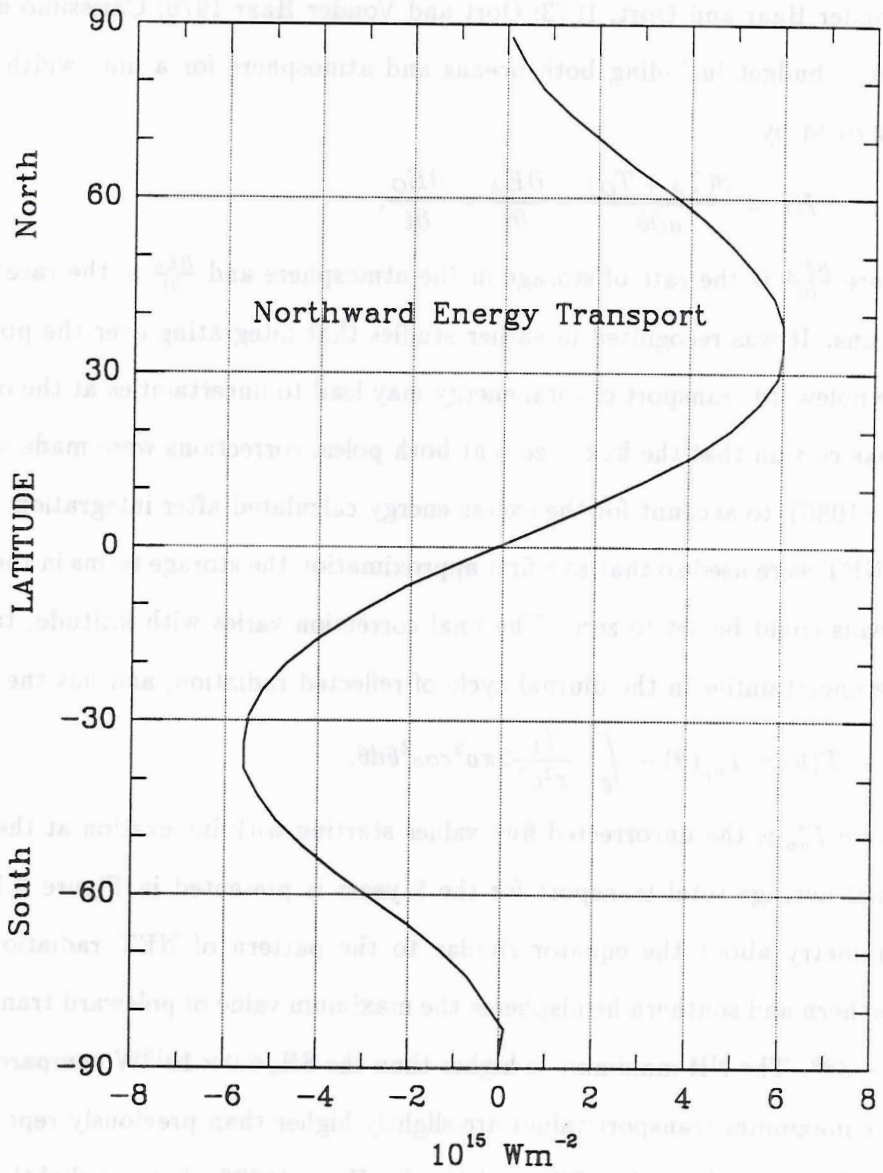


Figure 3.12: Total atmospheric transport derived from the *Nimbus-7* net balance from 11/78 - 10/86. Values are in 10¹⁵Wm⁻².

Table 3.2: *Nimbus-7* Earth Radiation Budget zonal averages for the eight year data set (11/78 - 10/86). All values in Wm^{-2} .

LATITUDE	INFRARED FLUX DAY	INFRARED FLUX NIGHT	INFRARED FLUX AVE	ALBEDO (%)	NET BALANCE
87.75	181.0	181.0	181.2	86.0	-128.2
83.25	183.3	182.9	183.4	82.6	-122.2
78.75	185.7	184.8	185.5	76.1	-115.1
74.25	188.0	186.8	187.6	68.8	-105.6
69.75	191.4	190.2	191.1	63.2	-96.3
65.25	195.9	194.1	195.3	56.9	-85.6
60.75	200.7	199.0	200.1	50.4	-73.1
56.25	206.1	204.3	205.5	46.1	-60.4
51.75	212.4	209.4	211.2	43.0	-47.5
47.25	220.0	215.7	218.2	40.0	-34.4
42.75	228.6	222.7	226.0	37.0	-21.1
38.25	237.8	230.6	234.5	34.1	-8.7
33.75	247.3	239.0	243.5	31.4	2.3
29.25	256.3	247.3	252.1	29.0	12.3
24.75	262.6	253.6	258.5	26.8	23.2
20.25	264.6	256.1	260.7	25.0	35.8
15.75	261.7	254.2	258.3	24.0	49.2
11.25	255.7	249.2	252.8	23.9	60.4
6.75	250.6	244.7	248.0	24.2	67.6
2.25	250.1	244.1	247.4	23.9	71.2
-2.25	253.1	246.3	250.0	23.4	70.8
-6.75	257.3	249.9	254.0	23.0	66.6
-11.25	262.4	254.3	258.7	22.7	59.6
-15.75	266.6	257.5	262.4	22.6	51.0
-20.25	267.5	258.1	263.2	23.1	41.8
-24.75	264.1	255.4	260.1	24.1	32.9
-29.25	256.7	250.1	253.8	25.7	23.8
-33.75	247.1	243.2	245.5	27.9	13.5
-38.25	236.8	235.5	236.4	30.7	1.0
-42.75	226.8	226.9	227.2	34.1	-13.2
-47.25	217.7	218.7	218.5	37.5	-28.2
-51.75	209.5	211.4	210.8	41.2	-43.6
-56.25	202.0	203.8	203.2	45.4	-58.9
-60.75	194.3	195.9	195.4	51.7	-74.6
-65.25	185.4	186.8	186.4	60.5	-89.7
-69.75	174.8	176.6	175.9	68.3	-100.6
-74.25	164.6	164.9	165.0	72.3	-104.1
-78.75	156.0	155.5	156.0	78.4	-102.1
-83.25	147.4	146.1	147.0	84.4	-98.1
-87.75	138.9	136.7	138.0	87.1	-93.4

Table 3.3: *Nimbus-7* Earth Radiation Budget zonal averages for the eight year data set (November 1978 - October 1986). Values are Wm^{-2} . Transport scaled by 10^{15} .

LATITUDE	DIURNAL DIFFERENCE	TOTAL TRANSPORT
87.75	0.0	0.1
83.25	0.4	0.4
78.75	0.8	0.8
74.25	1.2	1.4
69.75	1.1	2.1
65.25	1.7	2.8
60.75	1.7	3.6
56.25	1.8	4.3
51.75	3.0	4.9
47.25	4.3	5.4
42.75	5.9	5.8
38.25	7.1	6.0
33.75	8.3	6.0
29.25	9.0	5.9
24.75	9.1	5.5
20.25	8.5	4.9
15.75	7.5	4.1
11.25	6.5	3.0
6.75	5.8	1.8
2.25	6.0	0.5
-2.25	6.8	-0.8
-6.75	7.5	-2.1
-11.25	8.0	-3.1
-15.75	9.0	-4.0
-20.25	9.4	-4.7
-24.75	8.7	-5.2
-29.25	6.6	-5.5
-33.75	3.9	-5.6
-38.25	1.3	-5.6
-42.75	-0.1	-5.3
-47.25	-1.0	-4.9
-51.75	-1.9	-4.3
-56.25	-1.8	-3.6
-60.75	-1.6	-2.8
-65.25	-1.4	-2.0
-69.75	-1.8	-1.3
-74.25	-0.4	-0.7
-78.75	0.5	-0.3
-83.25	1.3	0.1
-87.75	2.1	0.0

Table 3.4: *Nimbus-7* Earth Radiation Budget GLOBAL monthly averages for the eight year data set from 11/78 – 10/84. Values are Wm^{-2} , except Albedo in %.

MONTH	IRF DAY	IRF NIGHT	IRF AVE	ALBEDO	NET BALANCE
January	235.4	230.1	233.1	30.6	12.3
February	235.7	230.2	233.3	30.0	12.7
March	234.9	230.3	232.9	29.8	10.1
April	236.1	230.7	233.7	29.9	5.0
May	237.9	232.7	235.6	30.0	-2.4
June	239.4	234.9	237.5	30.0	-6.5
July	240.4	235.9	238.4	29.7	-5.2
August	241.7	236.2	239.3	28.9	-1.4
September	239.0	234.7	237.1	28.9	4.0
October	237.0	232.2	235.1	29.9	6.7
November	236.3	230.5	233.7	31.1	7.7
December	234.0	229.6	232.1	31.1	10.7

3.2 Monthly Averages and Annual Cycles

This section will present the monthly averages and will discuss the magnitude of the annual cycles. As mentioned earlier only two months in the first eight years were missing, May and June 1986. Therefore averages for these months May and June included only seven years while the other months included eight. The global averages for each month are listed in Table 3.4. Hemispheric averages for the NH and SH appear in Tables 3.5 and 3.6.

3.2.1 Outgoing longwave radiation and net balance

The annual cycle of global averaged NET balance and OLR are presented in Figure 3.13. We can see that the NET balance and the OLR have a considerable annual cycle and the amplitude of the annual cycle is 19 and 8 Wm^{-2} respectively. We have found the NET cycle to almost identically reflect the incident radiation cycle, which again points out the stability of the OLR/albedo reciprocity radiative effect. Maximum NET occurs in January and February when the earth is closest to the sun. The minimum occurs six months later in June – July. Interannual variability on each monthly average is represented by the error bars which show plus and minus one standard deviation of the

Table 3.5: *Nimbus-7* Earth Radiation Budget NORTHERN HEMISPHERE monthly averages. Values are Wm^{-2} , except Albedo in %.

MONTH	IRF DAY	IRF NIGHT	IRF AVE	ALBEDO	NET BALANCE
January	230.0	224.7	227.7	29.2	-66.3
February	231.5	225.9	229.0	29.9	-37.3
March	232.9	227.7	230.6	30.8	1.7
April	237.1	229.9	233.8	31.5	37.6
May	241.4	233.8	238.0	30.0	62.6
June	245.0	237.8	241.7	30.0	72.0
July	247.3	241.0	244.5	31.2	66.6
August	247.2	240.8	244.3	30.0	44.6
September	242.5	238.0	240.5	29.2	10.9
October	237.7	233.1	235.7	29.1	-28.8
November	233.0	227.4	230.5	29.3	-61.8
December	229.0	224.3	226.9	28.7	-75.3

Table 3.6: *Nimbus-7* Earth Radiation Budget SOUTHERN HEMISPHERE monthly averages. Values are Wm^{-2} , except Albedo in %.

MONTH	IRF DAY	IRF NIGHT	IRF AVE	ALBEDO	NET BALANCE
January	240.8	235.4	238.5	31.3	91.0
February	239.9	234.4	237.5	30.0	62.6
March	236.8	232.9	235.2	28.9	18.6
April	235.2	231.6	233.7	27.7	-27.7
May	234.4	231.5	233.3	30.0	-67.5
June	233.3	233.9	233.3	30.0	-85.0
July	233.4	230.8	232.4	26.6	-77.0
August	236.1	231.7	234.2	27.1	-47.4
September	235.5	231.3	233.7	28.6	-2.9
October	236.8	231.4	234.4	30.6	42.1
November	239.1	235.0	237.3	32.2	96.7
December	239.6	233.6	236.9	32.1	77.2

monthly average from the 8 year mean. Highest variability occurs during April and May with considerably less variation during June – October. The variability of the monthly NET was generally 1.0 to 1.5 Wm^{-2} , and we again note as stated earlier, that the NET cycle is not centered on 0.0 Wm^{-2} , but skewed to a positive 4.5 Wm^{-2} .

The three OLR annual cycles plotted in Figure 3.13 are from the ascending orbits (day), the descending orbits (night), and the daily average. An interesting result is that the global diurnal difference of the OLR (the difference in the ascending and descending passes) changes little throughout the year, and varies by only 1 Wm^{-2} . The diurnal difference stays fairly constant in the spring and fall seasons but increases in the summer and winter, probably due to the larger day/night temperature differences over the continents during these months. The longwave emission peaks in August during the northern hemisphere (NH) summer, with the minimum in January. Individual hemispheric averages show a slightly greater intra-annual variability of $3\text{--}4 \text{ Wm}^{-2}$, and a slightly greater day-night difference occurs during the hemispheres summer. Plus or minus one standard deviation of the monthly averages is plotted as error bars on the annual cycle of the daily average. The NH summer months (May–August) have the largest monthly variation with almost twice the variability in May as during the minimum in December.

3.2.2 Albedo

The annual albedo cycle is also presented in Figure 3.13 and is quite different than the NET or the OLR as more than just a single wave cycle was evident, with a secondary maximum in May – June. The causes of this effect were examined in Randel and Vonder Haar (1985). The reason behind the increase from March through May was not discernable by examining either the global or hemispheric average albedo cycles. The annual cycle of smaller areas needed to be examined to find the areas where the albedo was increasing during these months. Therefore each hemisphere was split into two equal latitude areas from $0\text{--}30^\circ$ and from $30\text{--}90^\circ$. The annual cycle of these 4 areas are shown in Figure 3.14. The reflectivity of the north and south polar quadrants were decreasing during these months and therefore these areas could not contribute to the global average increase. However from 30°N to 30°S the albedo was increasing and thus it is the tropics which drive

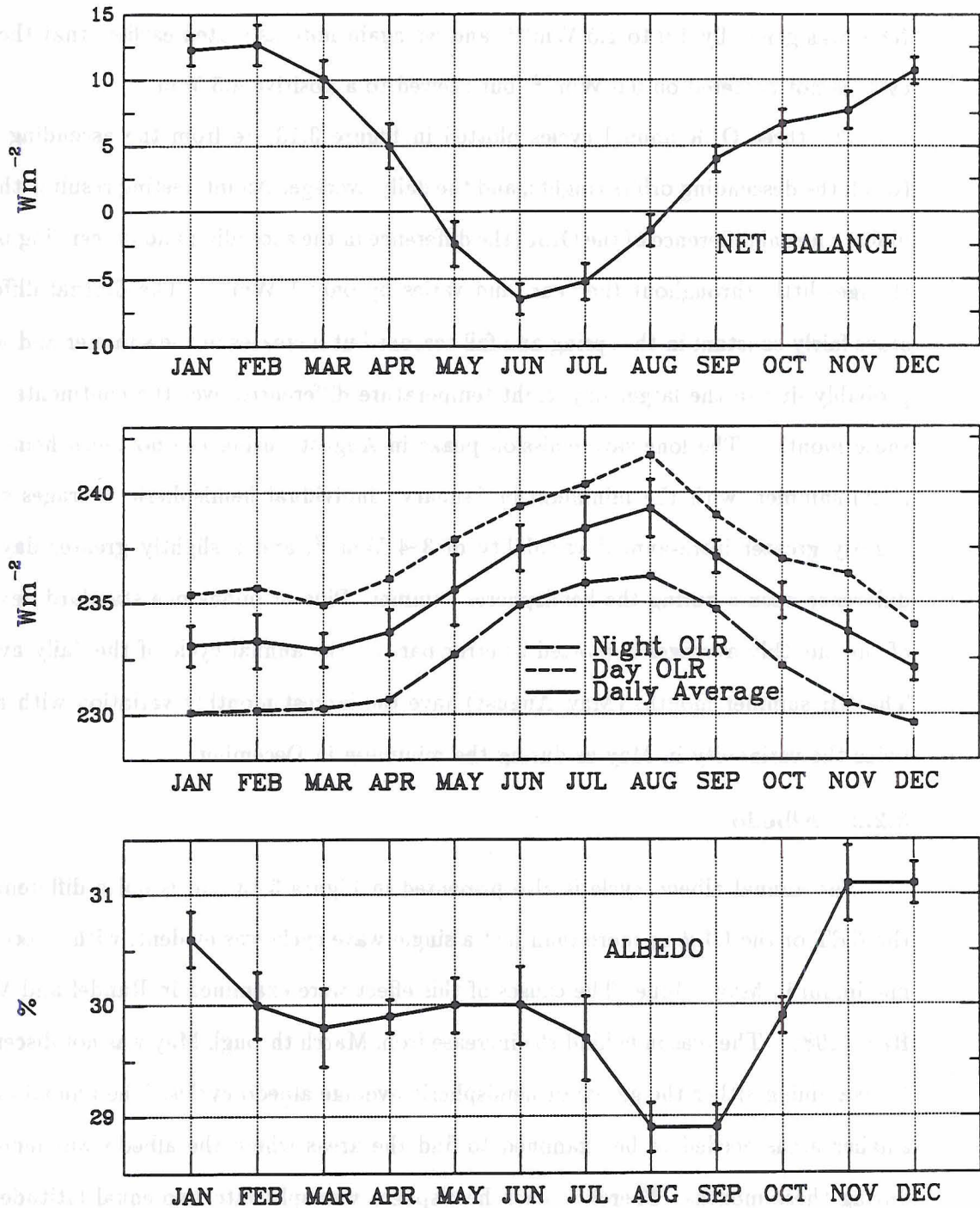


Figure 3.13: Annual cycle of global averaged NET balance, OLR and albedo for the eight years 11/78 - 10/86. Values are Wm^{-2} except albedo which is in $\% \times 100$.

the secondary albedo maximum. Next the annual cycle of individual years was examined and revealed that during half the years the albedo dropped from May to June and the other half it increased. We assumed that some large scale global effect was occurring to change this albedo pattern. Since global averages were being examined, regional scale influences would need to be large to have any effect on the global average. We knew from examining the albedo cycle by latitude quadrant that the tropics were the most likely area for year to year variability. Of course the Indian monsoon was suspected first as it causes a large regional scale increase in the albedo and it usually commences during June.

Examination of the tropical radiation budget components in the Indian monsoon region proved this area to be the major contributor to the global increase in albedo. For three years (1980, 1982, 1985) the global albedo increased from May to June. These years were characterized by a large May - June difference in albedo over northern India. Alternatively for 2 years (1979,1981) the global averaged decreased and the May - June albedo decreased over southern India and the eastern Arabian Sea. These large changes in albedo (15 %) were associated directly with the changes in convective cloudiness and the onset of the Indian monsoon. Changes in the timing or location of the convective activity near the beginning or end of the month can cause this interannual variability in the June monthly averages. It is remarkable that year to year changes to a regional area can significantly affect the globally averaged radiation budget values.

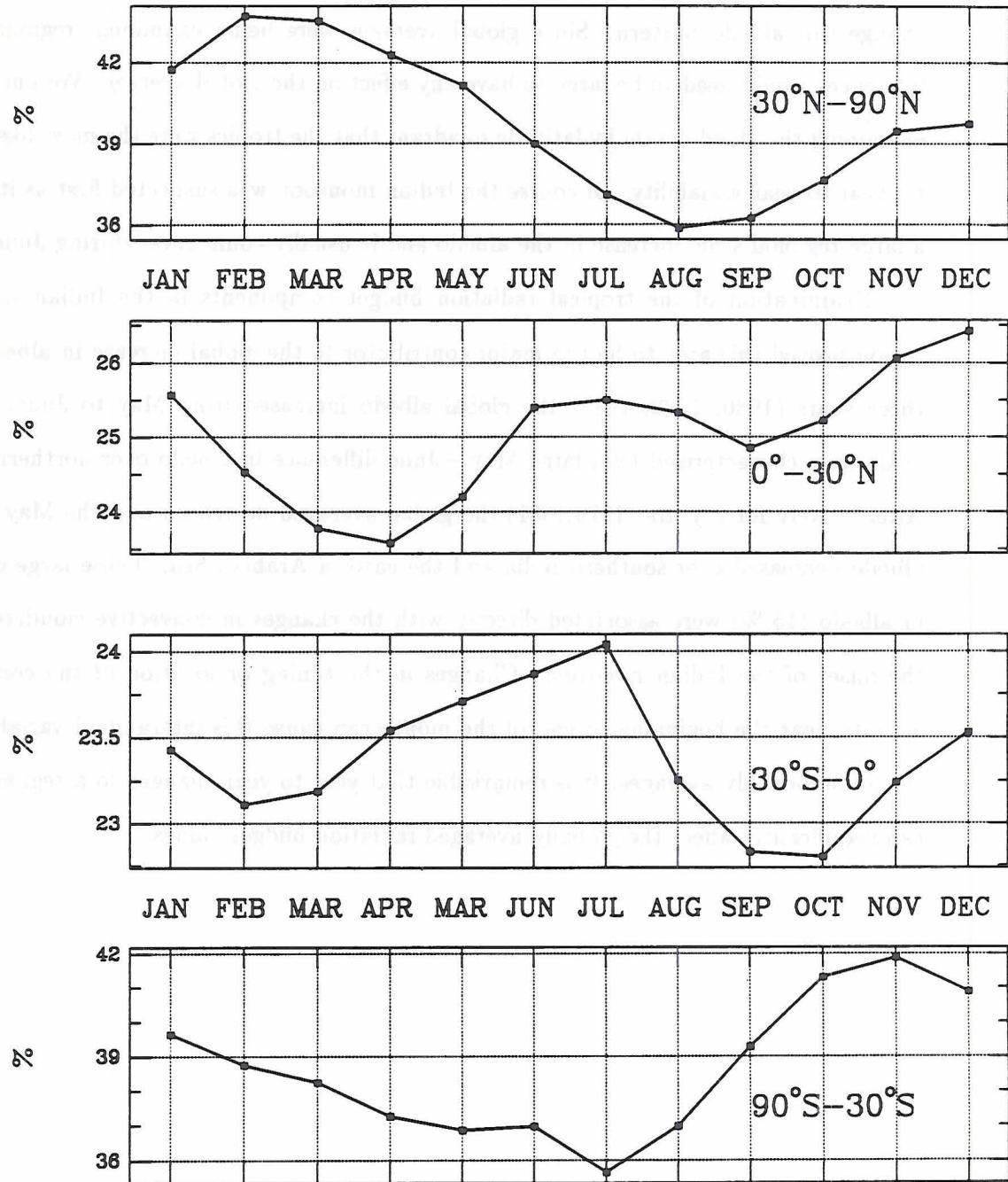


Figure 3.14: Annual cycle of sub-hemispheric averaged albedo (%).

Chapter 4

VARIABILITY IN THE EARTH RADIATION BUDGET

This chapter will examine the variation of the ERB from *Nimbus-7* over the first 8 years of the data ERB set. An easy approach to studying interannual variability is by calculating the variance between the samples. This is done in the following three subsections. The first uses annual averages as the samples, the second calculates the monthly variance before an annual average is computed, and the third includes the annual cycle by treating each month as a sample in the variance calculation. Each of these methods will be described in the individual subsections and the results reveal areas which vary the most in the ERB but due to different factors. The final section will examine in detail, using the CMATRIX cloud products the areas of highest NET variability.

4.1 Interannual Variability

4.1.1 ERB Variability of One Year Averages

A major advantage of the long ERB data set is that it is possible to examine the interannual variations using annual averages rather than just a collection of months. This enables us to look at how a longer term average 'climate' can differ from one year to another. To examine the variability of the annual averages, seven annual averages as well as their mean were calculated from which standard deviations were computed. This removes the annual cycle and highlights those areas in which the ERB anomalies last many months.

The *Nimbus-7* ERB data set had one large data inconsistency when the instrument was prematurely turned off, affecting May and June 1986. The solar power cells on *Nimbus-7* degraded with exposure to space, and over time this decreased the available

Table 4.1: *Nimbus-7* Earth Radiation Budget global averages of STANDARD DEVIATION OF ONE YEAR AVERAGES for 11/1978 - 10/1985. Values are in Wm^{-2} except albedo which is in %.

Parameter	Global Ave	Global Max	Global Min	NH Ave	NH Max	NH Min	SH Ave	SH Max	SH Min
OLR DAY	3.0	12.5	0.4	3.4	12.5	0.5	2.7	11.9	0.4
OLR NIGHT	3.0	11.0	0.4	3.1	10.6	0.5	2.9	11.0	0.4
OLR AVE	2.9	11.0	0.2	3.1	10.9	0.2	2.7	11.0	0.4
ALBEDO	0.9	3.3	0.1	1.0	3.3	0.1	0.9	3.0	0.2
NET	2.4	6.2	0.4	2.3	5.7	0.4	2.7	6.2	0.5

power to the satellites instruments. The ERB instruments were shut down due to the power limitations for two months during 1986 when two instruments on board *Nimbus*, the SMMR and CZCS were given power priority. After this time the CZCS instrument failed and power to the ERB was restored. Since two months of data were missing from the eighth year, data from this year could not be included when the means, standard deviations, and anomalies were generated. Of course this precluded any eighth year annual anomalies from being generated. Again it must be mentioned that the entire data set was very well calibrated, and while the absolute error in the measurements approaches 7 Wm^{-2} , we believe the relative error from one year to the next to be minimal.

The global average standard deviations for the ERB parameters with the annual cycle removed are listed in Table 4.1 and were: outgoing longwave radiation (OLR) and NET, 3.0 Wm^{-2} , and albedo less than 1 %. The greatest variability in the OLR had a standard deviation of 11.0 Wm^{-2} , 6.2 Wm^{-2} for the NET, and 3.3 % for the highest albedo variation. The local noon and midnight OLR maximums are 12.5 Wm^{-2} and 11.0 Wm^{-2} respectively. There are only small hemispheric differences, and generally no hemispheric bias in the global averaged values seems to occur. Thus at least on annual averaged time scales, with hemispheric averages, the variation of the radiation budget in each hemisphere is equivalent.

Figures 4.1, 4.2, and 4.3 present the global maps of standard deviation for the OLR, albedo and NET balance. We see from the albedo map that high variations occur in the

polar regions, mainly due to wide fluctuations in snow and ice coverage. The OLR map also shows higher standard deviations over 4.0 Wm^{-2} poleward of 75° . The standard deviation of the NET reflects the OLR variability and also shows higher polar values. For most studies the high variations at the poles are not as important as the temperate latitudes areas because of the much smaller total energy exchange. The map projection used here makes these polar areas seem much larger in proportion to the equatorial areas than they actually are. The interannual variation in the mid-latitudes is remarkably small with minimum OLR and albedo values below 2 Wm^{-2} and 0.5 % respectively over the oceans. Only slightly higher mid-latitude variation occurs over the continents. The standard deviation of the ERB parameters is greatest in the tropics, where small Wm^{-2} changes can have profound effects on the energy budget. These high variability areas have the largest amounts of incoming and outgoing radiation, and due to the number of square meters, the total energy changes are extremely large. The standard deviation of OLR and albedo are greatest in two areas of the central Pacific and co-located. Most of these tropical variations are due to the changes in cloudiness associated with the '82-'83 El Niño, with the exception of the large interannual variability in the NET west of tropical Africa. These NET anomalies will be examined in more detail in a later section. Even in the areas where the OLR and the albedo varied greatly, we see the effects of their reciprocity as a decreased variation in the NET, generally with values less than 3 Wm^{-2} . Greater interannual variations occur in three areas along the equator: South America and the eastern Pacific, the Gulf of Guinea off the west coast of Africa, and in the western Pacific northeast of the marine continent of Indonesia. We see from this set of figures that tropical interannual variability is not constant but changes greatly along the equator. This produces large gradients of varying energies that fuel the strong tropical circulations.

4.1.2 ERB Variability of Monthly Averages

In the previous section we calculated the annual averages of the ERB quantities for each of the seven full years in our data set, after which the mean and standard deviations were calculated. This effectively removed any variability with a short life cycle. In this section, the standard deviation of each month is first computed using the same month in

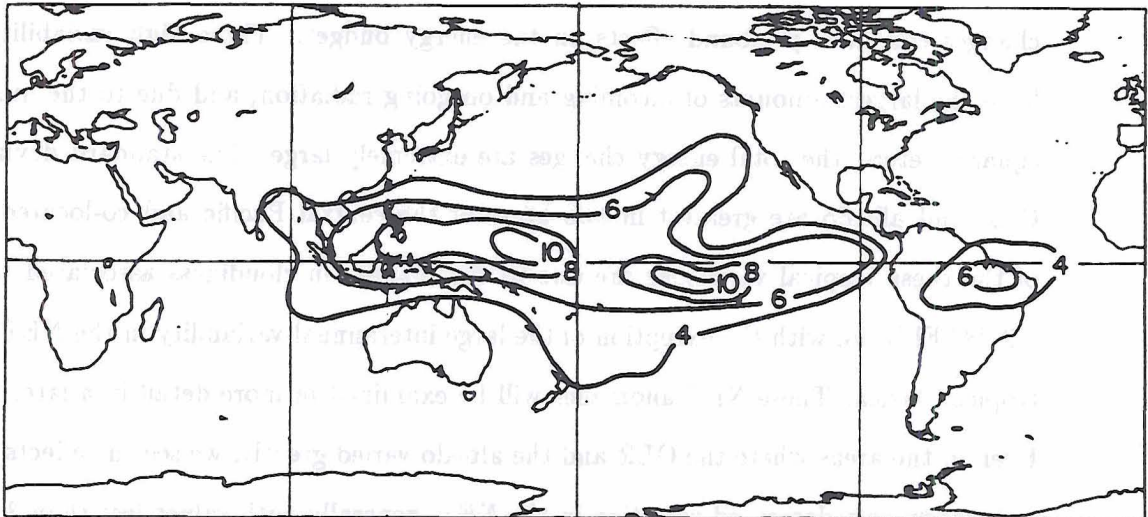


Figure 4.1: Standard deviation (Wm^{-2}) of the annual averaged outgoing longwave radiation from *Nimbus-7* for 11/79 - 10/85.

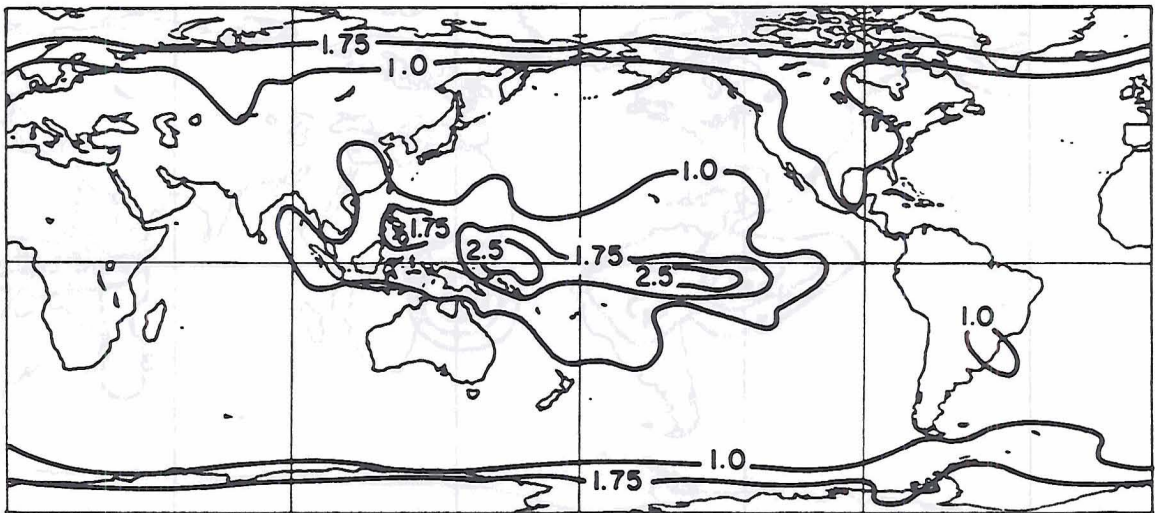


Figure 4.2: Standard deviation (%) of the annual averaged albedo from *Nimbus-7* for 11/79 - 10/85.

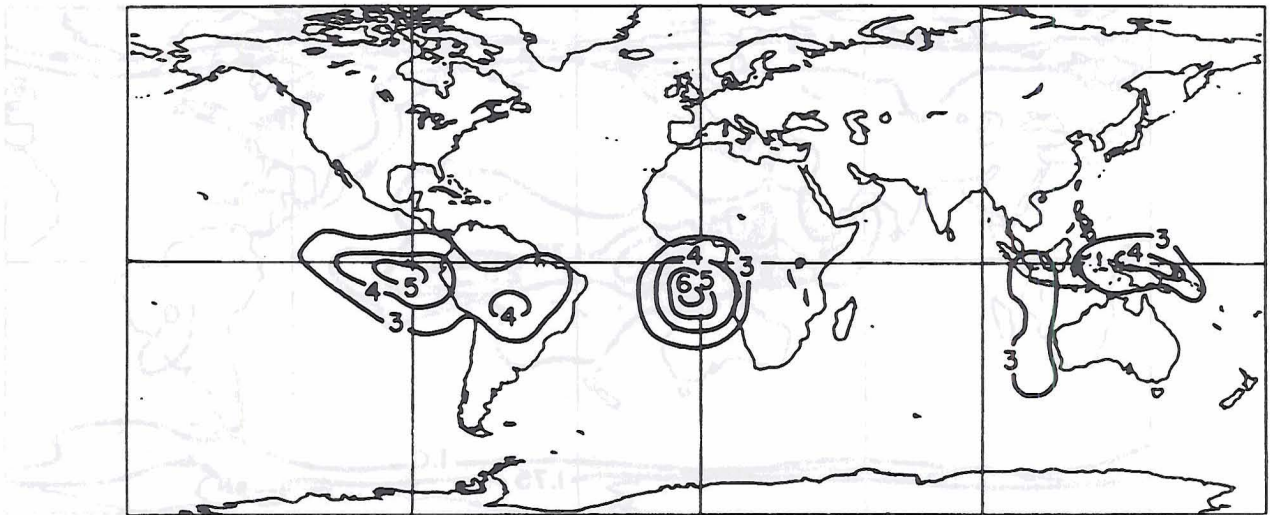


Figure 4.3: Standard deviation (Wm^{-2}) of the annual averaged net radiation balance from *Nimbus-7* for 11/79 - 10/85.

Table 4.2: *Nimbus-7* Earth Radiation Budget global averages of STANDARD DEVIATION WITH MONTHLY TIME SCALE included over the eight year data set (November 1978 - October 1986). All values are in Wm^{-2} except albedo which is in %.

Parameter	Global Ave	Global Max	Global Min	NH Ave	NH Max	NH Min	SH Ave	SH Max	SH Min
OLR DAY	6.7	18.7	2.1	7.2	18.7	3.1	6.2	17.4	2.1
OLR NIGHT	6.8	15.2	2.9	7.1	15.2	3.5	6.4	14.2	2.9
OLR AVE	6.1	15.0	2.1	6.5	15.0	3.1	5.7	13.9	2.1
ALBEDO	3.0	25.4	0.6	3.1	25.4	0.6	2.9	24.2	1.1
NET	5.7	10.5	3.2	5.7	10.3	3.2	5.7	10.5	3.4

each year as the sample. For example, the January deviation is calculated by using the eight Januarys as the sample, then the February deviation map is calculated using the eight Februarys, and so forth. Finally, these 12 global fields of monthly standard deviation are averaged to produce an annual averaged standard deviation. This in effect removes the annual cycle but shows the areas which have the highest variability including the shorter lasting events.

Dealing with the monthly averages has the added advantage of including year eight which had 2 missing months of data. The global averaged standard deviations of the ERB parameters including shorter time variability events are listed in Table 4.2.

The next 3 figures, 4.4, 4.5, and 4.6 present the global maps of standard deviation for the OLR, albedo and NET balance on the monthly time scale. The deviations are much greater than the previous set. The albedo map shows the lowest deviation in the Sahara desert and in the mid-latitude oceans of the SH. Very high deviations occur at each pole. Small interannual changes in the latitude of snow and ice coverage in the winter months have a severe influence on the albedo and OLR. A strong tropical maximum is evident along the equator at approximately $145^{\circ} - 160^{\circ}$ east longitude, northeast of the island of New Guinea. Other local maximums occur in the stratiform region off southern California, and a rather strong maximum over the central plains of the US and southern Canada. This area of higher albedo variability is not observed in the OLR standard deviation. Since this is a continental location, the effect most likely is caused by a surface property change

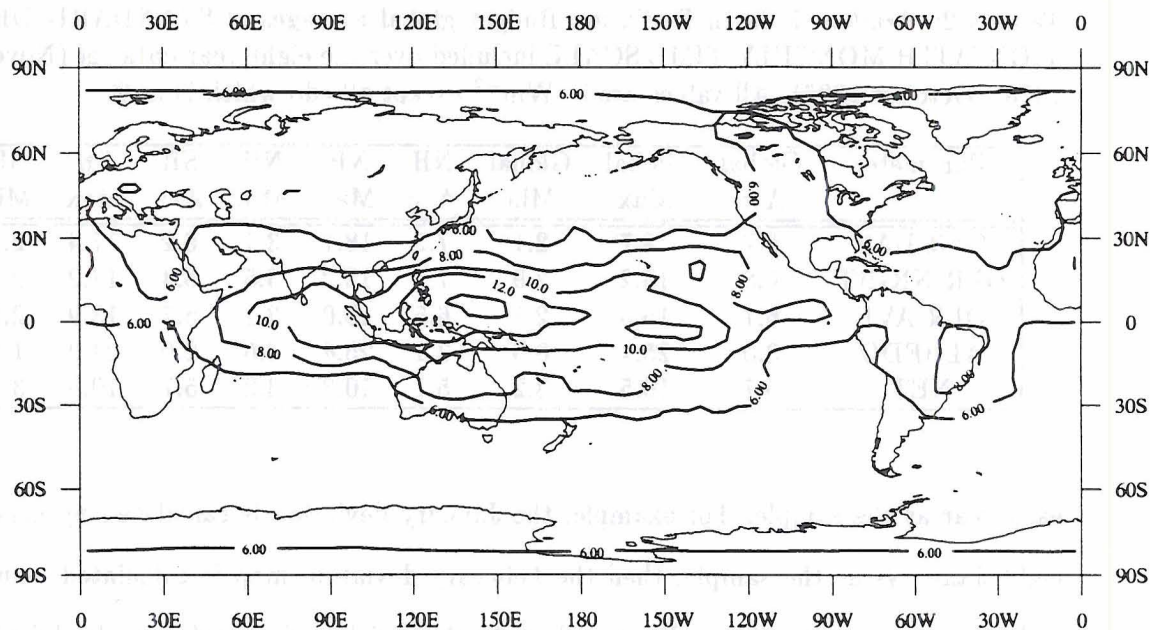


Figure 4.4: Standard deviation (Wm^{-2}) of the monthly averaged outgoing longwave radiation from *Nimbus-7* for 11/79 - 10/86. The standard deviations for each of the calendar months are then averaged into a yearly average, thus examining variability due to shorter time scales effects.

such as variability in the grass covered surface in summer or snow covered high albedo surface in winter. Figure 4.4, the OLR variation, shows the minimum variability over the SH ocean is less than 3 Wm^{-2} . The same latitude ocean areas in the NH has $3-4 \text{ Wm}^{-2}$ change. The maximum occurs near the equator but is over a much larger area than the area of maximum albedo variation. The OLR maximum is also centered well west of the albedo maximum between $120^\circ - 155^\circ \text{ E}$. longitude. In both these areas strong tropical convection occurs.

Other areas of high OLR variability include the central Sahara desert, and eastern Brazil. Patterns of high variation in the NET are similar to those using a one year average, but the stratiform region off the coast of California and the convective regions show greater fluctuations. The difference in the maximums for the Gulf of Guinea and the west coast of South America is even more pronounced than when the annual averaged were used.

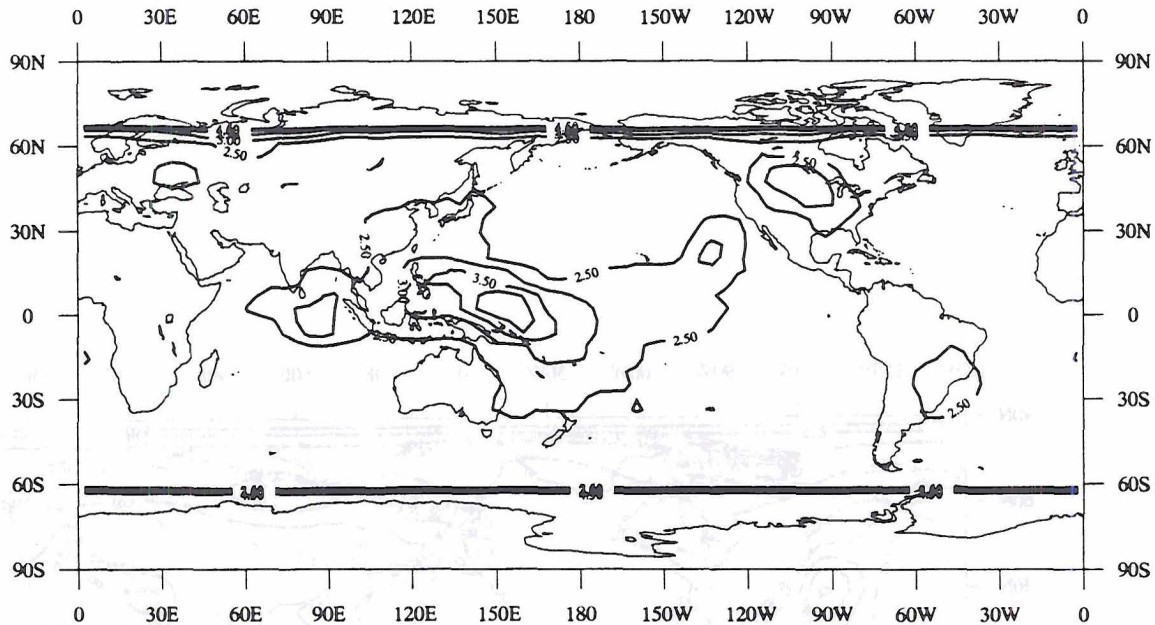


Figure 4.5: Standard deviation (%) of the annual averaged albedo from *Nimbus-7* for 11/79 - 10/86. The standard deviations for each of the calendar months are then averaged into a yearly average, thus examining variability due to shorter time scales effects.

4.1.3 ERB Variability with Annual Cycle

The next three figures examine the variability of the 94 month data set with the annual cycle included. The standard deviation sample included each individual month, and no averaging was done. In the albedo and NET parameters the annual cycle is much larger than with interannual only variability. Figure 4.7 shows the NET variability peaks at 90 Wm^{-2} in the southern mid-latitudes and 80 Wm^{-2} in the northern mid-latitudes. This is much greater than the $10\text{-}15 \text{ Wm}^{-2}$ with no annual cycle (shown in the previous figure set). The albedo plot with the annual cycle, Figure 4.8 shows this similar effect. The amplitude of the annual cycle in the high latitudes and over the mid-latitude continents is 4-5 times greater than the variability caused by interannual variability. This masks the greater interannual variability of the albedo in the Pacific as seen in Fig. 4.2. The OLR variability with the annual cycle is shown in Figure 4.9. The highest variability OLR areas are caused by continental heating and cooling, the movement of the ITCZ, and other large scale cloud changes such as the monsoons. The highest variability occurs in the areas

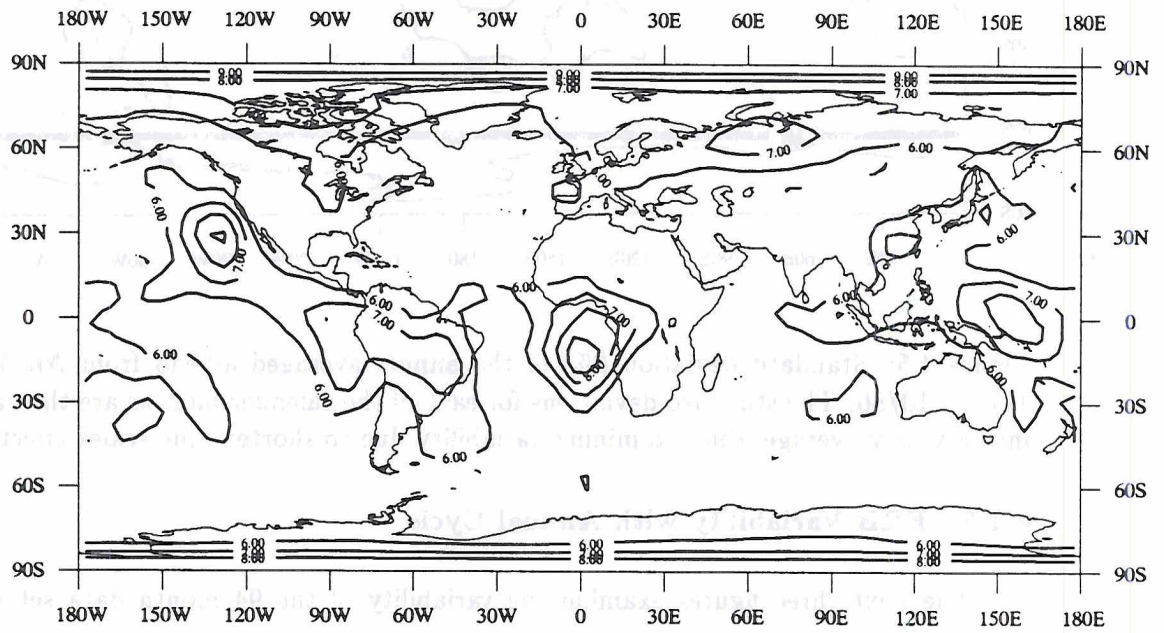


Figure 4.6: Standard deviation (Wm^{-2}) of the monthly averaged net radiation balance from *Nimbus-7* for 11/79 - 10/86. The standard deviations for each of the calendar months are then averaged into a yearly average, thus examining variability due to shorter time scales effects.

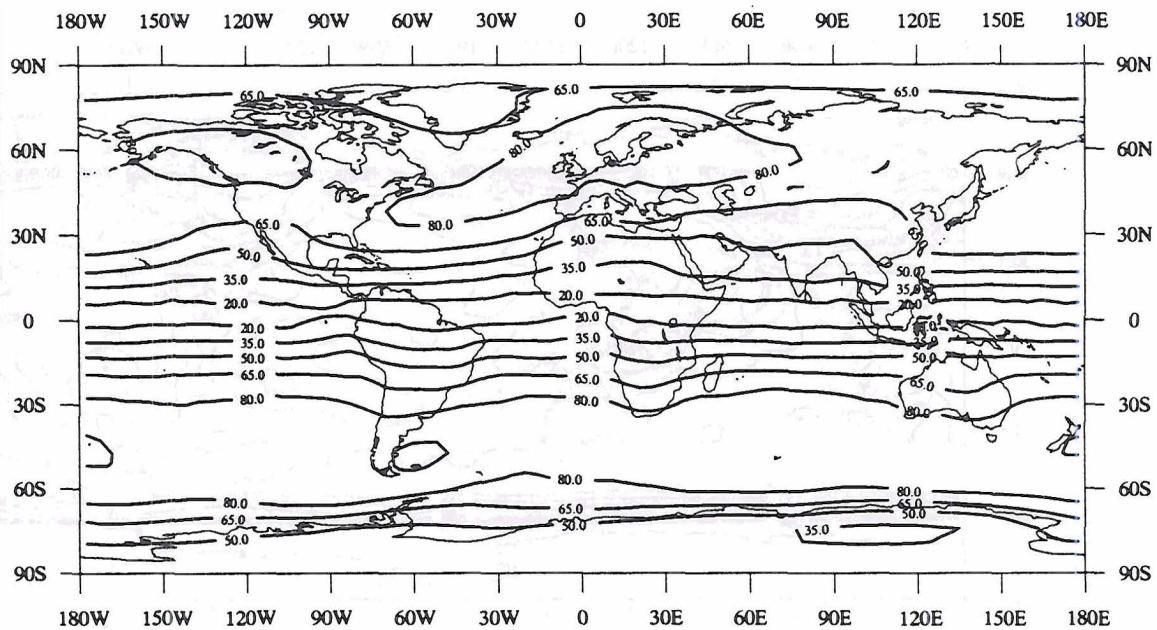


Figure 4.7: Standard deviation (Wm^{-2}) of the net radiation balance for 11/79 - 10/86 with all months as the sample thus including the annual cycle.

of western Asia, tropical Africa, the Bay of Bengal (caused by the Indian monsoon), the northern coast of Australia, and in tropical Brazil. The magnitude of the OLR variability is similar to that without the annual cycle (Fig. 4.1), but different areas are highlighted.

4.2 Examination of the Interannual NET Variability

This section will describe in detail the three areas of highest NET variability. What was most surprising was the variability of the Atlantic area which was 20% greater than the eastern Pacific and 35% greater than the western Pacific near Indonesia. The maximum anomalies in these two Pacific regions occurred during the El Niño year 1982 - 1983, while the maximum Atlantic anomalies, south of the Gulf of Guinea, occurred during 1984. An independent data set of derived cloud type and amount from the Temperature Humidity Infrared Radiometer (THIR) and the Total Ozone Mapping Spectrometer (TOMS) instruments shows interannual changes in multi-level convective cloud systems have a minimal effect of the NET. However changes in middle and low clouds drastically affect the balance, and are the most likely cause of the maximum radiation balance variability in the Gulf

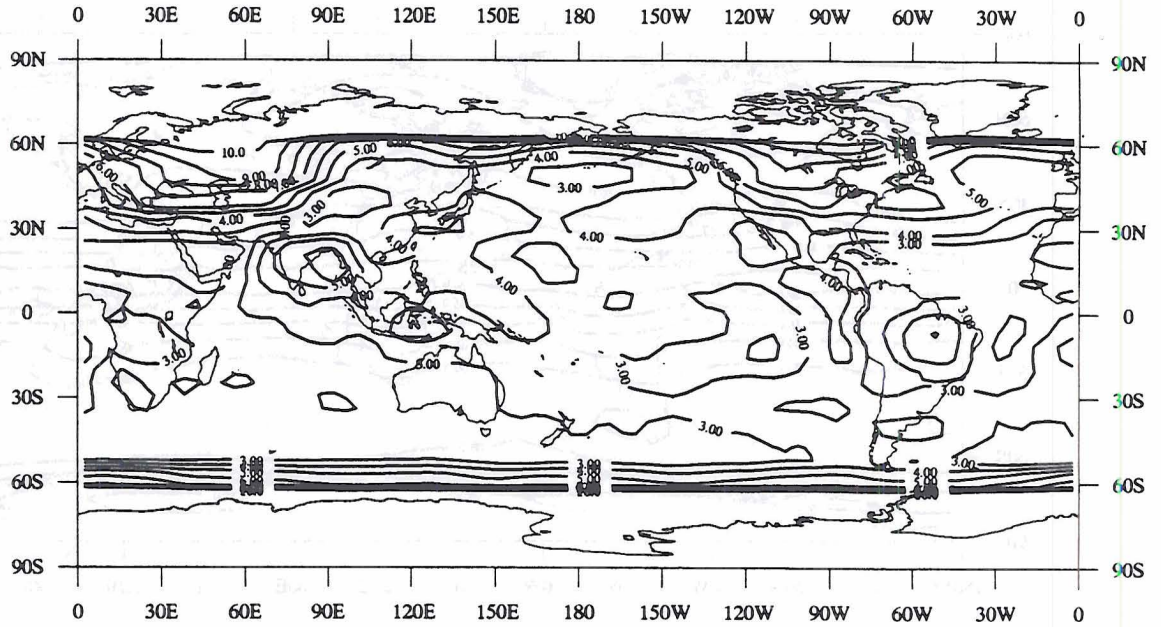


Figure 4.8: Standard deviation (%) of the albedo for 11/79 - 10/86 with all months as the sample thus including the annual cycle.

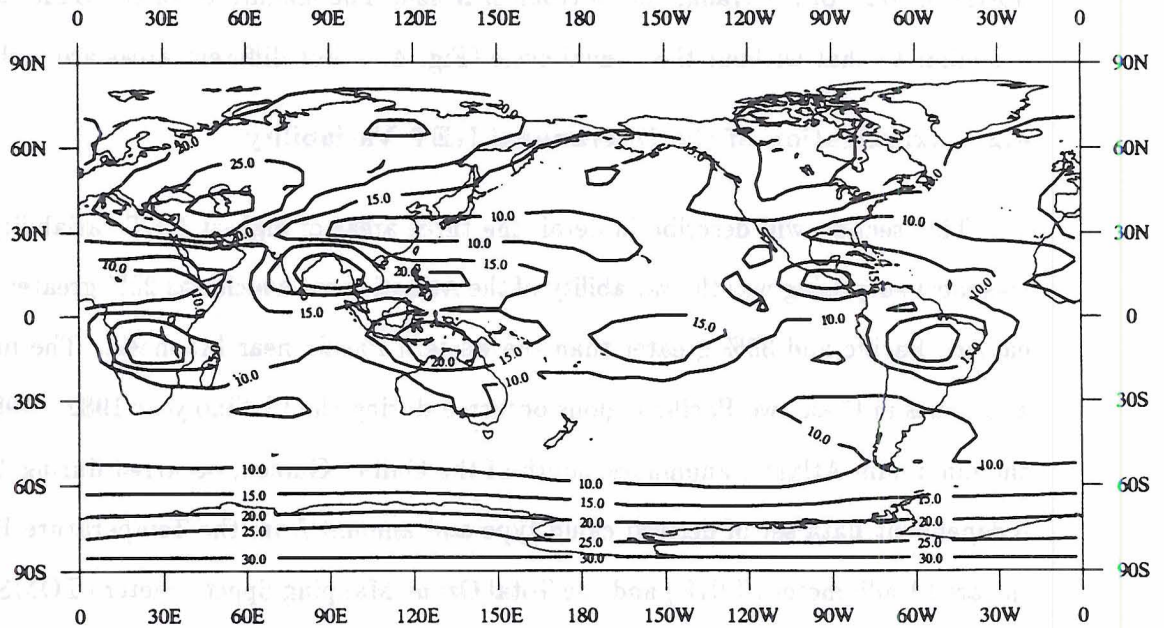


Figure 4.9: Standard deviation (Wm^{-2}) of the outgoing longwave radiation for 11/79 - 10/86 with all months as the sample, thus including the annual cycle.

of Guinea region. This observed interannual variation of the top of the atmosphere NET denotes the most variable "cloud radiative forcing" situation observed to date.

As has been discussed before, the NET is calculated by differencing the emitted long-wave and absorbed shortwave irradiances. This measurement defines deficit or surplus energy in the earth/atmosphere column that can be used in other energy transformations. The effect of clouds, referred to as cloud radiative forcing, is derived by differencing an actual scene with clouds and the defined clear sky irradiances. Cess (1976), Ellis (1978), Hartmann and Short (1980), and Ohring and Clapp (1980), have made estimates of the effect of cloud changes on the radiation balance and atmospheric temperature with sometimes conflicting results. Most recently Ramanathan et al. (1989) used early results from the Earth Radiation Budget Experiment (ERBE), and showed that clouds, in general, tend to cool the planet. The net radiative effect of course depends on the cloud type as well as total cloud amount. In general a change in large scale convective cloudiness results in little variation of the NET due to the reciprocity of the albedo and the emitted flux. When the cloud amount and albedo increase, the emitting temperature and flux decreases thus producing little NET change. However changes in certain cloud types do cause significant NET variation. An increase in low level stratiform clouds can greatly affect the balance by decreasing the absorbed shortwave radiation. Since they are near the earth's surface little change in emitted flux is observed. Another example is high level cirrus clouds which significantly affect the emitted flux but have a relative small albedo effect.

In addition to calculation of the radiative forcing it is important to identify areas where changes in cloudiness and forcing occur. The variability of these regions and their relative heating or cooling can modify the atmospheric energetics and have an effect on the general circulation. Studies, (Liebmann and Hartmann 1984; Hendon and Hartmann 1982; Hoskins and Karoly 1981) point to changes in the mid-latitude circulation patterns caused by tropical heat sources and sinks. Calculation of NET anomalies can help define these areas. The area off the west coast of Africa is shown to vary, in the annual average case, more than any other area in the world, and thus its effect as a changing tropical heat

source is of interest. An anomaly in the NET may also contribute to anomalies in sea surface temperature (SST), as there is often a positive NET anomaly in conjunction with large scale SST warming. Such highly variable regions are also of interest to circulation modelers as recent studies of the radiation budget with respect to model verification have shown the necessity of correctly modeling the large scale radiation variability as well as the overall patterns (Smith and Vonder Haar, 1989; Charlock et al., 1988; Ramanathan, 1987).

The interannual variability of the NET for this cloud-ERB comparison is shown in Fig. 4.3 and was calculated by first computing the seven annual averages and standard deviation using these samples. Each annual average follows the *Nimbus-7* satellite year from November 1 – October 31. As was stated previously the greatest NET variation occurs in the Gulf of Guinea area where the maximum standard deviation of 6.2 Wm^{-2} was greater than the 5.0 Wm^{-2} in the eastern Pacific, and 4.4 Wm^{-2} near Indonesia. Some regions poleward of 70° have similar variability, but due to the severe fluctuation of the albedo during times of near zero incident radiation, these areas are suspect.

4.2.1 NET Time Series

Examining the time series of the NET variability of the three areas, Figure 4.10, clearly shows the largest Pacific anomalies were during the El Niño in late 1982 into 1983. Near Indonesia the NET dropped rapidly after October '82, to an almost 25 Wm^{-2} decrease in February '83. After an initial rise of over 20 Wm^{-2} in late '82, the NET in the eastern Pacific near the coast of South America dropped 25 Wm^{-2} only to rise again later in the year. In the Gulf of Guinea region there was a decrease in the NET during '83 of 15 Wm^{-2} , but the largest anomalies of the eight year time period occurred during '84 – the year after the Pacific El Niño. Twice during '84, in January and September, the anomaly grew to over 20 Wm^{-2} , and at times during 1982 the anomalies were $10\text{-}20 \text{ Wm}^{-2}$ below normal.

Since our computation of the standard deviation involves annual averages, the interannual variation of the incident radiation is held constant, and therefore all the variation must be from the reflected and emitted irradiances. Figure 4.11 presents the time series

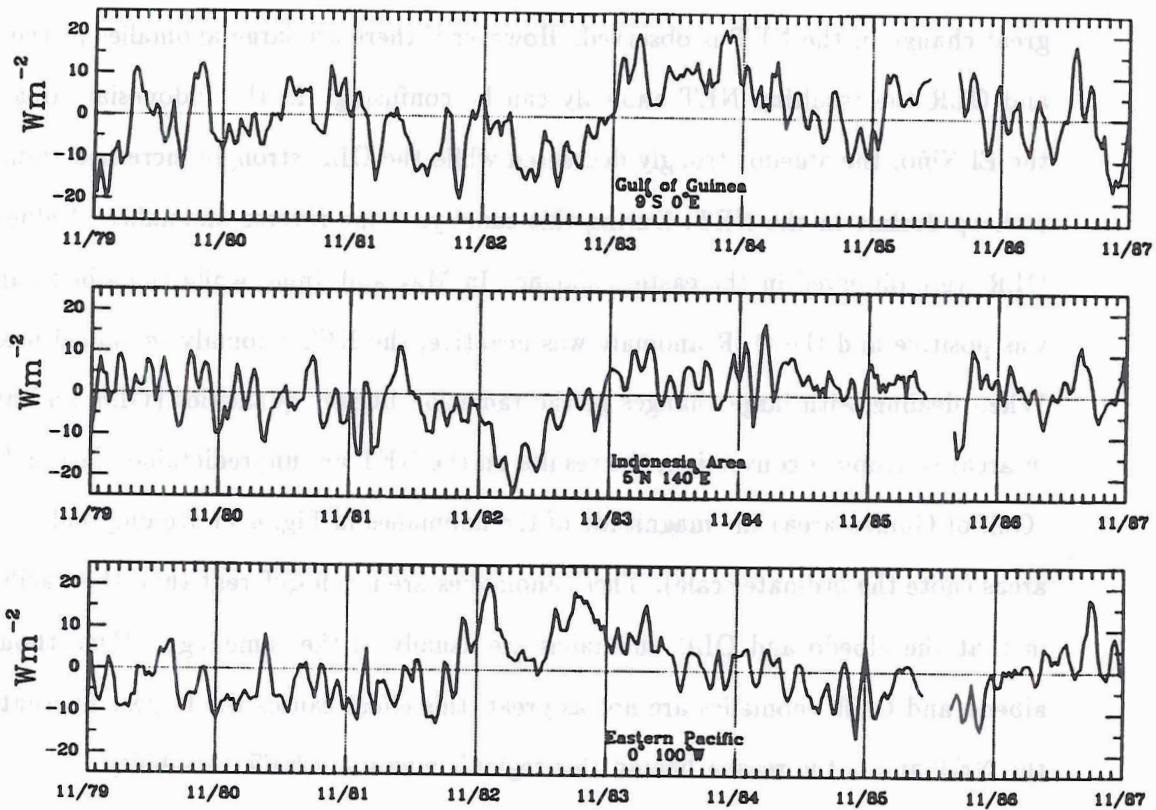


Figure 4.10: Weekly net radiation balance anomalies (Wm^{-2}) from *Nimbus-7* ERB for 11/1979 – 10/1986 in the three areas of highest annual averaged NET variability.

of the albedo and OLR anomalies concurrent with the NET anomalies of Fig. 4.10. Generally, for an individual time period, the albedo and the OLR anomalies are reversed. For example, when the albedo increases, (usually more cloud) the OLR will decrease due to the cooler temperatures of the cloud tops. This especially holds true in areas of strong convection, where whenever there is a positive anomaly in one parameter the other is negative. During times of low to moderate anomalies these two effects balance out and no great change in the NET is observed. However if there are large anomalies in the albedo and OLR the resulting NET anomaly can be confusing. In the Indonesian area during the El Niño, the albedo strongly decreased while the OLR strongly increased resulting in a sharp decline in the NET. During this same year the reverse anomalies of albedo and OLR were observed in the eastern Pacific. In May and June, while the albedo anomaly was positive and the OLR anomaly was negative, the NET anomaly remained near zero. When dealing with large changes in the radiation budget quantities (OLR and albedo), in areas of tropical convection, the results on the NET are unpredictable. In the Atlantic (Gulf of Guinea area) the magnitude of the anomalies in Fig. 4.11 are only half the other areas (note the ordinate scale). These anomalies are much different than the Pacific areas in that the albedo and OLR anomalies are usually of the same sign. Even though the albedo and OLR anomalies are not as great, this effect causes the largest fluctuations in the NET and is the reason behind this region's maximum NET variability.

The high variability of the ERB in the eastern and western Pacific is not unexpected as the El Niño during 1982 and 1983 has previously been shown to produce large changes in the OLR (Kyle et al., 1985). The Indonesian area is normally dominated by decreased OLR, indicative of strong vertically developed convection. This was reversed during early 1983. The eastern Pacific region generally has OLR values representative of little enhanced convection except during the El Niño year when this was the norm. Similar to the eastern Pacific, the OLR and albedo in the Atlantic area usually show no evidence of convective clouds. The Atlantic Intertropical Convergence Zone (ITCZ) and its associated strong convection rarely moves far enough south of the equator to have a direct effect on our

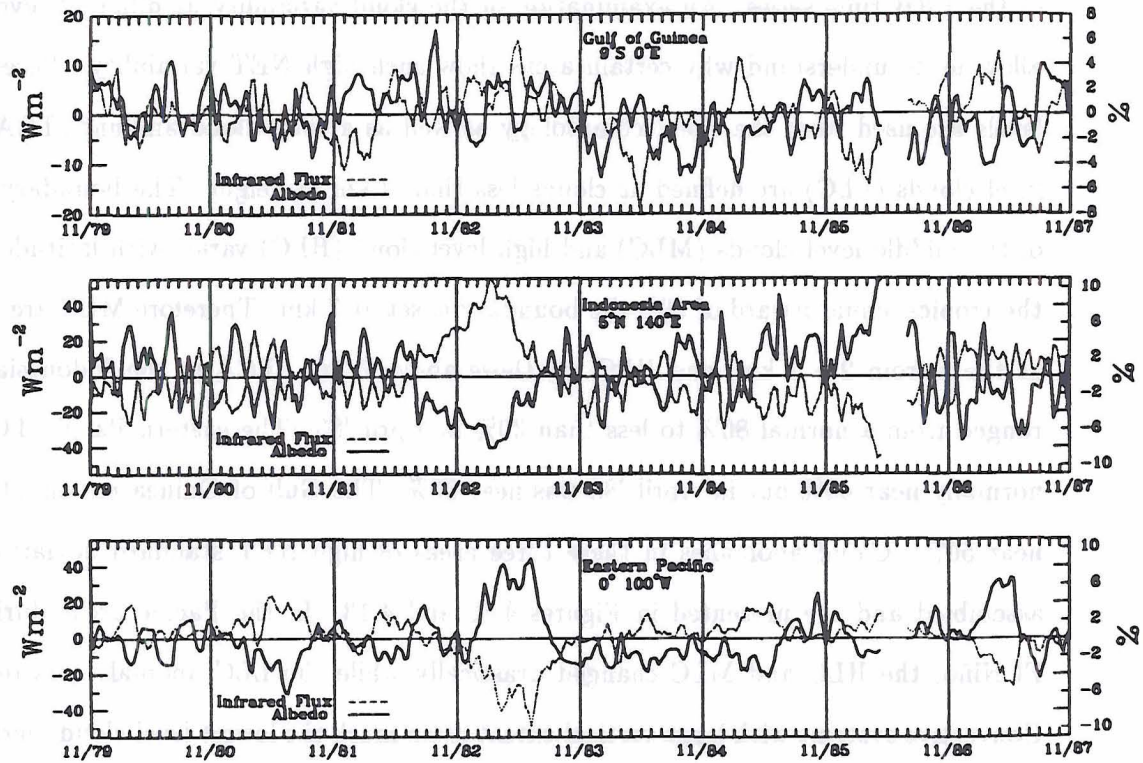


Figure 4.11: Weekly outgoing longwave radiation (OLR) anomalies (Wm^{-2}) and albedo anomalies (%) from the *Nimbus-7* ERB for 11/1979 – 10/1986 for the three areas of highest annual averaged NET variability.

defined region. Therefore the changes in clouds, which must be the cause of NET variability, are much different in each of the three areas. In the next section we will examine the cloud changes that lead to the radiation budget parameter anomalies.

4.2.2 Cloud Variability in Three Areas of Highest NET Variability

The *Nimbus-7* global cloud climatology is available for the first five and a half years of the ERB time series. An examination of the cloud variability at different levels, will allow us to understand why certain areas show such high NET variability. Three cloud levels are used from the cloud climatology as well as a total cloud amount (TCA). Low level clouds (LLC) are defined as clouds less than 2 km in height. The boundary height of the middle level clouds (MLC) and high level cloud (HLC) varies with latitude but in the tropics, equatorward of 30°, the boundary is set at 7 km. Therefore MLC are defined as those from 2 - 7 km, and HLC are those above 7 km. TCA in the Indonesian area ranged from a normal 80% to less than 30% in April '83. The eastern Pacific TCA was normally near 40% but in April '83 was near 90%. The Gulf of Guinea region TCA was near 50%. Cloud anomalies in these three areas of high NET standard deviation were assembled and are presented in Figures 4.12 and 4.13. In the Pacific areas during the El Niño, the HLC and MLC changed drastically while the LLC anomaly was reversed. Convective systems with large vertical extent often mask the lowest level cloud amount, so when the convective clouds are absent, an increase in the LLC anomaly becomes suspect. In contrast to large changes in the Pacific areas, the TCA in the Gulf of Guinea region varied by only 20%. The only significant changes were in the MLC (+/- 15%) and LLC (+/- 10%). During 1982 - '83 the TCA remained normal while there was an increase in the LLC and a decrease in the MLC. This increased the albedo and OLR and therefore dropped the NET. There was also a rise in the MLC during the following year, reaching a maximum anomaly of +10 % in April '84.

4.2.3 Discussion and Conclusions on Highest NET Variability Areas

It quickly became apparent that the three areas of greatest net radiation balance variability have quite different cloud characteristics. The two Pacific areas, one near

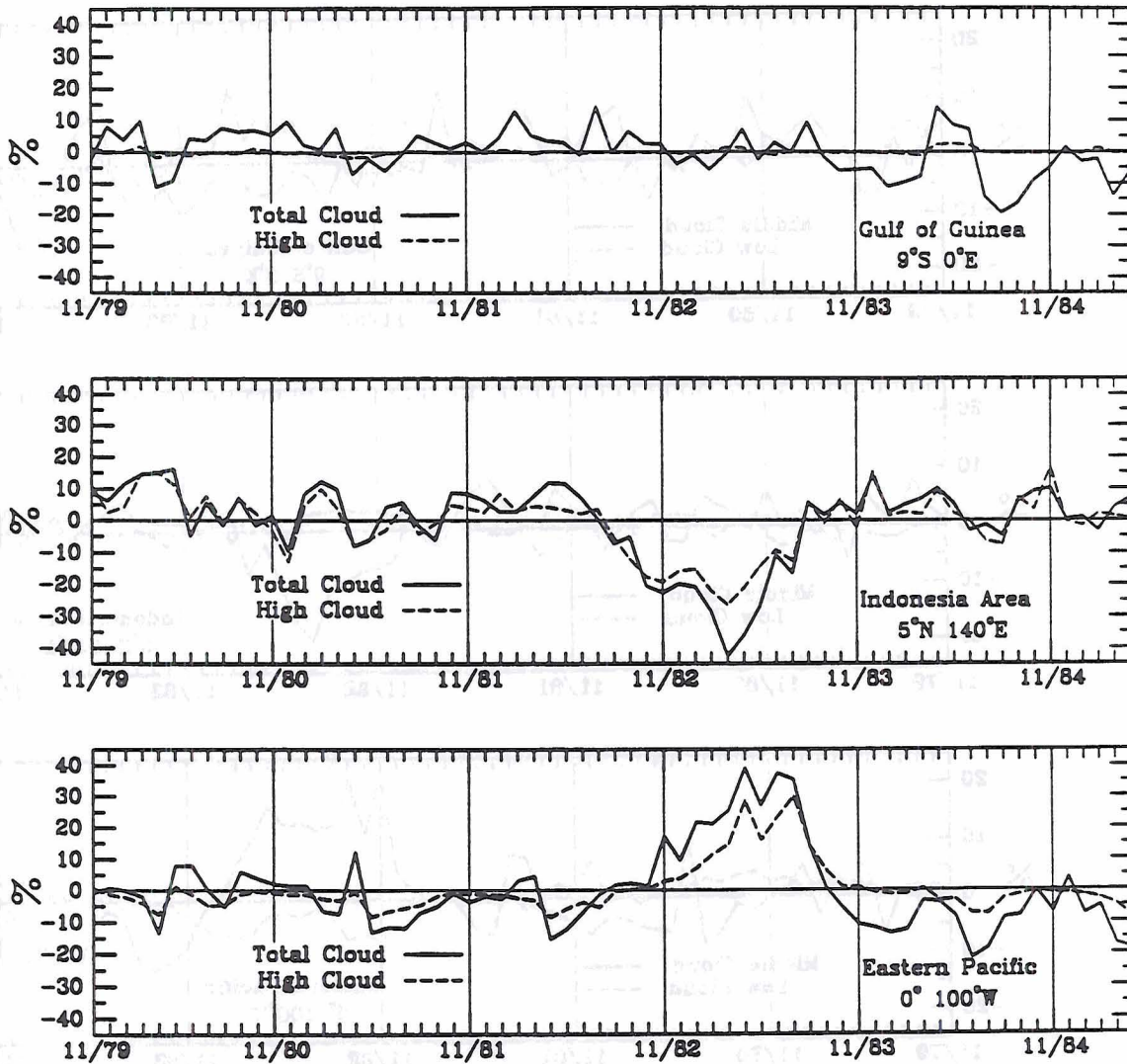


Figure 4.12: Total and High cloud amount anomalies (%) from the *Nimbus-7* cloud climatology for 11/1979 - 4/1985 for the three areas of highest annual averaged NET variability.

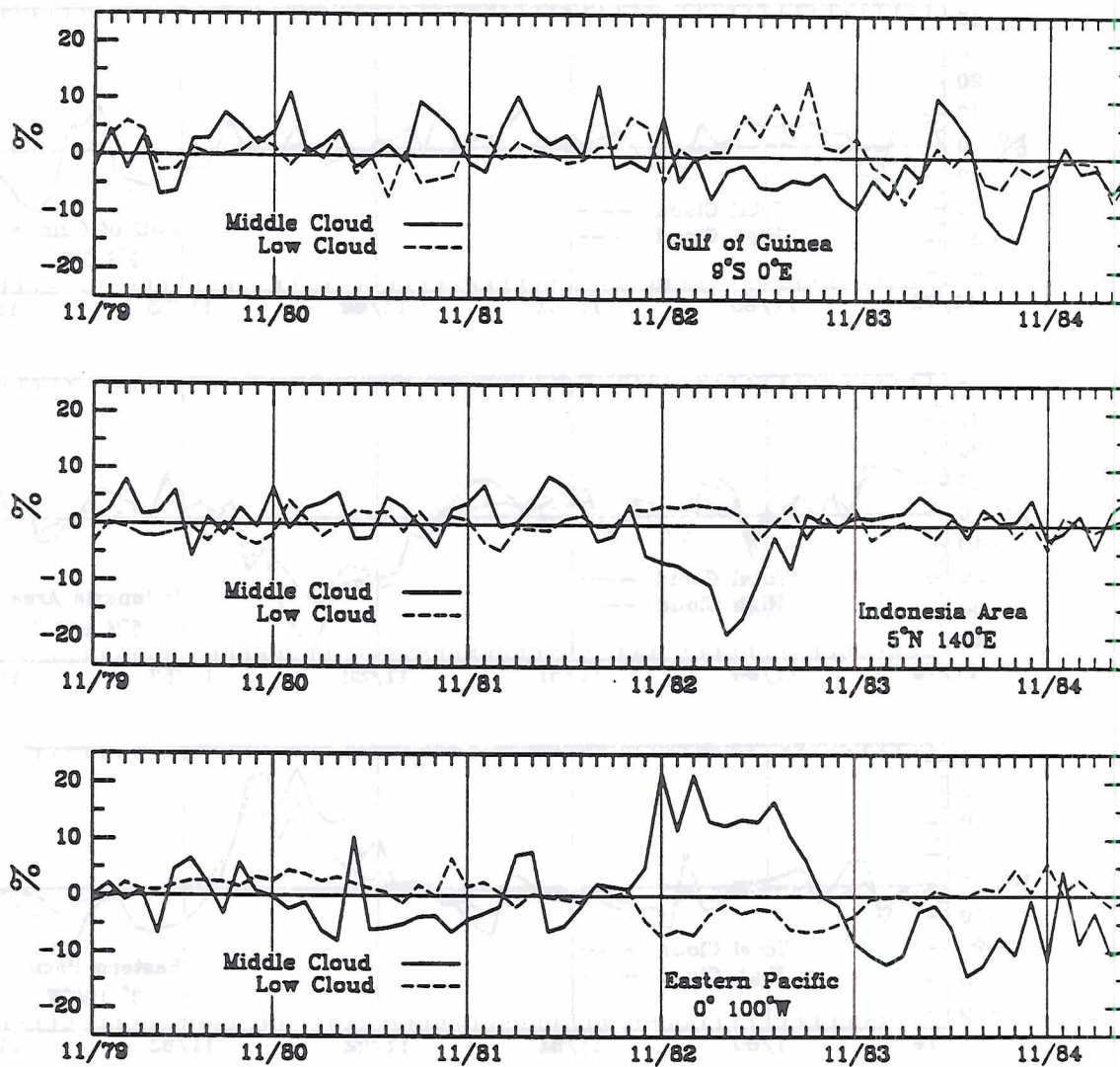


Figure 4.13: Middle and Low cloud amount anomalies (%) from the *Nimbus-7* cloud climatology for 11/1979 - 4/1985 for the three areas of highest annual averaged NET variability.

South America, the other near Indonesia were greatly influenced by cloud changes which occurred during the 1982-'83 El Niño event. The Indonesian area is normally 80% cloud filled, with low OLR and high albedo, and with considerable cloud amounts at all three levels. This area of strong convection has a interannual NET deviation of 4.4 Wm^{-2} with the largest variations during the El Niño year when a sharp decrease in the TCA, HLC and MLC occurred. At this time, the NET dropped sharply as anomalies in the emitted radiation were greater than those in the absorbed. Because this area still had significant cloud filled area the albedo did not change enough to offset the large increase in OLR caused by much warmer than normal emitting temperatures. The decrease in the HLC and MLC clouds were significant enough to allow the majority of emission to occur at lower levels.

The eastern Pacific region off the west coast of South America usually has near 40% TCA consisting of only MLC and LLC. By March 1983, the TCA had increased by over 40% with a sharp increase in the HLC and MLC. The albedo increased, the OLR decreased, but the NET anomaly was near 0.0 Wm^{-2} . The major enhanced convection was already occurring, as evident in the TCA increase, but the reciprocity of the albedo and OLR anomalies had cancelled any NET anomaly. The maximum NET anomalies were in December 1982 and August 1983 before and after the convective event. In these months the albedo and OLR anomalies were concurrently negative. This again points out the importance to the NET anomaly of relative minor changes in the OLR and albedo, when these are of the same sign. For the El Niño year this area had a positive NET anomaly of almost 10.0 Wm^{-2} , and was an area of warmer than average SST. This 'surplus' energy in the ocean-earth-atmosphere column may have contributed to the increase and maintenance of the high SST. The El Niño event provided the most significant contribution to this region's high NET variability, (5.0 Wm^{-2}), but the following year the NET was still above average. Other than these years the NET was remarkably constant.

The region which had the highest interannual variability of the NET, 6.2 Wm^{-2} , is off the west coast of Africa, south the Gulf of Guinea. Only MLC and LLC dominate this area's cloud climatology. As previously discussed, when these cloud amounts fluctuated,

the anomalies of albedo and OLR often had the same sign, thus causing the large changes in the NET. The NET variability was greatest in 1984, the year after the Pacific El Niño, when the anomalies of MLC and LLC were widely varying. An Atlantic SST warming event similar to the Pacific El Niño occurred in 1984 (Weisberg and Colin 1986). In June of that year the SST in our defined area was 3–4 °C warmer than the previous year. By this time there had been seven months of above normal NET, averaging near 10 Wm^{-2} . As in the Pacific this surplus energy may have contributed to the rise and maintenance of the SST anomaly.

An associated displacement of the Atlantic ITCZ southward from normal (Philander, 1986; Horel et al., 1986) may account for the cloud and NET variability observed during 1984. In January and August the NET anomaly was $+20 \text{ Wm}^{-2}$, caused by large negative albedo anomalies and minimal increases in OLR. A sharp decline in the MLC and LLC caused these radiation changes. The ITCZ is normally furthest north in August allowing the southern hemisphere subtropical high pressure systems to shift north. The resulting large scale subsidence is critical to the formation of persistent low and mid-level stratiform clouds that characterize this region. When the ITCZ is displaced southward, this high pressure system cannot move north to its normal location and the MLC and LLC decrease. During April the ITCZ is normally at its most southern latitude. In 1984 the southerly shift caused abnormally high MLC, resulting in decreased OLR and positive NET anomalies.

The areas off the west coast of South America and Africa have been shown to have the greatest variability in the annual average net radiation balance. The NET variation in both were caused not by changes in large scale convective cloud changes, but instead by changes in middle and low level clouds. These cloud types alter the normal reciprocity of the albedo and OLR found in multi-level convective clouds. There are other mid-latitude areas which have similar stratiform cloud characteristics, but these tend to be interannually stable. There is high NET variability in the tropical stratiform areas because these areas are affected by interannual global scale circulation changes such as El Niño.

Chapter 5

ATMOSPHERIC ENERGETICS AND NIMBUS-7 ERB COMPARISONS

Our most primary understanding of how the earth-atmosphere system functions tells us it is the variation of energy, both spacial and temporally that drives the general circulation. This chapter will examine the variability of the atmosphere by using atmospheric energetics derived from ECMWF circulation data for both the Northern and Southern Hemispheres. The energetic differences between hemispheres lets us understand the circulation features unique to each. Finally, the annual cycle and weekly anomalies of the ERB is directly compared with the variability of the energetics.

5.1 Atmospheric Circulation Data

The best global atmospheric data set currently available is from the European Centre for Medium Range Weather Forecasts (ECMWF). This includes both modelled analyses and forecast fields. The excellent data assimilation schemes for the Southern Hemisphere have been shown to produce a more realistic analysis than the NMC gridded data (Koehler and Whittaker, 1985). One product of the ECMWF is the World Meteorological Organization (WMO) Archive. This data includes all the usual meteorological parameters at standard levels and with a $2.5^{\circ} \times 2.5^{\circ}$ grid resolution. The analysis fields used in the model initialization are actually a result of the assimilation scheme that includes data analysis, model initialization and forecast (Lönnerberg and Shaw, 1986). Input data is collected from the GTS (Global Telecommunications System) which includes reports from surface, ship, and buoy stations as well as rawinsonde, pilot reports, aircraft reports and satellite observations. The analysis fields are created as follows. The initial first guess field comes from the ECMWF model 6 hour forecast field. The error is calculated by a differencing and normalization process between the first guess model field and that derived from actual

observations. The three-dimensional analyzed fields are interpolated using a multivariate optimal interpolation scheme which is fully described in Lorenc (1981). This scheme is dependent on the different error characteristics of each variable. This process to form the initial or analysis fields is therefore a modeled approach and the results more closely resemble the balanced atmosphere. This makes it an excellent choice for study of global scale derived quantities such as the energetics. Trenberth and Olson (1988) have made an extensive evaluation of the ECMWF analyses over seven years from 1979 – 1986 and summarized the periodic changes to ECMWF model. When trends due to model changes could be noted they have been removed from the derived energetic results before comparisons were analyzed. More will be discussed on data quality later as it becomes appropriate.

The atmospheric data used in the energetic calculations are from only the 12 UTC analysis fields. The variables included the U and V component winds for the calculation of the kinetic energy, and the temperatures fields for calculation of the available potential energy. Vertical levels included 1000, 850, 700, 500, 300, and 200 mb.

5.2 Energetics

5.2.1 Kinetic Energy

The atmospheric kinetic energy is a measure of the magnitude of atmospheric motion. It is most commonly split into its zonal (KE_z) and eddy (KE_e) components. The KE_z uses the zonal averaged U and V components to calculate the mean motion energy. From Oort (1964) the KE_z restricted to only the space domain can be expressed by:

$$KE_z = \frac{1}{2} \int ([u]^2 + [v]^2) dm$$

The eddy kinetic energy KE_e is the amount of energy attributed to variability in the east-west or zonal direction. It can be thought of as the amount of variability in the atmospheric wind field within an individual zonal latitude ring:

$$KE_e = \frac{1}{2} \int (\overline{[u^{*2}] + [v^{*2}]}) dm$$

Where the brackets represent a zonal average, the asterisk a deviation from the zonal average, and the bar a time average. The integrals were evaluated in isobaric coordinates by representing dm as $-\frac{1}{\rho g} dp$ and applying a trapezoidal integration scheme to each vertical layer from 1000 to 200 mb. Zonal averages of KE_z and KE_e were calculated for each day in the ECMWF data set from January 1, 1980 – November 1, 1987. The zonal averages were then combined and averaged into a data set concurrent with the weekly averaged ERB data. This provided 45 periods per year, or 355 consecutive periods in the complete time series. Hemispheric averages from $20^\circ - 90^\circ$ were then calculated for each weekly period.

Figure 5.1 presents the KE_z and KE_e time series over the eight years and shows many differences between the hemispheres. The Southern Hemisphere (SH) KE_z values are higher which are indicative of the greater zonal wind speeds. In contrast the KE_e is much higher in the Northern Hemisphere (NH), pointing to greater amplitude mid-latitude waves. The range of the annual cycle shows pronounced hemispheric bias where the NH varies almost twice that of the SH.

5.2.2 Available Potential Energy

The available potential energy is defined in the classic paper by Lorenz (1955) as the difference between the total potential energy and that of a horizontal stably stratified reference state which would result from an adiabatic redistribution of mass. The total available potential energy is commonly split into two components: the zonal available potential energy (PE_z) and eddy available potential energy (PE_e). The generation of PE_z results from the unequal distribution of incoming solar radiation with latitude. In addition estimates by Oort and Peixoto (1974), have included the PE_e as a energy generation term when transient eddies are included. Thus the variability of radiation in the east-west direction adds to the total available potential energy. In a crude sense, the available potential energy is a measure of the energy available for conversion to kinetic energy.

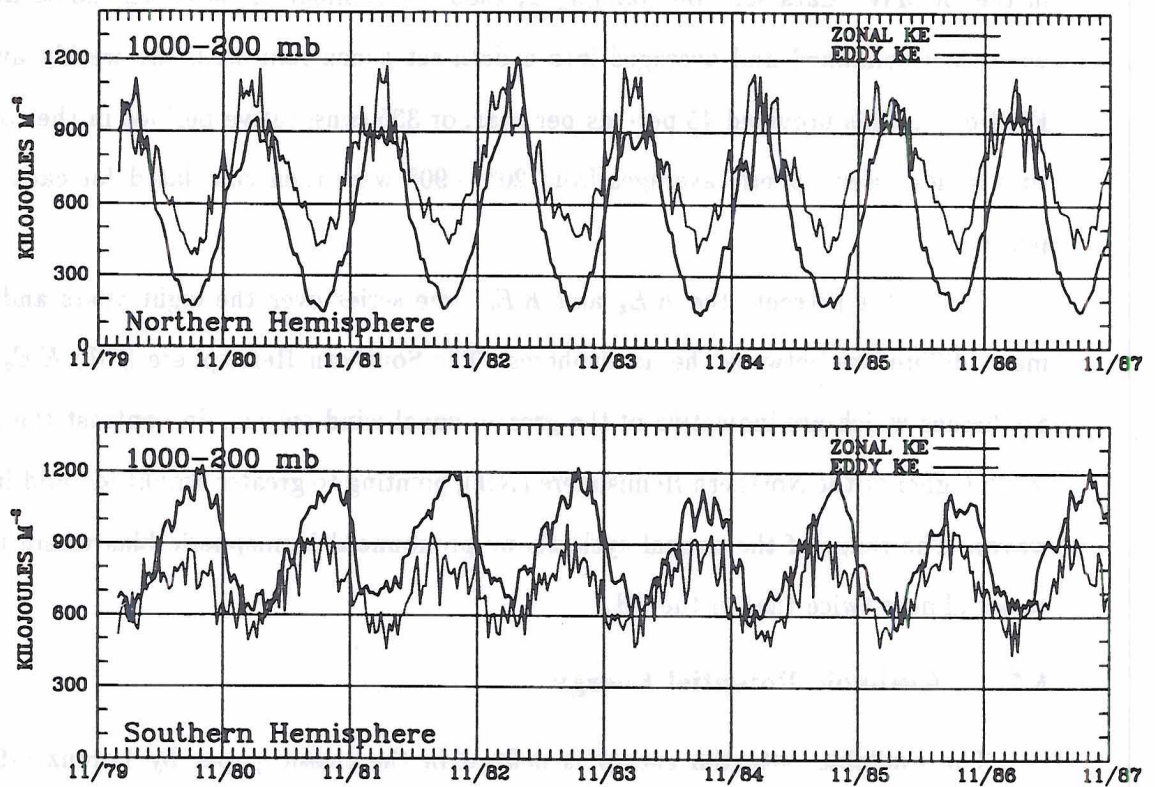


Figure 5.1: Eight years of zonal and eddy kinetic energy, January 1980 – November 1987. Northern and Southern Hemisphere averages from 20° – 90° latitude.

While the magnitude of the available potential energy may seem great, it is less than $\frac{1}{2}$ % of the total potential energy (Krueger, et al., 1965).

The equations for zonal and eddy available potential energy used here are the approximate form with variable static stability:

$$PE_z = \frac{1}{2} C_p \int \overline{\gamma [T]''^2} dm$$

$$PE_e = \frac{1}{2} C_p \int \overline{\gamma [T^{*2}]} dm$$

where:

$$\gamma = - \left(\frac{\Theta}{T} \right)^2 \frac{R}{C_p p_0} \int_0^{p_0} \left(\frac{T}{\Theta} \right) \frac{1}{p} \left(\frac{\partial \tilde{\Theta}}{\partial p} \right)^{-1} dp$$

The notation is as follows: Θ = potential temperature, R = gas constant, $p_0 = 1000\text{mb}$, C_p = specific heat at constant pressure, $(\bar{\quad})$ = area average over a closed pressure surface, and $(\quad)''$ = deviation from the area average.

This 'approximate' form allows for easy computation of available potential energy on isobaric surfaces. The exact form is calculated by differencing directly the total potential energy from the amount at a specified reference state after temperatures are interpolated to isentropic surfaces. It was reported by Oort (1964) that the approximate form has minimal error for global or hemispheric scale studies. This form assumes that the pressure and static stability over the closed pressure surface do not vary in space and time. The approximate form was found to be not valid when regional scale studies are attempted (Min and Horn, 1982). In all subsequent results the approximation equations are used as this study concentrates on hemispheric scales and the ECMWF temperature fields remain on isobaric coordinates.

Since the PE_z depends on the deviation from an area average the latitude range over which the PE calculations were valid had to be defined during processing of the temperature data. Two hemispheric areas were defined from $20^\circ - 90^\circ$ north and south latitude. The data calculations followed similar processing as the kinetic calculations, resulting in 45 time periods per year and a 355 period time series.

As stated earlier, our final goal is to relate the changes in the atmospheric energetics to observed variability in the ERB. To this end, the energetic averages must be concurrent with the ERB averages. Since the ERB averages were a combination of 7-8 days, energetic eddies that vary only in the space domain could be used. The above equations reflect this limitation.

Figure 5.2 shows the individual hemisphere time series of PE_z and PE_e . A simplification of the PE_z values is that the PE_z represents the gradient of temperature, in this case over the latitude range $20^\circ - 90^\circ$. We can see that the SH PE_z is much higher than the NH due to a larger temperature gradient brought about by the lower OLR in the SH polar region. The other potential energy component, PE_e can be thought of as the variability within a constant latitude zonal ring. Since the SH atmospheric structure is much more zonal with lower amplitude waves, we find the SH PE_e to be less than the NH. As can be seen in Fig. 5.2, the SH PE_e is only half of the NH amount. The strong increase in the potential and kinetic energies in the winter months are indicative of much stronger winter cyclonic systems. The strength of these synoptic and finer scale systems is directly tied to the abundant potential energy available for conversion to kinetic energy. An interannual trend is apparent in the SH PE_z , as changes were made in the ECMWF data retrieval and analyses schemes. This trend is removed for the studies with interannual anomalies.

A version of the Lorenz (1955) or Oort (1964) energetic box diagram is shown in Figure 5.3. A short discussion will help us understand the sources of the energy components and their possible relationship to the ERB parameters. Generation of PE_z results from the uneven distribution of solar radiation causing warming at the equator and cooling at the poles thus producing a zonal temperature gradient. According to the linear baroclinic instability theory, an amplifying small amplitude wave receives energy from PE_z building the wave and producing PE_e . This eddy term is the variability within a latitude zone and is produced when cold air moves south and warm air north at different longitudes. Simultaneously the temperature gradients within the zonal ring force eddy vertical motion creating KE_e . Since only the space domain was used in the energy calculations, all the

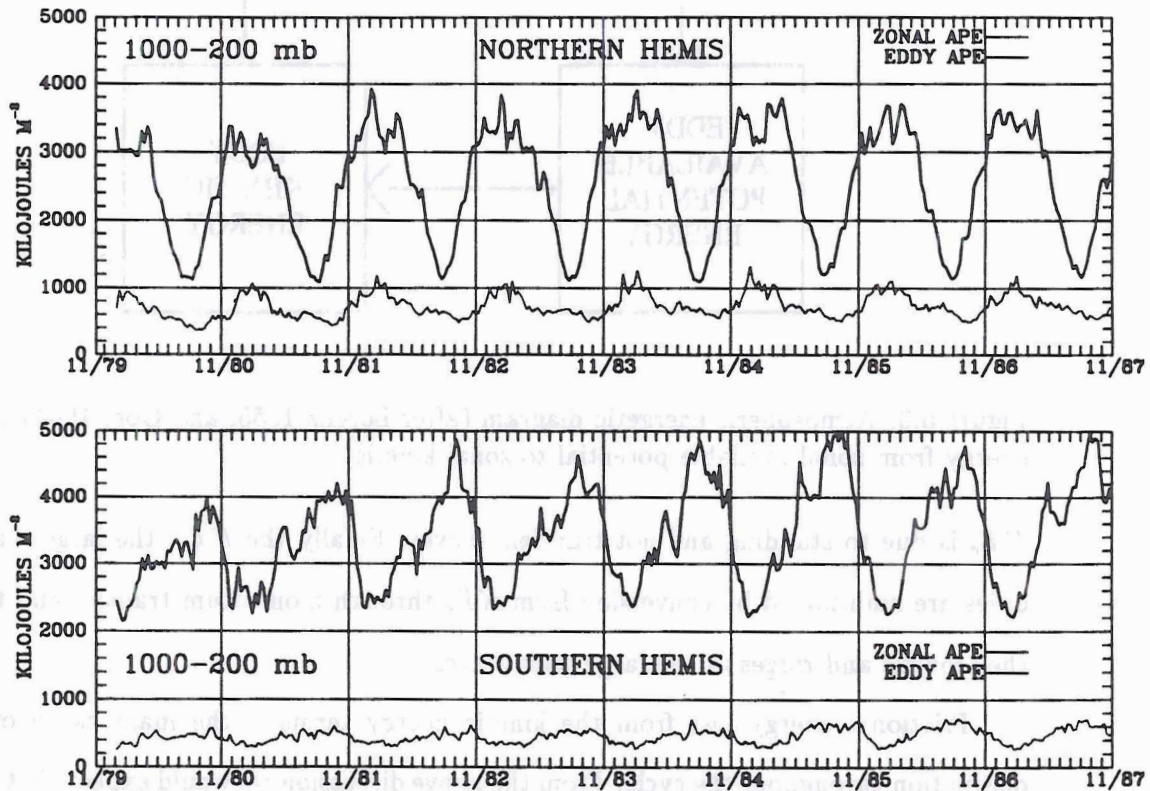


Figure 5.2: Eight years of zonal and eddy available potential energy, January 1980 – November 1987. Northern and Southern Hemisphere averages from 20° – 90° latitude.

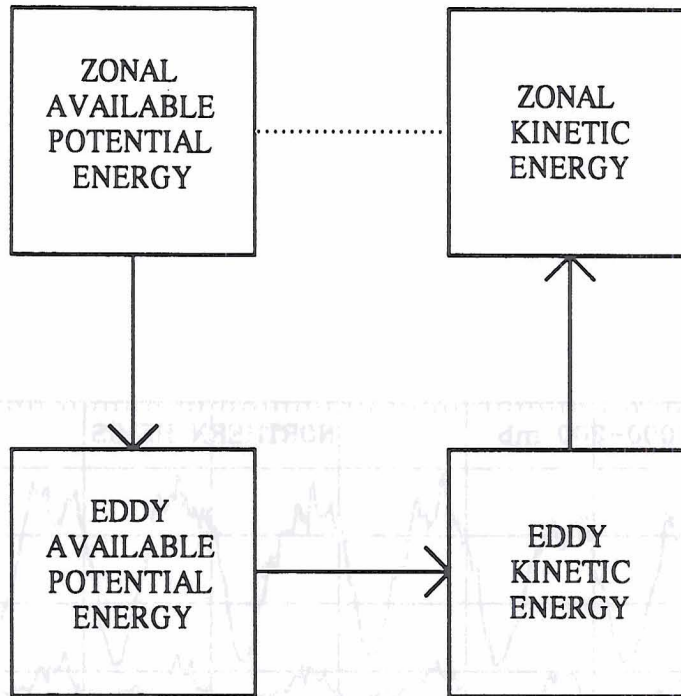


Figure 5.3: Atmospheric energetic diagram (after Lorenz 1955; and Oort 1964) of flow of energy from zonal available potential to zonal kinetic.

KE_e is due to standing and not transient waves. Finally the KE_z , the large scale westerlies are maintained by conversion from KE_e through momentum transfer and tilting of the troughs and ridges in the large scale waves.

Frictional energy loss from the kinetic energy terms is the main cause of energy dissipation throughout the cycle. From the above discussion we would expect that seasonal cycles of the energetic components would be highly correlated, since they rely so heavily on each other for their generation. Table 5.1 presents the correlation coefficients for the annual cycles of the energetics. These cycles are an average of each weekly time period over the eight years. The interaction of the energetics occur with some lag and/or lead time and this information is also included in Tab. 5.1. As a rule the lead times follow our above discussion on the energy conversions except in the SH where the seasonal cycles are often simultaneous. The seasonal cycle of NH PE_z leads the PE_e by 3 weeks, the PE_e leads the KE_e by 1 week, and the KE_e leads the KE_z by 1 week. Seasonal correlations are very high between 0.827 – 0.974. We have seen that in the SH the PE_z is much greater

Table 5.1: Correlation coefficients of the annual cycle of ECMWF derived atmospheric energetics. Lag and/or lead times are given of the maximum correlation values. Level of 1 % error is 0.406 .

Energy Comparison	Maximum Correlation	Time Lag
NH $PE_z - PE_e$	0.827	PE_z leads 3 weeks
NH $PE_e - KE_e$	0.925	PE_e leads 1 week
NH $KE_e - KE_z$	0.974	KE_e leads 1 week
NH $KE_z - PE_z$	0.940	PE_z leads 1 week
SH $PE_z - PE_e$	0.955	PE_z leads 1 week
SH $PE_e - KE_e$	0.952	simultaneous
SH $KE_e - KE_z$	0.971	KE_e leads 3 weeks
SH $KE_z - PE_z$	0.972	simultaneous

and PE_e is lower than the NH. We might speculate that the SH PE_z leads by only one week due to the greater amount of PE_z , and its ability to convert to PE_e faster. Though the SH eddies are not as strong as the NH they seem to be more directly tied to the PE_z . The SH correlation of KE_e and KE_z has the KE_e leading by 3 weeks which is longer than the NH.

By removing the annual cycle from the 8 year time series we are left with the individual weekly anomalies. Comparisons of the different energetic term anomalies shows some interesting results but the maximum correlation in all instances occurs with zero lag or lead time. The correlation is sometimes negative and most pronounced in the KE_e to KE_z comparison. From Tab. 5.1 we see that the annual cycle of these two terms have the highest correlations. The weekly correlations point out the reciprocity of the anomalies. One might state that there can only be so much kinetic energy and it is divided between the eddy and mean terms. Extremely high correlations are found between the PE_e and KE_e anomalies, again pointing out the strong conversion relationship. All the energetic anomaly correlation coefficients are presented in Table 5.2. The full 355 week time series was used for the correlations so the level of 1 % error, the test of significance, drops to 0.139 .

Table 5.2: Correlation coefficients for the weekly anomalies of ECMWF derived atmospheric energetics. The maximum correlation occurred in each case with no time lag. Time series of 355 weekly periods. Level of 1 % error is 0.139 .

Energy Comparison	Maximum Correlation
N.Hemis $PE_z - PE_e$	0.177
N.Hemis $PE_e - KE_e$	0.541
N.Hemis $KE_e - KE_z$	-0.292
N.Hemis $PE_z - KE_z$	-0.156
S.Hemis $PE_z - PE_e$	0.200
S.Hemis $PE_e - KE_e$	0.602
S.Hemis $KE_e - KE_z$	-0.470
S.Hemis $KE_z - PE_z$	0.192

5.3 ERB and Energetics Comparisons

5.3.1 Annual cycle

During the comparison of mid-latitude ERB and atmospheric energetics, many different ways of examining the ERB data were attempted. The zonal mid-latitude averages were too greatly skewed by the simple seasonal cycle of the incident radiation to produce meaningful relationships. The ultimate purpose of the energetic annual cycle is to balance the difference of NET energy between the equator and poles. Examination of the gradients of OLR and NET across $30^\circ - 60^\circ$ seemed to mirror this purpose as this 'defines' the required energy transports. The primary interaction of the energetics and radiation budget must begin with the PE_z as this is the driving energy source for the other energetics parameters. Figures 5.4 and 5.5 show, for both hemispheres, the 8 year annual cycle of the PE_z simultaneously with the NET and OLR mid-latitude gradients. The maximum correlation coefficient and the offset lag or lead are presented in Table 5.3. The NH NET and OLR gradients closely match the annual PE_z cycle but lead by 2-3 weeks. In the early winter season the NET and OLR gradients increase as the poles cool greatly. The pole to mid-latitude temperature gradients increase and the total atmospheric transport needed to balance the difference grows. The increased temperature differential specifies that the PE_z also increases. The SH NET and OLR gradients lead by 1-2 weeks less than

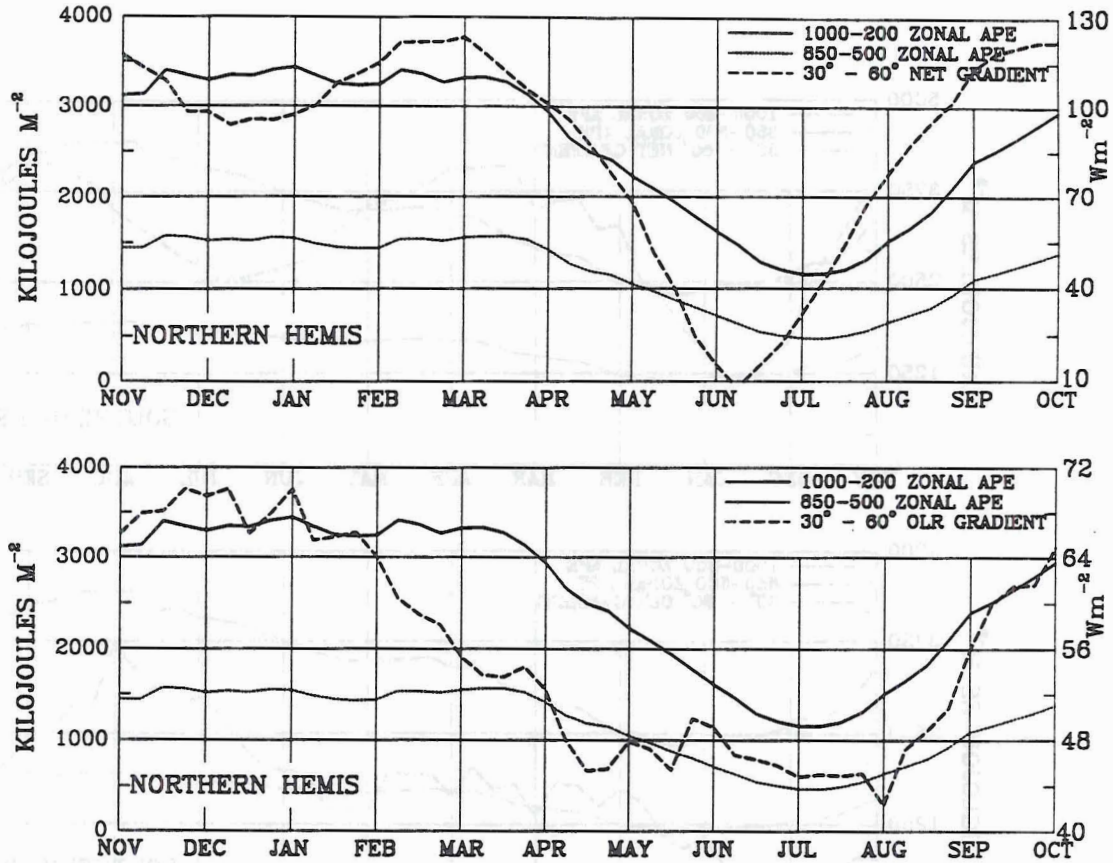


Figure 5.4: Northern Hemisphere eight year annual averaged cycle of zonal available potential energy and the gradients from $30^{\circ} - 60^{\circ}$ of NET and OLR.

the NH thus showing a quicker response of the atmosphere to radiative changes. The SH's lack of continental locking of the transient and standing waves allows for fast changes to its wave patterns. In contrast the NH strong continental cooling and heating tends to cause a stabilizing effect on the transient wave patterns thus causing a slower atmospheric response to the radiation variability. In summary, the annual PE_z cycle is responding to the seasonal cycle of NET and OLR mid-latitude gradients. In the next section an examination of the weekly anomalies is presented. This will probe the circulation - ERB connections which have short term weekly variability.

5.3.2 Weekly Anomalies

Here we compare the 8 year time series weekly anomalies. As mentioned previously this time series is comprised of 355 periods of approximately 1 week in duration. The

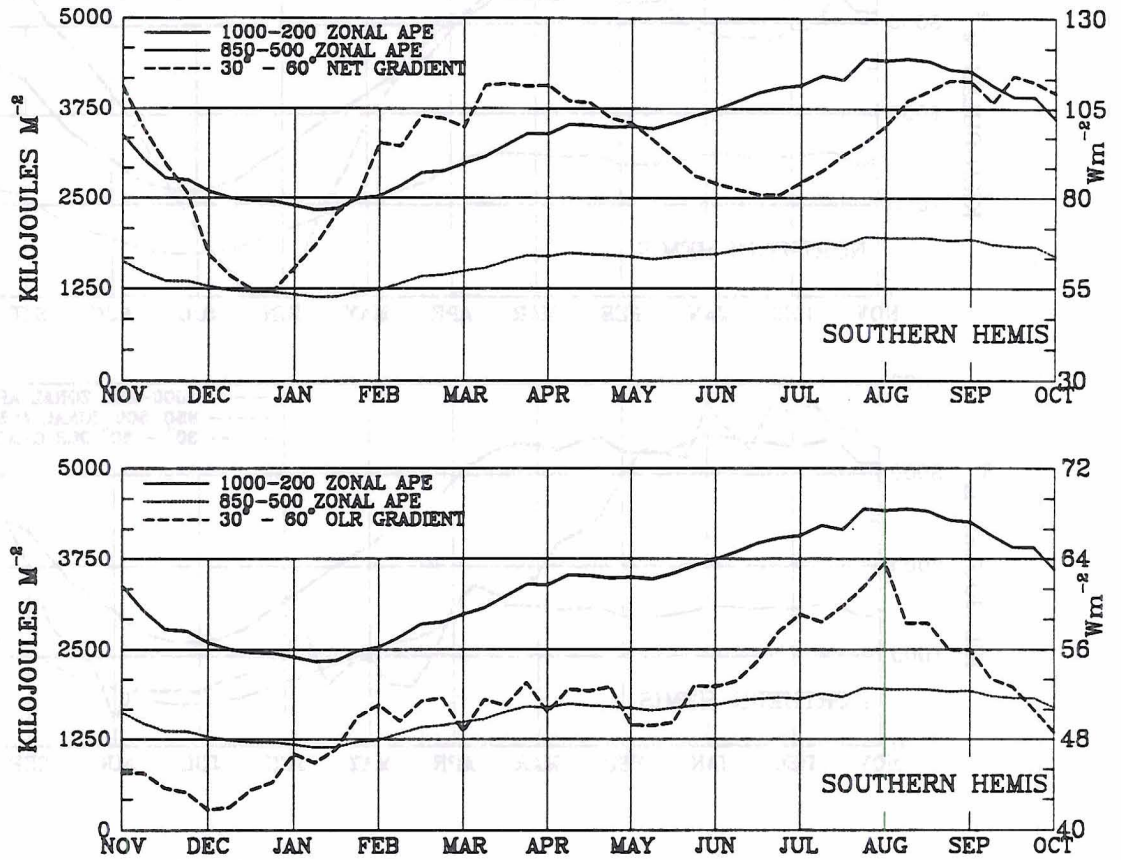


Figure 5.5: Southern Hemisphere eight year annual averaged cycle of zonal available potential energy and the gradients from 30° - 60° of NET and OLR.

Table 5.3: Correlation coefficients for the annual cycles of zonal available potential energy (PE_z) and the gradients of NET and OLR from 30° - 60°. Level of 1 % error is 0.406 .

ERB PE Comparison	Maximum Correlation	Time Lag
NH NET - PE_z	0.905	NET leads 3 weeks
NH OLR - PE_z	0.875	OLR leads 2 weeks
SH NET - PE_z	0.544	PE_z leads 1 week
SH OLR - PE_z	0.913	OLR leads 2 weeks

purpose of these comparisons is to find connections with short, weekly variability between the atmospheric energetics and ERB at concurrent times or with 1-4 week lag or leads. Anomaly comparisons were made of the zonal energetic quantities with mid-latitude ERB gradients. These measurements are similar in that they both are directly related to poleward transport of energy. Also the eddy energetic terms measure the variability within each zonal ring and these are compared to the variability within each zone of the ERB quantities. This is done by computing the variance within the zone of the ERB OLR and NET parameters. We would expect the PE_e to have a high correlation with the variance of OLR since both indirectly 'measure' the variability of temperature with a zone.

There was an additional error correction applied at this point to the ERB and energetic anomaly time series. Each of the time series had any long term trend removed by a least squares approximation to minimize correlation attributed to long term trends. Removing the long term trend from the data successfully removes a source of error for these types of correlations. The SH ECMWF temperature data included additional error from ECMWF analysis and data retrieval changes during the first three years (Trenberth and Olson, 1988). A separate trending approximation for these three years was performed and seems to have reduced this error. However this reduces our confidence somewhat in the significance of the SH correlations. Figures 5.6 and 5.7 present the eight year anomaly time series for the NET and OLR mid-latitude gradients. The amplitude of the variability averages around 5 Wm^{-2} , and is approximately 10% of the normal gradient values as shown in figures 5.4 and 5.5.

Table 5.4 presents the correlation coefficients for the ERB gradient and energetic comparisons. For the NH, we find good correlation in the OLR and PE_z with no time lag, but near the minimum accepted correlation between the PE_z and NET. The PE_e has significant correlation with both the OLR and NET gradients but are reversed in sign. Therefore as the gradient of OLR increases the PE_e decreases. The KE_z and KE_e are negatively correlated with the OLR gradient.

Another ERB variable was derived from the ERB NET data, the total energy transport. This is computed by integration of the NET from the north pole, a technique previously used and discussed by Oort and Vonder Haar (1980), and Carissimo, et al. (1985).

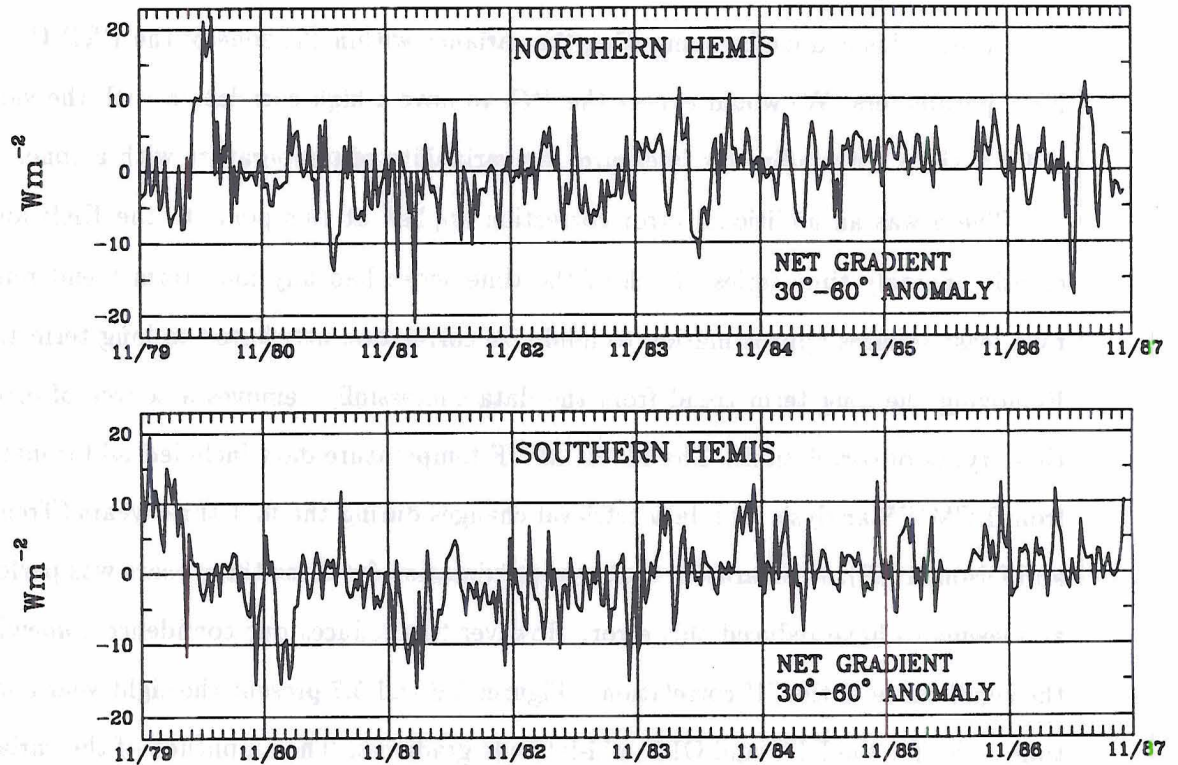


Figure 5.6: Eight year time series of Northern and Southern Hemisphere NET gradient ANOMALY from $30^{\circ} - 60^{\circ}$ in (Wm^{-2}). Magnitude of the variability is approximately 10% of the actual gradient.

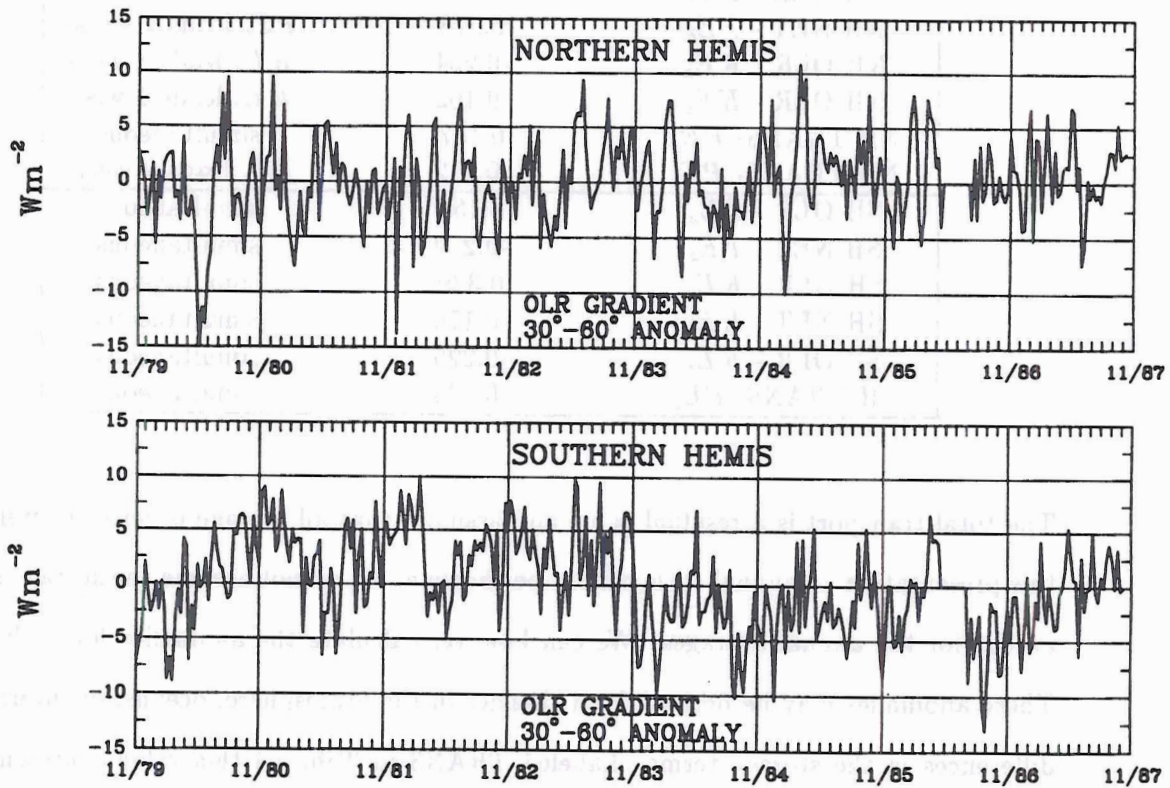


Figure 5.7: Eight year time series of Northern and Southern Hemisphere OLR ANOMALY as in the previous figure.

Table 5.4: Correlation coefficients for the weekly ERB vs energetic anomalies. NET and OLR are gradients from $30^\circ - 60^\circ$. TRANS is the required total energy transport. Correlations are from concurrent 355 period time series. Lag and/or lead times are given of the maximum correlation values. Level of 1% error is 0.137.

Anomaly Comparison	Maximum Correlation.	Time Lag
NH OLR - PE_z	0.361	simultaneous
NH NET - PE_z	-0.153	PE_z leads 1 week
NH OLR - PE_e	-0.227	PE_e leads 1 week
NH NET - PE_e	0.218	PE_e leads 2 weeks
NH OLR - KE_z	-0.204	KE_z leads 1 week
NH OLR - KE_e	-0.162	KE_e leads 1 week
NH TRANS- PE_z	0.157	simultaneous
NH TRANS- PE_e	-0.212	PE_e leads 2 weeks
SH OLR - PE_z	0.157	simultaneous
SH NET - PE_z	-0.239	simultaneous
SH OLR - KE_z	0.329	simultaneous
SH NET - KE_e	-0.176	simultaneous
SH OLR - KE_e	-0.225	simultaneous
SH TRANS- PE_z	-0.233	simultaneous

The total transport is a residual value and assumes that all storage is zero. Therefore in this presentation an annual cycle cannot be shown as we cannot assume the storage is zero except for the annual averages. We can however calculate the anomalies for each week. These anomalies may be derived from changes in the atmosphere, oceans, or interannual differences in the storage terms. Labeled TRANS in Tab. 5.4 this value represents the anomalous total energy transport between $30^\circ - 60^\circ$ needed to balance the NET gradient. Tab. 5.4 also lists the significant correlations between TRANS and PE_z and PE_e .

In most of these NH comparisons the energetic anomalies lead the ERB anomalies by 1–2 weeks. This is in contrast to the seasonal annual cycle where generally the ERB terms lead the energetics. This seems to suggest that variability in the ERB doesn't force the energetic changes but the reverse may actually be true. The significant SH correlations are also listed in Tab. 5.4 and show many of the same relationships as the NH. The basic difference is that the lead/lag times of the maximum correlation are always zero. We speculate this may be due to the lack of continental influences in the SH, the associated

Table 5.5: Correlation coefficients for the weekly ERB zonal variance and eddy energetics anomalies. The maximum correlation occurred in each case with no time lag. Time series of 355 weekly periods. Level of 1 % error is 0.139 .

Anomaly Comparison	Maximum Correlation
N. Hemis OLR - PE_e	0.346
N. Hemis NET - PE_e	0.207
N. Hemis OLR - KE_e	0.272
S. Hemis OLR - PE_e	0.171

relatively constant temperature gradients, and consistent atmospheric wave patterns from year to year.

Table 5.5 lists the significant correlations of the zonal variance ERB terms and the eddy energetic terms. As discussed previously the eddy terms should have a correlation to the variability within each zone of the ERB. Significant NH correlations are found between the OLR and PE_e , the NET and PE_e , and reflecting the high correlation of PE_e to KE_e , and OLR to KE_e . In the SH only the PE_e and OLR comparison was significant.

5.4 Winter Only Correlations

As an experiment, correlations were computed with a subset of the time series for the comparisons previously presented. As previously shown, the summer months are the time of minimum OLR and NET gradients as well as potential and kinetic energies. It was believed that if correlations were made using only the winter months for 8 years, the relationships between all the parameters would be stronger. This section is an attempt to prove that hypothesis. Table 5.6 presents the difference in correlation coefficient using just the winter months of the relationships previously presented in Tables 5.2 – 5.5. The data year was actually evenly split so that for the NH these months are defined as November 1 – May 1. The other 6 months of the year define the SH winter months.

As can be seen in Tab. 5.6 there are large differences between the entire year correlations and the winter only samples. In almost every case using only the winter weeks increased the correlation. This increase was most prevalent in the NH total atmospheric

Table 5.6: Weekly anomaly differences of the correlation coefficients for the 'winter' months versus the full year time series. The correlations using the full year are shown in previous tables. The Northern Hemisphere has 184 samples, the Southern Hemisphere, 176, for a level of significance at 1 % error of 0.195 .

Anomaly Comparison	Winter Correlation	Difference(X 100)
NH $PE_z - PE_e$	0.257	8.0
NH $PE_e - KE_e$	0.559	1.8
NH $KE_e - KE_z$	-0.276	-1.6
NH $PE_z - KE_z$	-0.226	8.0
SH $PE_e - KE_e$	0.584	-1.8
SH $KE_e - KE_z$	0.489	1.9
NH OLR grad - PE_z	0.391	3.0
NH NET grad - PE_z	0.217	6.4
NH OLR grad - PE_e	-0.230	0.3
NH NET grad - PE_e	0.233	1.5
NH OLR grad - KE_z	-0.297	9.3
NH TRANS - PE_z	0.320	16.3
NH TRANS - PE_e	-0.317	10.5
SH OLR grad - PE_z	-0.279	12.2
SH NET grad - PE_z	-0.291	5.2
SH OLR grad - KE_z	0.401	7.2
SH NET grad - KE_z	-0.287	11.1
SH OLR grad - KE_e	-0.251	2.6
SH TRANS - PE_z	-0.314	8.1
NH STD OLR - PE_e	0.480	13.4
NH STD NET - PE_e	0.344	13.7
NH STD OLR - KE_e	0.294	2.2
SH STD OLR - PE_e	0.249	7.8

transport anomaly (TRANS) to PE_z and PE_e comparisons. Also the NH OLR gradient vs. KE_z correlation increased greatly. In the SH the largest improvements came with the OLR to PE_z comparison and in the NET to KE_e . The comparisons within each zonal ring (STD), done by calculating the variance of the ERB quantities and the eddy terms, strongly improved in the NH but showed little SH difference.

5.5 Discussion and Summary

Eight years of *Nimbus-7* Earth Radiation Budget (ERB) measurements have been compared with a simultaneous time series of ECMWF derived northern and southern hemisphere potential and kinetic energies. The seasonal cycles of each proved to be highly correlated as the same driving force, the solar annual cycle, accounts for most of the ERB variability. The correlation of the energetic cycles of zonal and eddy available potential energy and eddy and zonal kinetic energy tend to substantiate our current understanding of the atmospheric energy cycle. The ERB mid-latitude gradients of NET and OLR were shown to lead the annual cycle of the energetics by 2-3 weeks. The amount of explained variance for the annual cycle comparisons was between 68% – 95% for the energetic to energetic terms and as high as 82% for the NH NET – PE_z comparisons. Weekly anomalies of the ERB and energetics were correlated and significant correlations were found. These anomalies tended to occur simultaneously in contrast to the annual cycles where the ERB always leads. The amount of explained variance is the correlation coefficient squared so even though the correlations proved to be mathematically significant, a small part of the total variance in the weekly anomalies could be explained. Generally the amount of explained variance for the weekly anomaly comparisons were from 6% – 35% in the energetic comparisons, 6% – 16% for the ERB to energetic comparisons, and 6% – 23% for the zonal variance and eddy term connections. These values seem low but we must remember these are averages on hemispheric scales and are more a climate scale indicator than that of individual weather systems. If smaller regional areas were included the correlations would certainly have been much higher. For this type of study, the set of potential and kinetic energy equations must include both time and space variability

components with would include the transient eddies. This was not possible here due to the constraint of the composite 7-8 day ERB fields.

the comparison and in the NET to A.E. The comparison within each con-
the variance of the ERB quantities and the eddy term
strongly increases in the NH but showed little NH difference.

3.2. Discussion of a summary

Eight years of January-February (ERB) measurements have been
with a simultaneous time series of ECMWF derived northern and southern
hemisphere potential and kinetic energy. The seasonal cycle of each proved to be highly
correlated with the same driving force, the solar annual cycle, as occurs for most of the ERB
variability. The correlation of the energetic cycle of zonal and eddy available potential
energy and eddy and zonal kinetic energy lead to substantial out current understandings
of the atmospheric energy cycle. The ERB mid-latitude gradient of VET and OLE
was shown to lead the annual cycle of the energy by 2-3 weeks. The amount of
explained variance for the annual cycle comparisons was between 68% - 92% for the
correlation to energetic terms and as high as 82% for the NW NET - VET comparison.
Weekly anomalies of the ERB and energetic were correlated and significant correlations
were found. These anomalies tended to occur simultaneously in contrast to the annual
cycles where the ERB always leads. The amount of explained variance in the correlation
coefficients equaled or even the sign the correlations proved to be statistically significant,
a small part of the total variance in the weekly anomalies could be explained. Generally
the amount of explained variance for the weekly anomaly comparisons were from 67
50% in the energetic comparisons, 6% - 16% for the ERB to energetic comparisons, and
6% - 23% for the zonal variance and eddy term comparisons. These values seem low but
we must remember these are variance on hemispheric scales and are more a climate scale
indicator than that of individual weather systems. If smaller regional areas were included
the correlations would certainly have been much higher. For this type of study, the set
of potential and kinetic energy equations must include both time and space variability

Chapter 6

OBSERVED NIMBUS-7 ERB TELECONNECTIONS

The severity of the 1982-1983 El Niño event intensified efforts to understand the effects of large tropical changes on the mid-latitude climate. Many observational and general circulation model studies have been published which examined changes in tropical convection, sea surface temperature, and wind fields (Liebmann and Hartmann 1982; Webster 1982; Geisler et al. 1985;) and their correlation with mid-latitude circulation properties. Areas of anomalous tropical convection define the regions where variability of the normal vertical motions, and release of latent heat might create tropical heat sources or sinks. The outgoing longwave radiation (OLR) anomalies measured from satellites have been used as a indirect method of measuring these anomalies in the vertical motion fields. The observational studies which use changes in tropical convection most often use tropical OLR from scanning radiometers on the series of NOAA polar orbiting satellites radiometers (Liebmann and Hartmann, 1984). The greatest advantages to these instruments are their long time series of observations during the '70s and '80s, and their high spatial resolution. A major disadvantage is their inability to accurately represent the total reflected energy and thus no NET calculation is routinely performed.

This study requires the tropical NET anomalies and therefore incorporates a different and unique set of satellite observations from the *Nimbus-7* ERB instruments. From these broadband observations accurate NET anomalies as well as the OLR anomalies are available. The NET anomalies define regions that act directly as radiative heat sources or sinks without assuming that only latent heating is the source. The tropical areas with significant OLR and NET correlations point out the strength of the tropical circulation patterns that make up the El Niño and Southern Oscillation. Teleconnections of the ERB parameters

with mid-latitude ECMWF 500 mb geopotential heights (GH) for both the Southern and Northern Hemispheres shows interesting and significant correlations patterns.

Generally the ERB to geopotential height teleconnections results in low correlation values. Due to the long time series of observations (355 consecutive weeks), the correlation values can be low and still be within a statistical significant range. However the lower the correlation coefficient the lower the explained variance. The amount of explained variance is only of the order of 5 -15%. It is beyond the scope of this study to definitively explain the cause and effect relationships between the tropical ERB and mid-latitude circulation patterns. This study is searching for a signal, even a small signal, that helps to understand the variability of mid-latitude 500 mb heights. We feel that explaining even 10% of this variability, related to tropical changes, makes a significant contribution and points to areas of future research. The global distribution of these ERB to 500mb teleconnection patterns are presented in section 6.2. Before we look at these tropical – mid-latitude interactions we will examine, in the following section, the simultaneous relationships in OLR and NET fluctuations and the tropical circulation they imply.

6.1 ERB to ERB Comparisons

6.1.1 Background

As in the previous chapter, the ERB data includes the composite 6 day averaged data set. This includes 45 time periods per year, continuous from November 1978 – October 1986 with the exception of two months in April and May 1986. Eight year averages and anomalies were computed for each of the weekly averages. This produced a 355 point time series of anomalous OLR or NET for each of the the 3200 global areas. The OLR and NET standard deviations presented in figures 4.1 and 4.3 were used to define the areas of greatest variability. These areas were used as the center or reference points for the teleconnections. In the NET these areas were: the eastern tropical Atlantic off the west coast of Africa, the eastern Pacific near South America, and the western Pacific northeast of the Indonesian oceanic continent. For the OLR the areas were: central South America in Brazil, the central Pacific on the equator, and the western Pacific northeast

of Indonesia. The OLR and NET anomaly time series in each of these six reference areas were correlated with the anomaly time series over all global grid points which results in global maps of the correlation coefficient (CC). The correlation coefficient for comparison of the two time series is given by:

$$CC_{xy} = \frac{\frac{1}{N} \sum_{n=1}^N (X_n - \bar{X})(Y_n - \bar{Y})}{\left[\left(\frac{\sum_{n=1}^N (X_n - \bar{X})^2}{N-1} \right) \left(\frac{\sum_{n=1}^N (Y_n - \bar{Y})^2}{N-1} \right) \right]^{\frac{1}{2}}}$$

Examination of these relationships provides an excellent method of defining the tropical areas with circulation interaction, even though these areas may be separated by large distances. Lau and Chan (1983) used the NOAA scanning instrument data in their study of concurrent OLR anomalies and showed shifts in the South Pacific Convergence Zone and the eastern Pacific dry zone were related to the Southern Oscillation. Heddinghaus and Krueger (1981), and Liebmann and Hartmann (1982) showed that changes both within a season and interannually of tropical OLR were related to changes in tropical general circulation.

The ERB anomaly time series includes the greatest tropical circulation change observed to date. This was of course the 1982 – 1983 El Niño. Many of the strong relationships found here are a direct result of the circulation changes during this time period and their effect on the location and severity of tropical convective clouds. The strongest ERB correlations occurred for the OLR when the reference points were centered in the central and western Pacific ocean. The ERB simultaneous correlations presented in the next set of figures represent correlations for the entire annual cycle time series. No attempt was made to relate seasonal dependant correlations. To examine significance of the correlation the variance test was used. This test depends of the sample size and only explains the level at which there is a 1% chance that the correlations come about from random chance. The amount of explained variance is a better indicator of how much of the variability has been accounted for. For a sample size of 355 points the 99% significance level is 0.14. Any correlation values found below this threshold could be simply chance. Even at this level the explained variance is very low, only 3 %, therefore only values twice the minimum significant correlation were normally examined.

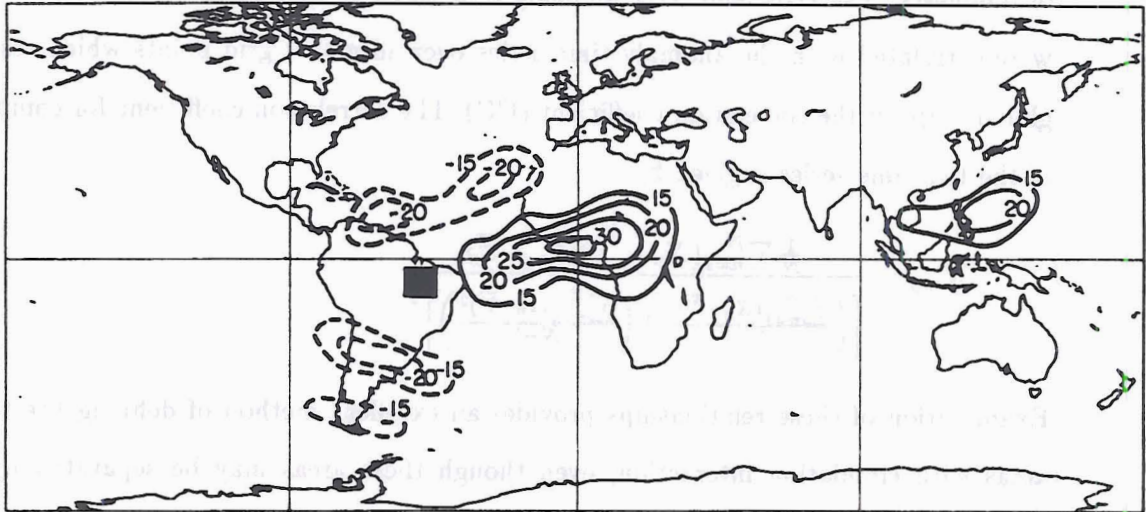


Figure 6.1: Global distributions of correlation coefficient ($\times 10^2$) for the simultaneous teleconnections of OLR anomalies from 11/78 – 10/86. Reference point is the black square and in this case is centered in South America.

6.1.2 OLR Teleconnections

The OLR teleconnection for the first reference area is presented in Figure 6.1. The reference point is centered in central Brazil and shows a large area of positive CC in the Gulf of Guinea as high as 0.30. Positive CC means the OLR anomalies in this areas have the same sign as the reference point. For example when the OLR is above normal at the reference point (representative of less clouds), the area in the Gulf of Guinea would also have less than normal OLR. The South America reference point is normally an area of strong convective clouds, however as a generalization the African area has less vertically developed stratiform clouds. Negative CC are found in two areas to the north and south of South America. These areas are in the downward branch of the Hadley cell. An increase in the tropical convective activity increases the upward motion field which then may cause a representative decrease, due to increased subsidence, in subtropical cloudiness.

Figure 6.2 has its reference point in the central Pacific ocean centered on the equator. This area usually is on the boundary of the dry eastern Pacific area with the much more convective western Pacific. during the El Niño year this area has much greater convective activity while convective cloud amount in the Indonesia area was reduced. The CC over

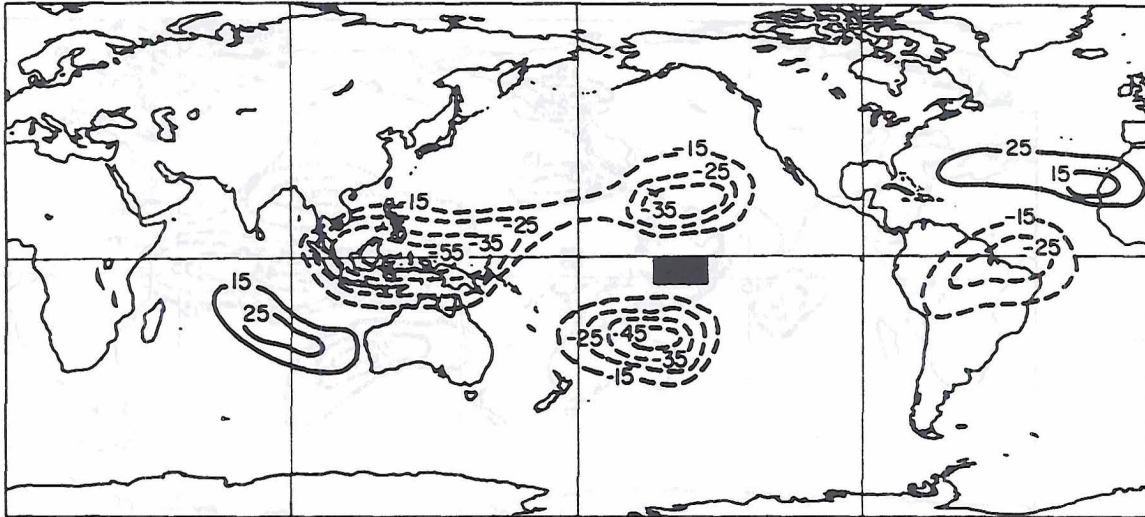


Figure 6.2: Global distributions of correlation coefficient ($\times 10^2$) for the simultaneous teleconnections of OLR anomalies from 11/78 – 10/86. Reference point is the black square and is centered in the central Pacific.

Indonesia was negative and as great as -0.55 . Therefore the OLR anomalies in these two areas are closely related as over 30 % of the variance is explained. These areas are separated by over 100 degrees of longitude which is over 25 % of the earth's circumference. As in the previous figure, there are areas in the subtropics immediately north and south of the reference area which have negative correlations. As before these areas may be tied through changes in the Hadley cell circulation. There are other minor areas of negative correlation off the northwest coast of desert Africa and in Brazil. Lau and Chan (1983) used NOAA OLR anomalies with this same reference area. Their areas of correlations were similar in both area extent and sign.

The strong negative correlation over Indonesia in the previous figure did not fall exactly in the third OLR high variability area but to the west. The final OLR teleconnection area is centered just north of the Equator at 150° E longitude as shown in the CC distribution is presented in Figure 6.3. This area's OLR is normally characterized by low values due to strong vertically developed clouds with high cloud tops. Refer to Chapter 4, figures 4.12 and 4.13 which show the time series of total, high, mid, and low level cloud amount from the *Nimbus-7* CMATRIX cloud climatology. The effect of the El Niño in '82-'83 in this area is easily seen. Much less total and high cloud amount due to the suppression of

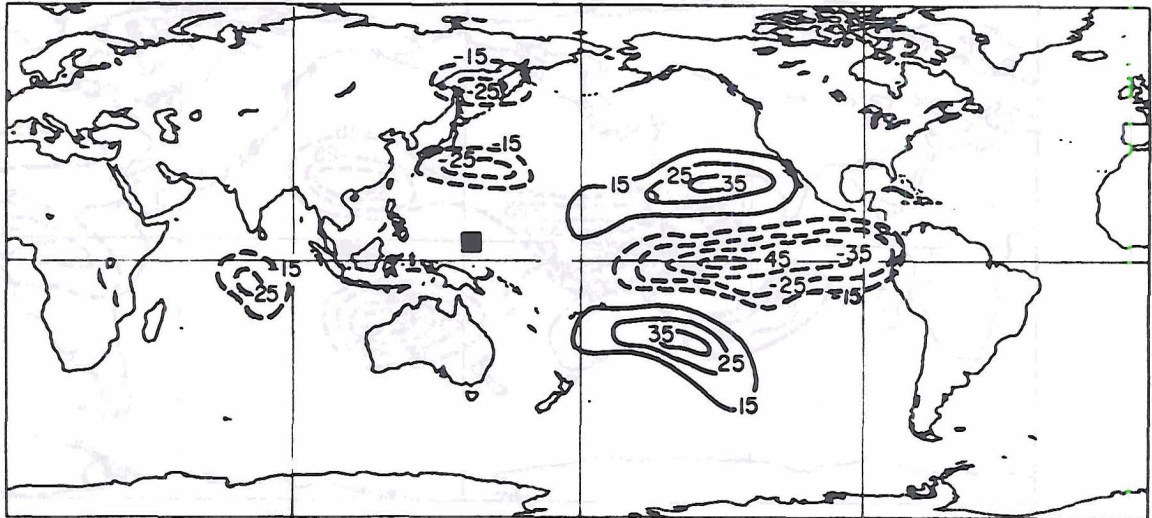


Figure 6.3: Global distributions of correlation coefficient ($\times 10^2$) for the simultaneous teleconnections of OLR anomalies from 11/78 – 10/86. Reference point is the black square and is centered in the western Pacific.

the convection was observed. This caused widely fluctuating OLR values. The opposite forcing of the convection in the central to western Pacific resulted in much greater cloud amounts and heavy rainfall. The relationship between these areas can be seen by the strong negative CC values in the central to eastern Pacific. As before positive correlations are observed in the subtropics and are the reverse of the strong tropical CC values. Also a small area of negative CC south of Japan may have been caused by similar effects.

6.1.3 NET Teleconnections

The next three figures present the NET teleconnection patterns from three areas of highest NET variability. The NET is the difference of the absorbed and emitted irradiances. As previously discussed, changes in convective clouds often lead to little change in the NET as the components of the NET calculation tend to have a reciprocal effect. Most of the large scale cloud changes during the El Niño year were to convective clouds which are easy to identify in the OLR teleconnection patterns. The NET CC values tend to be much less, indicative of the complexity of the shortwave and longwave effects on the NET. Therefore while the OLR teleconnection may explain as much as 30 % of the variance of remotely separately areas, the NET explained variance is never greater than 15 %.

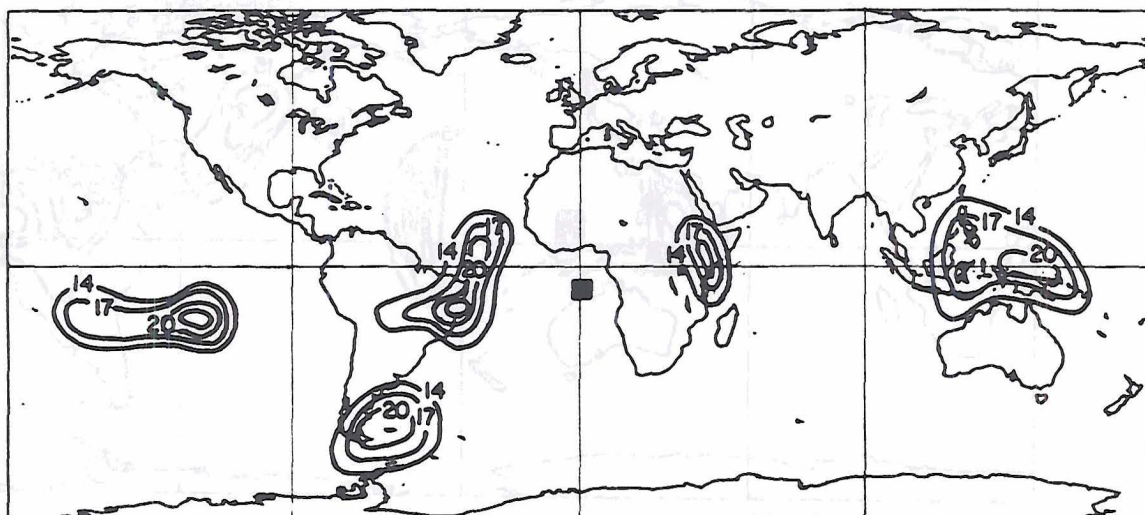


Figure 6.4: Global distributions of correlation coefficient ($\times 10^2$) for the simultaneous teleconnections of NET anomalies from 11/78 – 10/86. Reference point is the black square and is centered off the west coast of Africa in the Gulf of Guinea.

Figure 6.4 shows the simultaneous teleconnection pattern for the area of greatest NET variability off the west African Coast. As discussed in chapter 4, the NET changed drastically in this area due global scale circulation forcing which caused a modification to the low and middle cloud amounts. All of the significant CC areas are positive with the greatest CC occurring in Brazil and nearby off the east South American coast. Significant CC are also found in east Africa, in the central Pacific, and over Indonesia. These are areas which have been shown to be highly linked in the OLR and are roughly equally spaced about the equator. The western Pacific relationship is very strong for an area nearly half way around the world.

The teleconnection pattern for the second NET area is shown in Figure 6.5. This area, centered north of the equator in the western Pacific is the same region of which had a positive CC relationship in the previous figure with the Gulf of Guinea region off Africa. Therefore it is no surprise that the African area also shows a strong (0.33 CC) relationship. The CC between these areas are not an exact reciprocal because the reference points were chosen from the standard deviation plots and not from the teleconnection patterns. There are others areas of significant CC but low explained variance in the mid-Pacific, over the

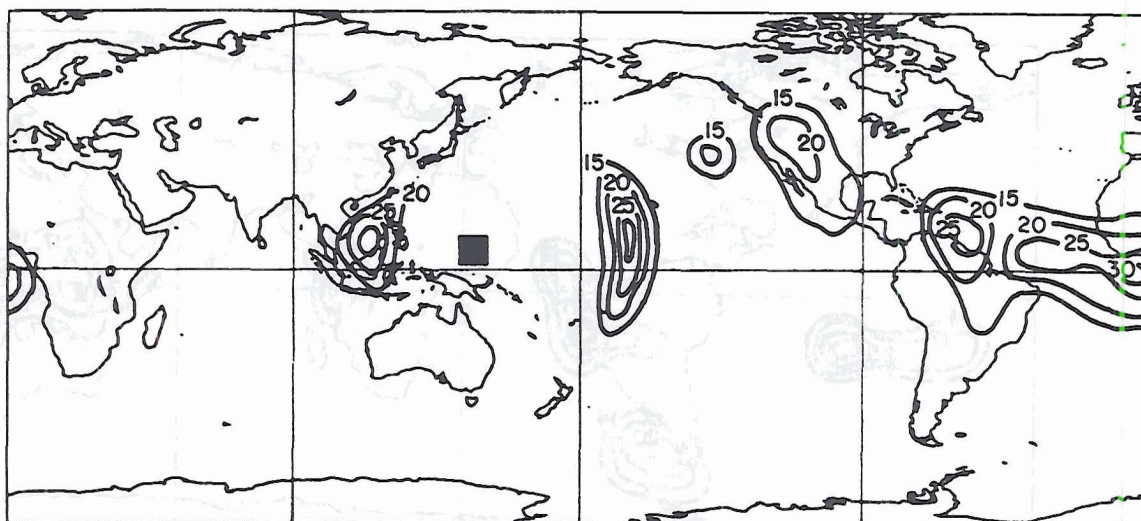


Figure 6.5: Global distributions of correlation coefficient ($\times 10^2$) for the simultaneous teleconnections of NET anomalies from 11/78 – 10/86. Reference point is the black square in the western Pacific.

west coast of the United States, and both to the east and west of the reference area. These close by areas are affected by similar large scale cloud variability which occurred mainly during the El Niño years 1982–1984. From the teleconnection pattern it seems that the whole tropical Atlantic ocean and the area just north of South America also has a positive NET relationship with the reference area, reaching a maximum of 0.28.

Figure 6.6 has as its reference point the last of the three high variability NET areas. This area, centered off the west coast of South America had large changes in convective cloudiness during the El Niño year but little change in the NET. The variability of the NET in this area was greatest before and after the El Niño when the OLR and albedo anomalies were of the same sign (see Chapter 4). Thus only when the cloud types were changing did this area have a large NET fluctuation. The greatest interactions in each of the previous OLR and NET figures were in areas which have large ENSO variability. Therefore, we find few strong correlation areas with this reference area. Areas of significant CC did occur to the west of the reference area and over Venezuela.

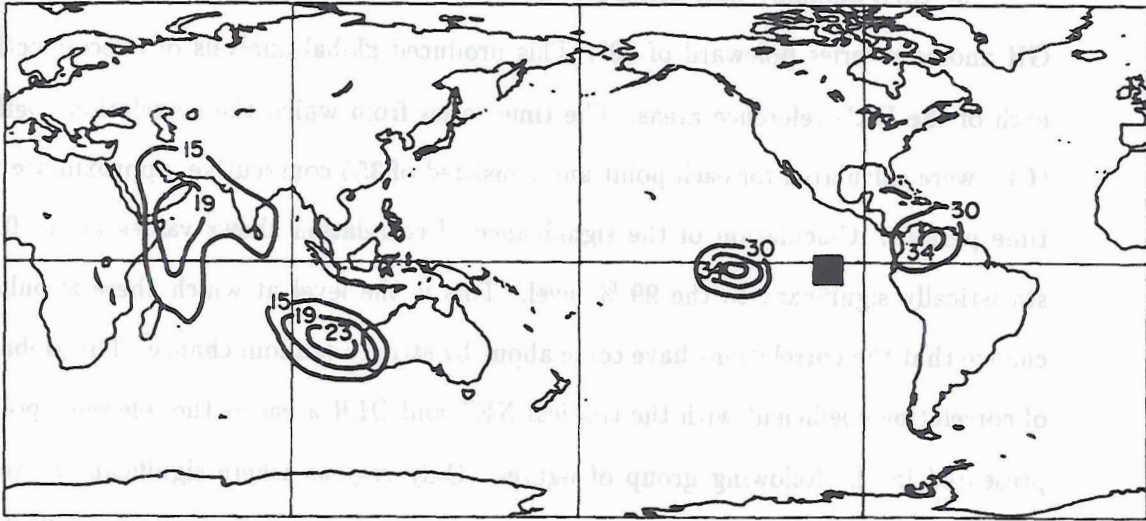


Figure 6.6: Global distributions of correlation coefficient ($\times 10^2$) for the simultaneous teleconnections of NET anomalies from 11/78 – 10/86. Reference point is the black square and is centered in the eastern Pacific.

6.2 ERB to Geopotential Height Comparison

This section will compare the tropical anomalies of ERB NET and OLR with the simultaneous anomalies of mid-latitude 500 mb geopotential heights. The atmospheric data used throughout includes the geopotential heights (GH) from the European Centre for Medium Range Weather Forecasting (ECMWF) 12 UTC initialization fields. The 500 mb global height fields were averaged into approximately weekly time periods simultaneous with the 6 day ERB averages. This study uses ERB and ECMWF data from January 1980 – October 1987. In addition to the weekly averages, weekly anomalies were computed by differencing the individual weekly periods from each eight year sample mean. Other ECMWF processing included resolution degradation as the ECMWF data which was originally on a $2.5^\circ \times 2.5^\circ$ grid and needed to be $4.5^\circ \times 4.5^\circ$ to match the ERB resolution. Error analyses found this to have a minimal effect on the data field.

For the process of calculating tropical to mid-latitude teleconnections identification of areas with highly variable tropical ERB is the first step. As in the previous section these areas were chosen from the ERB standard deviation plots of annual averaged variability. These included 3 areas each for the OLR and NET.

The ERB anomaly time series for these six areas were correlated with each individual GH anomaly series poleward of 20° . This produced global analysis of teleconnection for each of the ERB reference areas. The time series from which the correlation coefficients (CC) were calculated for each point and consisted of 355 consecutive, approximate weekly time periods. Calculation of the significance of correlation shows values above 0.14 are statistically significant to the 99 % level. This is the level at which there is only a 1% chance that the correlations have come about by strictly random chance. The global maps of correlation coefficient with the tropical NET and OLR areas as the reference points are presented in the following group of figures. Only regions where significant correlations are found are plotted. As mentioned previously correlation values are generally low but still explain 5-10 % of the variance. Generally when correlations are found the reference area and the correlation region are much closer geographically than the ERB to ERB comparisons. Therefore, only a partial global distribution is needed to examine all significant areas. Previous studies examining tropical to mid-latitude interactions have often used only winter months when the energetic and transport processes are at a maximum. Preliminary estimates, not presented here, of winter only correlations suggest a doubling of the explained variance when only the winter months are used. Liebmann and Hartmann (1982) showed a maximum explained variance in their tropical OLR to Northern Hemisphere GH comparisons of 20 % using only the winter months.

The NET reference points are regions of anomalous radiative balance. Positive values are a heat 'source' or excess energy while negative values correspond to areas of anomalous radiative loss. Since these are top of the atmosphere measurements, the excess heating or cooling may have occurred anywhere in the earth-atmosphere column. The three NET reference areas are over the tropical ocean, therefore excess heat may go into the atmosphere or the ocean. Two of these high variability NET areas show significant correlation with the GH. These two figures follow. There was only one small area of positive correlation between Australia and New Zealand associated with the NET reference area off the west coast of South America, and therefore that figure will not be presented. Figure 6.7 shows the 500 mb GH anomaly correlation associated with the NET anomalies in the Gulf of

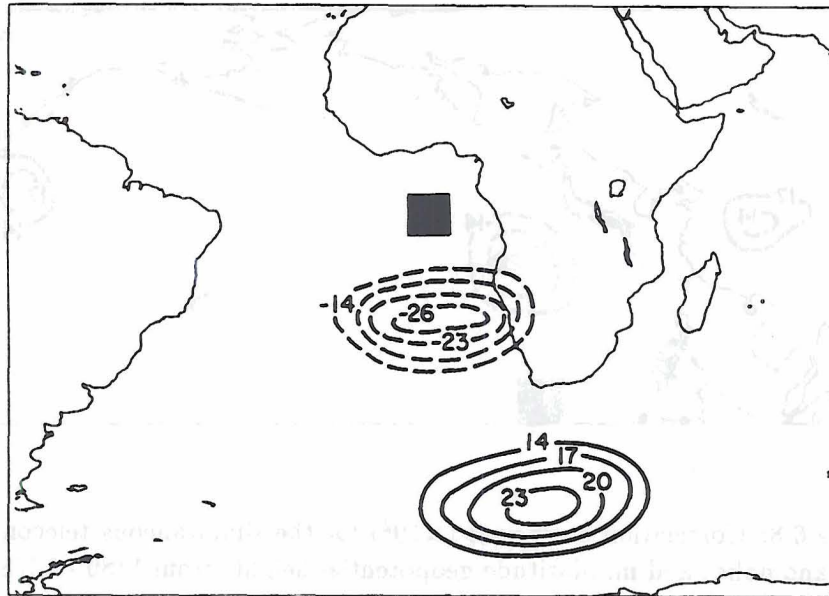


Figure 6.7: Correlation coefficient ($\times 10^2$) for the simultaneous teleconnection of tropical NET anomalies and mid-latitude geopotential heights from 1/80 - 10/87. Reference point is the black square and is centered in the Gulf of Guinea.

Guinea. An area of negative correlation is found off the west coast of South Africa with an area of positive correlation further south. Therefore, as an example, when there is a heat source represented by a positive NET anomaly there is a weakening of the subtropical high in the area at $20^\circ - 25^\circ$ S and mid-latitude ridging in the area at $40^\circ - 45^\circ$ S. The second NET anomaly region is northeast of Indonesia in the western Pacific and is presented in Figure 6.8. Positive correlations are found in China and an area adjacent to the west coast of the USA, therefore there are above normal heights in these areas related to tropical warming. Similar to the previous figure a region of negative correlation occurs directly poleward of the reference area near 30° , suggesting weakening of the subtropical high.

The next set of three figures show the OLR and GH teleconnection patterns. Generally lower OLR is representative of increasing cloudiness due to the lower emitting temperatures of the cloud tops. For example, if we have an increase in clouds, the areas with positive anomalies correspond to a decrease in 500 mb GH. Figure 6.9, with the OLR reference point centered in Brazil, shows positive correlation to areas off the east coast of the USA and the dry subtropical area of west Africa. This pattern infers that an increase in

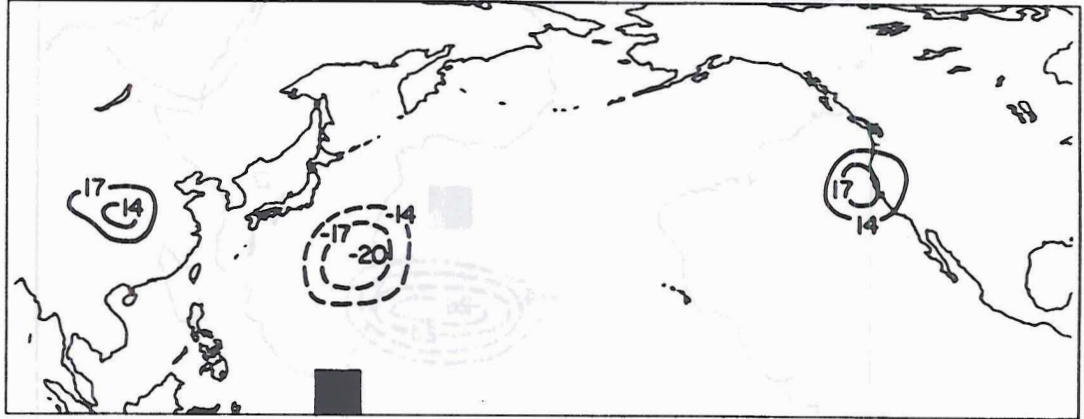


Figure 6.8: Correlation coefficient ($\times 10^2$) for the simultaneous teleconnection of tropical NET anomalies and mid-latitude geopotential heights from 1/80 - 10/87. Reference point is the black square and is centered in the western Pacific.

convective cloudiness and its associated vertical velocity over Brazil relates to a weakening of the subtropical high in west Africa and troughing off the east coast of the USA. Part of the west African area is south of 20° but was included for completeness. There was one minor area of negative correlation in the South Atlantic.

A most interesting teleconnection pattern was associated when the OLR reference area was centered in the western Pacific, Figure 6.10. Here a series of positive and negative correlation areas are found eastward from the reference point all the way to the east coast of the USA. These regions are the furthest away from any of the OLR or NET reference areas and imply a consistent pattern of alternating high and low height waves. In addition to this wave pattern a small area of positive values occurs east of Australia.

The OLR anomaly area with the strongest correlation to mid-latitude 500 mb GH was in the central Pacific, Figure 6.11. This area is known for its wide variations in OLR due to changes brought about by the ENSO and fluctuations in the ITCZ. Teleconnections to north Pacific off the west coast of the USA explained nearly 15% of the variability of the mid-latitude 500 mb geopotential height. An increase in convective clouds in the reference area is related to a decrease in the 500 mb heights in the Gulf of Alaska and ridging in the northeastern USA. There is one other region of positive CC located near the east coast of New Zealand.

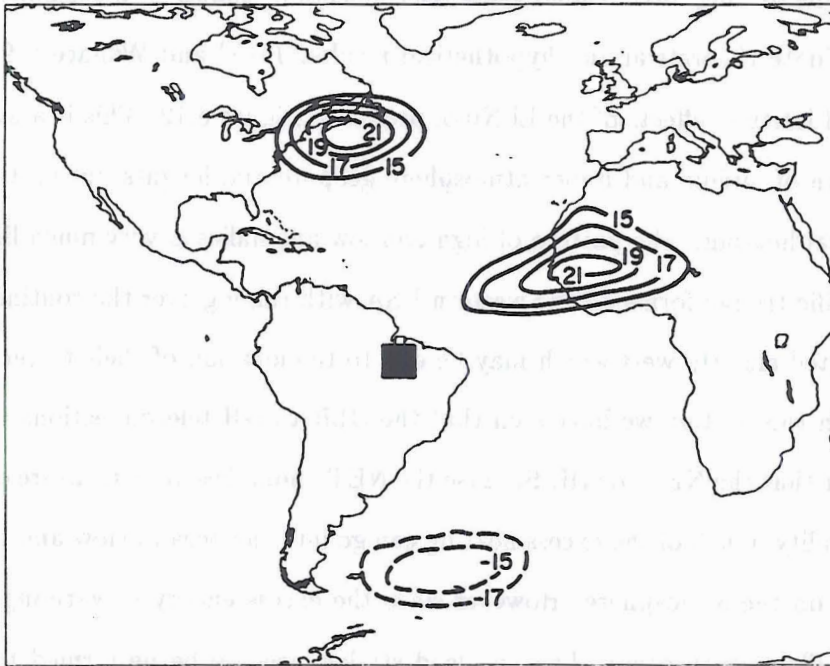


Figure 6.9: Correlation coefficient ($\times 10^2$) for the simultaneous teleconnection of tropical OLR anomalies and mid-latitude geopotential heights from 1/80 - 10/87. Reference point is the black square and is centered in Brazil.

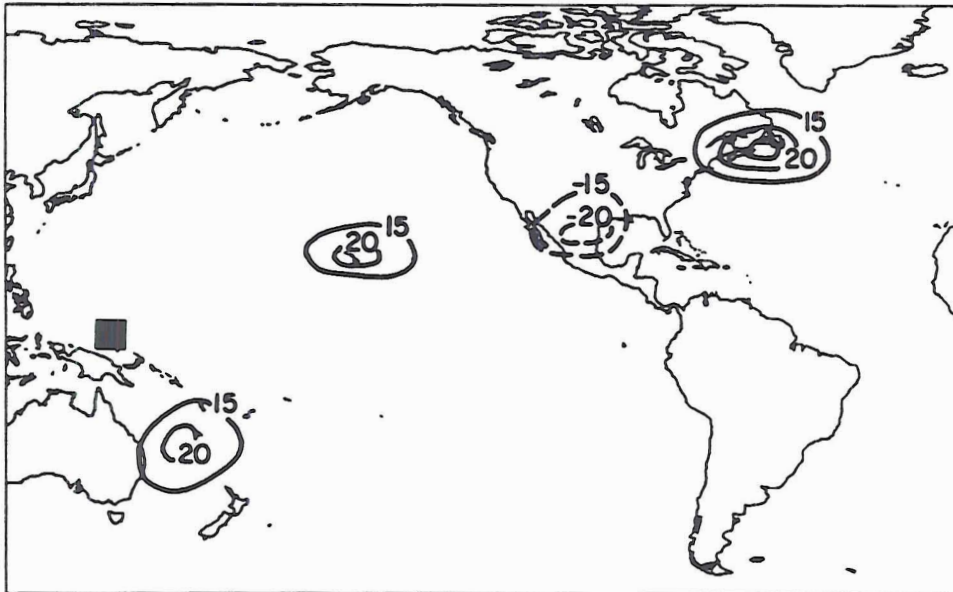


Figure 6.10: Correlation coefficient ($\times 10^2$) for the simultaneous teleconnection of tropical OLR anomalies and mid-latitude geopotential heights from 1/80 - 10/87. Reference point is the black square and is centered in the western Pacific.

One driving force behind these teleconnection studies is to use our observational data to validate theoretical and hypothetical results. Horel and Wallace (1981) in their study of mid-latitude effects of the El Niño, produced Figure 6.12. This is a hypothesized global pattern of middle and upper atmosphere geopotential heights during times of anomalous tropical heating. The pattern of high and low anomalies is very much like Fig. 6.11 where a Pacific trough forms off the western USA with ridging over the continent. Their pattern is shifted slightly west which may be due to the location of their tropical heating region.

In this section we have seen that the OLR to GH teleconnections tended to be much higher than the NET to GH. Because the NET anomalies are a measure of the total column variability, much of the excess heating can go into the ocean below and have no short term effect on the atmosphere. However since the excess energy is warming the ocean, longer term effects may occur. Lag and lead studies need to be performed to validate this. In contrast the anomalous latent energy released by an increase in convective cloudiness must go directly into the atmosphere. This allows for the variability of tropical OLR to have a much greater direct short term effect on the atmosphere and the mid-latitude height field.



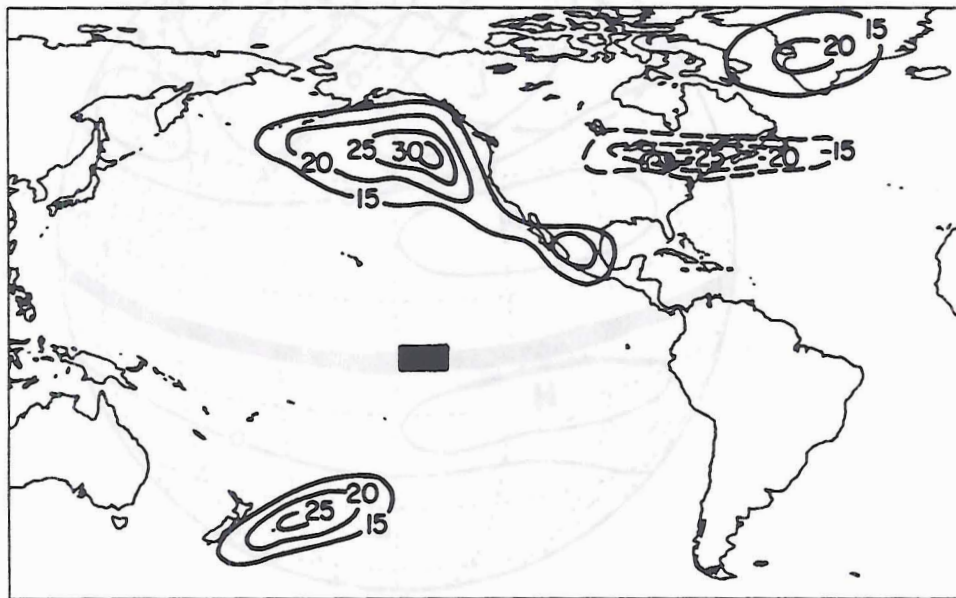


Figure 6.11: Correlation coefficient ($\times 10^2$) for the simultaneous teleconnection of tropical OLR anomalies and mid-latitude geopotential heights from 1/80 - 10/87. Reference point is the black square and is centered in central Pacific.

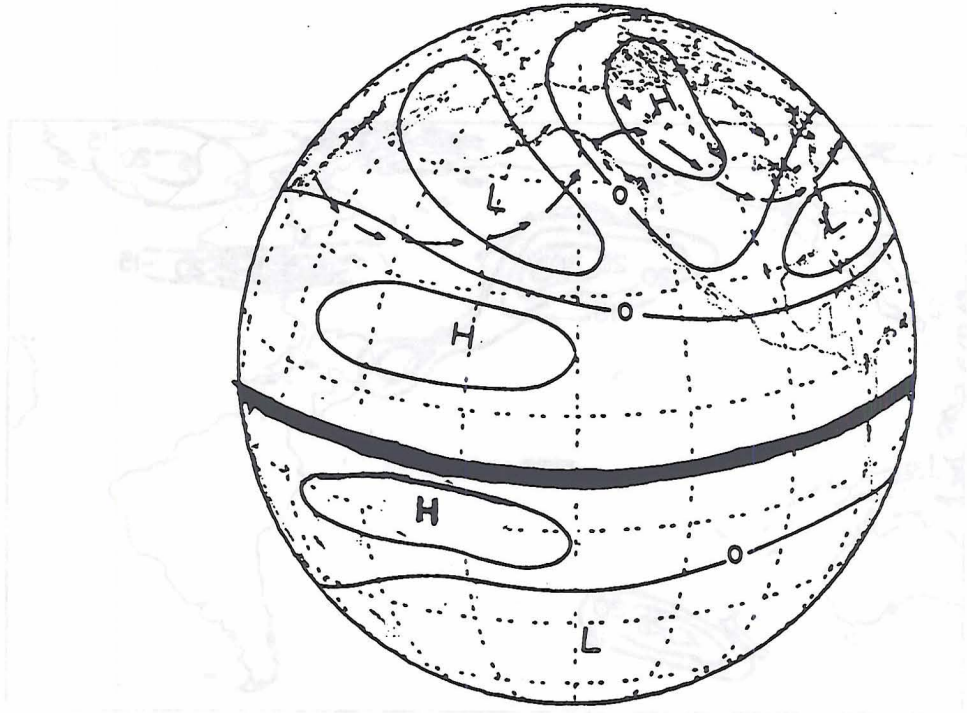


Figure 6.12: Hypothesized global pattern of mid-latitude geopotential height anomalies for the Northern Hemisphere winter during a tropical sea surface warming event (After Horel and Wallace, 1981).

Chapter 7

SUMMARY AND CONCLUSIONS

The variability of the earth radiation budget (ERB) directly modifies our atmospheric circulation. This simple statement was the driving force behind this work. We believed that with the excellent radiation and circulation data sets now available, direct connections could be found. This has been an observational study with a two pronged approach. First, the earth's radiation budget and its variability were examined. Second, the atmospheric energetics, potential and kinetic, were used to describe the state of the atmosphere and its variability, and 500mb geopotential heights for mid-latitude circulation features. Finally, these two paths converged and the ERB and circulation observations were examined for evidence of simultaneous direct relationships.

Many of the previous ERB studies which attempted to explain the interannual variability used a combination of data from different satellite and sensors. This was not necessary when using the latest set of data from the *Nimbus-7* ERB instruments. Over nine years are currently available and used throughout the previous chapters. Two to three more years are in various processing stages and will be available soon. As the decade of the 1990s begins we find renewed emphasis on the need to fully understand the earth-atmosphere-ocean system. Many new experiments are being planned to study the fundamental processes of atmospheric moisture and energy transport as well as cloud-radiation feedbacks. The Global Energy and Water Cycle Experiment (GEWEX) is occurring this decade with far reaching and ambitious goals to study almost all facets of the global system (Morel, 1990). Many of the results presented in this dissertation mirror the goals of the GEWEX experiment including: variability of the radiation budget, the effect of clouds on the net radiation, and atmospheric energetics and radiation interactions. These are

seen as fundamental problems for the improvement of radiative interactions in the rapidly developing set of global climate models.

By using the *Nimbus-7* wide Field-Of-View (WFOV) data, we created in Chapter 2, a nine year time series of weekly averages. The ERB data was extensively calibrated for consistency over the entire period from November 1978 – October 1987. A spectral deconvolution process was applied and was shown to 'enhance' the resolution. An additional set of products were available from two other sensors on *Nimbus-7*. The CMATRIX cloud product from Goddard Space Flight Center used THIR and TOMS instruments along with conventional data to form a five year estimate of global cloudiness. These products were used in later chapters to study the effects of cloud variability on the NET balance.

In Chapter 3 we first examined the *Nimbus-7* ERB climatology. Presented were the global distribution for the first eight years of the OLR, albedo, NET, total atmospheric transport, and diurnal variability. The interesting three wave pattern in the NET balance in the Southern Hemisphere was examined and found to be caused by the influences of stratiform cloudiness and continental heating. Next the annual cycle of the ERB quantities were examined. The global averaged values of the NET was found to have one annual cycle based roughly on the cycle of incident radiation. The OLR cycle, also with one cycle was driven by the continental effects of the Northern Hemisphere continental heating. The albedo cycle was found to have a secondary maximum in May and June and examination of sub-hemisphere scale averages suggests the variation in tropical cloudiness as the cause. The strength and timing of the onset of the Indian monsoon was shown to have an influence on the increase or decrease of the global averaged albedo during these months.

The interannual variability of the ERB was examined in Chapter 4. By calculating the variance of annual average and monthly averages using different time samples, areas of highest change over varying temporal scales were shown. From this the areas of greatest variability in the OLR, albedo NET balance were defined. The three areas of greatest NET change were the Gulf of Guinea, the eastern Pacific near the coast of South America, and the western Pacific near Indonesia. Using the *Nimbus-7* CMATRIX cloud climatology the changes in cloud type and amount were examined in each area. Due to the reciprocity of

the OLR and albedo the areas of greatest convective cloud changes did not greatly effect the NET. The largest changes in NET were caused by changes to areas with variable low and mid-level clouds. These have a large impact on the reflected shortwave without greatly changing the longwave flux.

Chapter 5 used circulation data from the European Centre for Medium Range Weather Forecasts (ECMWF) including multi-level winds and temperatures. The energetic parameters of zonal and eddy kinetic energy, and zonal and eddy available potential energy were calculated and averaged into weekly fields concurrent with the ERB data set. The annual cycles of hemispheric energetic averages were shown to agree well with our current understanding of the energetic conversions. Both the Southern and Northern Hemisphere's annual cycles were presented. The stronger zonal terms in the Southern Hemisphere (SH) and stronger eddy terms in the Northern Hemisphere (NH) were explained by the differences in the circulation patterns between the primarily continental NH and oceanic SH. The annual cycles of the energetics were compared to the the ERB cycles of mid-latitude radiation gradients. The annual cycles in the ERB tended to lead the energetic cycles by 2-3 weeks, which suggests the lag at which the atmosphere responds to the radiation. When the weekly anomalies were compared, the ERB and energetics anomalies most often occurred simultaneously. Significant correlations were found between each though the explained variance was generally low and between 5-30 %. The weekly averaging of the ERB data makes studies of regional ERB and energetics infeasible, therefore only the large, hemispheric scales were presented.

Chapter 6 concluded the ERB and circulation comparisons. This chapter included spatial teleconnections between simultaneous ERB anomalies, and tropical ERB and mid-latitude 500 mb geopotential height (GH) anomalies. Reference areas of highest variability OLR, albedo and NET were defined from the global distribution of interannual variability. The anomaly time series in each reference area were correlated with the anomaly time series in all other global grid areas. This produced maps of correlation coefficient associated with each reference area. Significant correlations explaining much of the variance was shown to be tied to the variability in the major El Niño event. When the tropical OLR and NET

anomalies were compared with mid-latitude 500 GH anomalies, many significant areas of connection were found though the explained variance was lower than the ERB to ERB teleconnections. The strongest of these was the atmospheric troughing off the west coast of the USA related to the equatorial OLR decrease. The tropical NET anomalies tended to have less connection with the mid-latitudes heights as much of the excess energy associated with a positive anomaly may input directly into the ocean and not have an immediate effect on the atmosphere.

We firmly believe the long term *Nimbus-7* ERB data set holds many other climate anomalies that are not observed as readily by other instrument systems. This has been shown by the Gulf of Guinea net balance anomaly. By combining the ERB data with other observations we can better understand the function of the atmosphere and how the radiation variability directly influences the circulation. Understanding the variability in the earth radiation budget and it's effect on the atmosphere must someday lead to improved long and medium range forecasts, and assist in the goal of accurate long term climate monitoring.

REFERENCES

- Ardanuy, P. E., and H. L. Kyle, 1986: El Niño and outgoing longwave radiation: Observations from Nimbus-7 ERB. *Mon. Wea. Rev.*, **114**, 415-433.
- Ardanuy, P. E., and H. Jacobowitz, 1984: A calibration adjustment technique combining ERB parameters from different remote sensing platforms into a long-term data set. *J. Geophys. Res.*, **89**, 5011-5019.
- Ardanuy, P. E. 1983: Determinability of inter-annual global and regional climate changes of the Earth radiation budget. *Fifth Conf. on Atmospheric Radiation*, Baltimore, Amer. Meteor. Soc., 410-413.
- Barkstrom, B. R., and G. L. Smith, 1984: The Earth Radiation Budget Experiment: Science and implementation. *J. Geophys. Res.*, **24**, 379-390.
- Bess, T. D., R. N. Green, and G. L. Smith, 1981: Deconvolution of wide field-of-view radiometer measurements of earth-emitted radiation, Part II: Analysis of first year of Nimbus-6 ERB Data. *J. Atmos. Sci.*, **38**, 474-488.
- Campbell, G. G., and T. H. Vonder Haar, 1980a: An analysis of two years of Nimbus-6 Earth Radiation Budget observations. *Atmos. Sci. Pap. 320*, Dept. of Atmospheric Science, Colorado State Univ., Fort Collins, Colorado.
- Campbell, G. G., and T. H. Vonder Haar, 1980b: Climatology of radiation budget measurements from satellites. *Atmos. Sci. Pap. 323*, Dept. of Atmospheric Science, Colorado State Univ., Fort Collins, Colorado.
- Cess, R. D., 1976: Climate change: An appraisal of atmospheric feedback mechanisms employing zonal climatology. *J. Atmos. Sci.*, **33**, 1831-1843.
- Carissimo, B. C., A. H. Oort, and T. H. Vonder Haar, 1985: Estimating the meridional energy transport in the atmosphere and in the oceans. *J. Phys. Oceanogr.*, **15**, 82-92.
- Charlock, T. P., K. M. Cattany-Carnes, and F. Rose, 1988: Fluctuation statistics of outgoing longwave radiation in a general circulation model and in satellite data. *Mon. Wea. Rev.*, **116**, 1540-1554.
- Charney, J. G., 1975: Dynamics of Deserts and Drought in the Sahel. *Quart. J. R. Meteorol. Soc.*, **101**, 193-202.
- Ellis, J. S., 1978: Cloudiness, the planetary radiation budget and climate. *PhD Thesis*, Dept. of Atmospheric Science, Colorado State Univ., Fort Collins, Colorado, 129 pp.

- Ellis, J. S., and T. H. Vonder Haar, 1976: Zonal average earth radiation budget measurements from satellites for climate studies. *Atmos. Sci. Pap.* 240, Dept. of Atmospheric Science, Colorado State Univ., Fort Collins, Colorado.
- Geisler, J. E., M. L. Blackmon, G. T. Bates and S. Muñoz, 1985: Sensitivity of January climate response to the magnitude and position of equatorial Pacific sea surface temperature anomalies. *J. Atmos. Sci.*, **42**, 1037-1049.
- Gruber, A., 1977: Determination of the Earth-atmosphere radiation budget from NOAA satellite data. *NASA Tech. Rpt. NESS*, **76**, pp 28.
- Gruber, A., and H. Jacobowitz, 1985: The longwave radiation estimated from NOAA polar orbiting satellites: An update and comparison with Nimbus-7 ERB results. *Adv. Space Res.*, **5**, 111-120.
- Hartmann, D. L., V. Ramanathan, A. Berroir, and G. E. Hunt, 1986: Earth Radiation Budget data and climate research. *Rev. Geophys.*, **24**, 439-468.
- Hartmann, D. L., and D. A. Short, 1980: On the use of Earth Radiation Budget statistics for studies of clouds and climate. *J. Atmos. Sci.*, **37**, 1233-1250.
- Heath, D., A. J. Krueger, and H. Park, 1978: The solar backscatter ultraviolet (SBUV) and total ozone mapping spectrometer (TOMS) experiment. *The Nimbus-7 User's Guide*, C.R. Madrid, Ed., NASA, Goddard Space Flight Center, 175-211.
- Heddinghaus, T. R. and A. F. Krueger, 1981: Annual and interannual variations in outgoing longwave radiation over the tropics. *Mon. Wea. Rev.*, **109**, 1208-1218.
- Hendon, H. H., and D. L., Hartmann, 1982: Stationary waves on a sphere: sensitivity to thermal feedback. *J. Atmos. Sci.*, **39**, 1906-1920.
- Horel, J. D., V. E. Kousky, and M. T. Kagano, 1986: Atmospheric conditions in the Atlantic sector during 1983 and 1984. *Nature* **322**, 248-251.
- Horel, J. D., J. M. Wallace, 1981: Planetary-scale atmospheric phenomena associated with the Southern Oscillation. *Mon. Wea. Rev.*, **109**, 813-829.
- Hoskins, B. J., and D. J. Karoly, 1981: The steady linear response of a spherical atmosphere to thermal and orographic forcing. *J. Atmos. Sci.*, **38**, 1179-1196.
- Hwang, P. H., Ed., 1982: Nimbus-7 temperature humidity infrared radiometer (THIR) data user's guide. NASA/Goddard Space Flight Center. 52 pp.
- Jacobowitz, H., H. V. Soule., H. L. Kyle, F. B. House, and the Nimbus-7 ERB Experiment Team, 1984a: The Earth Radiation Budget (ERB) Experiment: an overview. *J. Geophys. Res.*, **89**, 5021-5038.
- Jacobowitz, H., R. J. Tighe, and the Nimbus-7 ERB Experiment Team, 1984b: The earth radiation budget derived from the Nimbus-7 experiment. *J. Geophys. Res.*, **89**, 4997-5010.

- Jacobowitz, H., L. Stowe, J. Wydick, P. Pellegrino, E. Baldwin, V. Taylor, J. Hickey, F. House, T. Vonder Haar, A. Arking, L. Smith, A. Ingersoll, and R. Maschhoff, 1980: Radiometric performance of the Nimbus-7 Earth Radiation Budget (ERB) experiment. *Proc. Int. Radiation Symp.*, Fort Collins CO 556-558.
- Jacobowitz, H., W. L. Smith, H. B. Howell, F. W. Nagle, and J. R. Hickey, 1979: The first 18 months of planetary radiation budget measurements from the Nimbus-6 ERB experiment. *J. Atmos. Sci.*, **36**, 501-507.
- Jacobowitz, H., L. L. Stowe, and J. R. Hickey, 1978: *The Nimbus-7 Users Guide*. NASA Goddard Space Flight Center, 33-69.
- Koehler, T. L., and L. M. Whittaker, 1985: A two-week evaluation of available potential energy and kinetic energy from NMC and ECMWF analyses. *Mon. Wea. Rev.*, **113**, 865-877.
- Krueger, A. F., J. S. Winston, and D. A. Haines, 1965: Computations of atmospheric energy and its transformation for the Northern Hemisphere for a recent five-year period. *Mon. Wea. Rev.* **94**, no. 4 227-238.
- Kyle, H. L., P. E. Ardanuy, R. Hucek, and the Nimbus-7 ERB Experiment Team, 1986: El Niño and outgoing longwave radiation: An atlas of Nimbus-7 Earth radiation budget observations. *NASA Reference Publication*, **1163** pp 92.
- Kyle, H. L., P. E. Ardanuy, and E. J. Hurley, 1985: The status of Nimbus-7 earth radiation budget data set. *Bull. Am. Meteorol. Soc.*, **66**, 1378-1388.
- Kyle, H. L., F. B. House, P. E. Ardanuy, H. Jacobowitz, R. Maschhoff, and J. R. Hickey, 1984: New in flight calibration adjustment of the Nimbus-6 and -7 ERB WFOV radiometers. *J. Geophys. Res.*, **89**, 5057-5076.
- Lau, K.-M. and P. H. Chan, 1983a: Short-term climate variability and atmospheric teleconnections from satellite observed outgoing longwave radiation. Part II: Lagged correlations. *J. Atmos. Sci.*, **40**, 2751-2767.
- Lau, K.-M. and P. H. Chan, 1983b: Short-term climate variability and atmospheric teleconnections from satellite observed outgoing longwave radiation. Part I: Simultaneous relationships. *J. Atmos. Sci.*, **40**, 2735-2750.
- Liebmann, B., and D. L. Hartmann, 1984: An observational study of tropical-mid-latitude interaction on intraseasonal time scales. *J. Atmos. Sci.*, **41**, 3333-3350.
- Liebmann, B., and D. L. Hartmann, 1982: Interannual variation of outgoing IR associated with tropical circulation changes. *J. Atmos. Sci.*, **39**, 1153-1162.
- Lönnerberg, P. and D. Shaw, 1985: Data selection and quality control in the ECMWF analysis system. *ECMWF Wrkshp on Quality Cntrl of Met. Obs.*, 6-9 Nov 1984.
- Lorenc, A. C., 1981: A global three-dimensional multivariate statistical interpolation scheme. *Mon. Wea. Rev.* **109**, 701-721.

- Lorenz, E. N., 1955: Available potential energy and the maintenance of the general circulation. *Tellus*, **7**, 157-167.
- Maschhoff, R., A. Jalink, L. Hickey, and J. Swedberg, 1984a: Nimbus earth radiation budget sensor characterization for improved data reduction fidelity. *J. Geophys. Res.*, **89**, 5057-5076.
- Maschhoff, R., G. G. Campbell, and T. H. Vonder Haar, 1984b: In-orbit characterization of spaceborne radiometers: understanding thermal sensor performance in a dynamic environment. *IRS '84: Current Problems in Atmospheric Radiation* Proceedings of the International Radiation Symposium, Perugia, Italy. 343-346.
- Min, K. D. and L. H. Horn, 1982: Available potential energy in the Northern Hemisphere during the FGGE year. *Tellus*, **34**, 526-539.
- Morel, P. 1990: Scientific plan for the Global Energy and Water Cycle Experiment (GEWEX). Draft for the WMO World Climate Research programme publication series.
- Ohring, G., A. Gruber, and R. Ellingson, 1984: Satellite determination of the relationship between total longwave radiation flux and infrared window radiance. *J. Clim. Appl. Meteor.*, **22**, 416-425.
- Ohring, G., and P. Clapp, 1980: The effect of changes in cloud amount on the net radiation at the top of the atmosphere. *J. Atmos. Sci.*, **37**, 447-454.
- Oort, A. H., and T. H. Vonder Haar, 1976: On the observed annual cycle in the ocean-atmosphere heat balance over the Northern Hemisphere. *J. Phys. Ocean.*, **6**, 781-800.
- Oort A. H., and J. P. Peixoto, 1974: The annual cycle of the energetics of the atmosphere on a planetary scale. *J. Geophys. Res.*, **79**, 2705-2719.
- Oort A. H. 1964: On Estimates of the Atmospheric Energy Cycle: *Mon. Wea. Rev.* **92**, no 11 483-493.
- Philander, S. G. H., 1986: Unusual Conditions in the Tropical Atlantic Ocean in 1984. *Nature* **322**, 236-238.
- Ramanathan, V., B. B. Barkstrom, and E. F. Harrison 1989: Climate and the Earth's radiation budget. *Physics Today*, **42**, 22-32.
- Ramanathan, V. 1987: The role of Earth Radiation Budget studies in climate and general circulation research. *J. Geophys. Res.*, **92**, 4075-4098.
- Randel, D. L., and T. H., Vonder Haar, 1990: On the interannual variation of the Earth Radiation Balance. *J. Climate*, **3**, 1168-1173.
- Randel, D. L., T. H. Vonder Haar, and G. G. Campbell, 1985: Hemispheric differences in the Earth radiation budget derived from Nimbus-7 related to climate studies. *Advances in Space Research*, **5**, 99-103.

- Trenberth, K. E., and J. G. Olson, 1988: ECMWF Global Analyses 1979-1986. Circulation Statistics and Data Evaluation. *NCAR Tech. Note*. NCAR/TN-300+STR 94 pp plus 12 fiche.
- Vonder Haar, T. H., and A. H. Oort, 1973: New estimates of annual poleward energy transport by Northern Hemisphere Oceans. *J. Phys. Oceanogr.*, **2**, 169-172.
- Vonder Haar, T. H., and V. E. Suomi, 1971: Measurements of the earth's radiation budget from satellites during a five-year period. I. Extended time and space means. *J. Atmos. Sci.*, **28**, 305-314.
- Vonder Haar, T. H., 1968: Variation of the earth's radiation budget. Ph.D. dissertation, Dept. of MET, Univ. of Wisconsin, 188pp.
- Webster, P. J., 1982: Seasonality in the local remote atmospheric response to sea surface temperature anomalies. *J. Atmos. Sci.*, **39**, 41-52.
- Weisberg R. H., and C. Colin, 1986: Equatorial Atlantic Ocean Temperature and Current Variations During 1983 and 1984. *Nature* **322**, 240-243.

- Randel, D.L., L.D. Smith, T.H. Vonder Haar, and G.G. Campbell, 1984: Analysis of Nimbus Earth radiation budget measurements for climate study. *IRS '84: Current Problems in Atmospheric Radiation* Proceedings of the International Radiation Symposium, Perugia, Italy. 206-209.
- Randel, D.L., 1983: Space-time variations in the earth radiation budget. Colorado State University, Department of Atmospheric Science paper 374. 96 pp.
- Raschke, E., T.H. Vonder Haar, W.R. Bandeen, and M. Pasternak, 1973: The annual balance of the earth-atmosphere system during 1969-1970 from Nimbus-3 measurements. *NASA Tech. Note 7249*.
- Raschke, E., and W.R. Bandeen, 1970: The radiation balance of the planet earth from radiation measurements of the satellite Nimbus-II. *J. Appl. Meteor.*, **9**, 215-238.
- Saunders, R.W., L.L. Stowe, G.G. Hunt, and C.F. England, 1983: An intercomparison between radiation budget estimates from METEOSAT 1, Nimbus-7 and TIROS-N satellites. *J. Appl. Meteor.*, **22**, 446-459.
- Short, D.A., and R.F. Cahalan, 1983: Interannual variability and climatic noise in satellite-observed outgoing longwave radiation. *Mon. Wea. Rev.*, **111**, 572-577.
- Smith, G.L., and T.D. Bess, 1983: Annual cycle and spatial spectra of Earth emitted radiation at large scales. *J. Atmos. Sci.*, **40**, 998-1015.
- Smith, G.L., and R.N. Green, 1981: Deconvolution of wide field-of-view radiometer measurements of earth-emitted radiation, Part I: Theory. *J. Atmos. Sci.*, **38**, 998-1015.
- Smith, L.D., and T.H. Vonder Haar, 1989: Clouds - radiation - hydrologic cycle interactions in a GCM: Impact upon the planetary radiation balance. *J. Geophys. Res.*, *In Press*
- Smith, L.D., T.H. Vonder Haar, and D.L. Randel, 1986: Interannual variability study of the earth radiation budget from Nimbus-7 monthly data. Sixth Conference on Atmospheric Radiation, Williamsburg, Va. *Extended Abstracts*, 211-214.
- Soule, H.V., 1983: Nimbus-6 and -7 Earth Radiation Budget (ERB) sensor details and component tests. *NASA Tech. Memo.*, **83906**.
- Staylor, W.F., 1990: Degradation rates of the AVHRR visible channel for the NOAA 6, 7, and 9 spacecraft. *J. Atmos and Ocean. Tech.*, **7**, 411-423.
- Stephens, G.L., G.G. Campbell, and T.H. Vonder Haar, 1981: Earth radiation budgets. *J. Geophys. Res.*, **86**, 9739-9760.
- Stowe, L.L., C.G. Wellemeyer, T.F. Eck, H.Y..M. Yeh, and the Nimbus-7 Cloud data processing Team, 1988: Nimbus-7 global cloud climatology. Part I: Algorithms and validation. *J. Clim.* **1**, 445-470.
- Stowe, L.L., H.Y..M. Yeh, T.F. Eck, C.G. Wellemeyer, H. Lee Kyle, and the Nimbus-7 Cloud data processing Team, 1988: Nimbus-7 global cloud climatology. Part II: First Year Results. *J. Clim.* **2**, 671-709.